Technical Progress Report

LOW TEMPERATURE CATHODE SUPPORTED ELECTROLYTES

DOE Contract No.: DE-AC26-99FT40710

Report for the period of

October 1, 2001 to March 31, 2002

Submitted by

Dr. Harlan U. Anderson
Dr. Fatih Dogan
Dr. Vladimir Petrovsky
University of Missouri-Rolla
Electronic Materials Applied Research Center (EMARC)
303 Materials Research Center
Rolla, MO 65401

Executive Summary
October 2001 – March 2002

This project has three main goals: Thin Films Studies, Preparation of Graded Porous Substrates and Basic Electrical Characterization and testing of Planar Single Cells.

This period has continued to address the problem of making dense ½ to 5μm thick dense layers on porous substrates (the cathode LSM).

Our current status is that we are making structures of 2-5cm^2 in area, which consist of either dense YSZ or CGO infiltrated into a 2-5μm thick 50% porous layer made of either nanoncrystalline CGO or YSZ powder. This composite structure coats a macroporous cathode or anode; which serves as the structural element of the bi-layer structure. These structures are being tested as SOFC elements.

A number of structures have been evaluated both as symmetrical and as button cell configuration.

Results of this testing indicates that the cathodes contribute the most to cell losses for temperatures below 750°C.

In this investigation different cathode materials were studied using impedance spectroscopy of symmetric cells and IV characteristics of anode supported fuel cells. Cathode materials studied included $La_{0.8}Sr_{0.2}Co_{0.2}Fe_{0.8}O_3$ (LSCF), $La_{0.7}Sr_{0.2}MnO_3$ (LSM), $Pr_{0.8}Sr_{0.2}Fe_{0.8}O_3$ (PSCF), $Sm_{0.8}Sr_{0.2}Co_{0.2}Fe_{0.8}O_3$ (SSCF), and $Yb_{.8}Sr_{0.2}Co_{0.2}Fe_{0.8}O_3$ (SSCF). A new technique for filtering the Fourier transform of impedance data was used to increase the sensitivity of impedance analysis.

By creating a filter specifically for impedance spectroscopy the resolution was increased. The filter was tailored to look for specific circuit elements like R//C, Warburg, or constant phase elements. As many as four peaks can be resolved using the filtering technique on symmetric cells. It may be possible to relate the different peaks to material parameters, like the oxygen exchange coefficient. The cathode grouped in order from lowest to highest ASR is LSCF < PSCF < SSCF < YSCF < LSM. The button cell results agree with this ordering indicating that this is an important tool for use in developing our understanding of electrode behavior in fuel cells.

LOW TEMPERATURE CATHODE SUPPORTED ELECTROLYTES

Report for Period October 1, 2001 to March 31, 2002

TABLE OF CONTENTS

1.0: Abstract

This project has three main goals or tasks:

Task 2.1: Thin Film Studies: Nanocrystalline Electrolyte

- Completed

Task 2.2: Preparation of Graded Porous Substrates

- 85% complete
- nearly on schedule

Task 2.3: Basic Electrical Characterization And Testing of Planar Single Cells

- 65% complete
- behind schedule, but most of the measurement obstacles have been overcome.

2.0: Future Research

Research Planned for FY 2001-2002:

Continue Optimization of the Cathode Substrate. Evaluate:

a) The influence of porous CeO_2 layer on SOFC performance.
b) The influence of the addition of LSCF into CeO_2 layer on SOFC performance.
c) The influence of the conductivity of the CeO_2 layer on SOFC performance.

Make Single Cell Fuel Cell Measurements

a) Cell performance as a function of electrolyte thickness and temperature.
    - YSZ electrolyte
    - CeO_2 electrolyte
b) Cell performance as a function of electrode composition.
    - Anode
    - Cathode

Continue Studies Related to Placing Thin Electrolyte Films onto Porous Substrates

a) Polymer precursor onto a graded substrate.
b) Transfer of dense films to a porous substrate.
c) Nanocrystalline/polymer precursor composites.

3.0: Individual Task Reports

Rational of Our Program Directions
Potential Impact on DOE's SECA Initiative

Fuel cell design by itself is a complicated problem. Many particular directions need to be analyzed and solved to get the final result, but there is no doubt that the combination of the materials involved in this design is a key issue. During the past few years there has been an effort promoted by the US Department of Energy (SECA Program) to lower the operating temperature of solid oxide fuel cells. As a result, the solid oxide fuel cell activities at the Electronic Materials Applied Research Center (EMARC) of the University of Missouri-Rolla (UMR) have been focused on the fabrication of thin (0.5 to 5μm thick), dense electrolyte layers of either zirconia or ceria. The route that has been taken is to deposit a polymer precursor solution, which contain the cations of the chosen electrolyte onto a substrate and subsequently convert the resulting polymeric films into dense layers by thermal treatment.

The efficiency of oxygen ion permeation through the SOFC structure is obviously a main issue [1]. Different components influence this ion permeation [2]. First of all, for the electrolyte there are the ohmic losses connected with the electrolyte itself. There are a limited number of the materials, which can be effectively used as an electrolyte. Yttrium or scandium substituted zirconia and gadolinium or samarium substituted ceria are the prime candidates to date [1-6]. Zirconia currently is the electrolyte of choice because it remains an ionic conductor at temperatures as high as 1000^{o}C under the reducing conditions present in the fuel. Ceria has a problem of becoming a mixed electronic/ionic conductor under the reducing conditions existing in the fuel. However, in the 500 to 700^{o}C regime, ceria may be sufficiently stable to become useful as an electrolyte, so certainly needs to be included in our considerations. Therefore, the discussion which mainly follows focuses on zirconia does include ceria, but in lesser detail. These are very good ionic conductors, but at this time improvements in the conductivity are unlikely. Thus, decreasing the electrolyte thickness appears to be the best way to improve the electrolyte performance in the lower temperature regime, but this solution does pose processing problems since it requires electrolyte thickness of <10 micrometers. This is illustrated in figure 1 which shows the relation between thickness, temperature and resistance/unit area. This suggests that if we are to operate a cell at 500^{o}C using a YSZ electrolyte, then the thickness of < 1 micrometer is required (or < 5 micrometers for Sm or Gd doped ceria). This means that we indeed need to focus on processing electrolytes in the 1 to 5 micrometer range.

The processing of dense electrolyte layers in the required 1-5 micrometer range is not simple because layers of such thickness cannot support themselves and requires a supporting structure for mechanical integrity. Thus the dense electrolyte must be produced as an integral layer of either the anode or cathode, which provide the mechanical support for the electrolyte/electrode structure. The usual methods to achieve this structure are:

1) Cast thin tape of the electrolyte and laminate it to tape of the electrode, followed by co-sintering to obtain the dense electrolyte/porous electrode structure. Most of these electrolytes are > 5 micrometer in thickness, however G. E. has been very successful in producing electrolyte in the < 5 micrometer range by adding a calendering step in the process prior to sintering [7].

A number of SOFC programs throughout the world are using this type of processing to make their electrolyte/electrode structures. The necessity of co-sintering the structure combined with the need for sintering temperatures > 1200^{o}C carries with it problems with dimensional stability and the possibility of chemical reactions between the electrolyte and electrode. These are problems which all of the researchers and/or producers of SOFC cells face and which our research is designed to avoid.

2) The electrolyte is deposited onto the porous electrode by a deposition technique such are: chemical vapor deposition, plasma deposition, flame deposition, evaporation, sputtering and so on. All of these techniques have shown success in depositing a dense electrolyte on a pre-sintered porous electrode with the Siemens-Westinghouse electro-vapor-deposition (EVD) process being the most successful [7]. With the exception of the EVD process, none of these processes require processing temperatures for the entire electrolyte/electrode structure of >1250^{o}C so interfacial reactions are less of a problem than with co-sintering, but cost and the ability to reproducibly produce dense electrolyte layers are problems.

3) Deposition of colloidal electrolyte powders onto partially sintered electrodes by such techniques as electrophoretic deposition, vacuum slip casting, dip coating, spin coating, spray pyrolysis and so on are processes being used by a number of SOFC programs [7]. In order to achieve non-porous density of the electrolyte, co-sintering temperatures of > 1100^{o}C are required which presents problems with dimensional stability, warping, cracking and interfacial reactions (the same problems as with co-sintering of tape).

Another consideration of processes which require heating the electrolyte to temperatures in the 1200 to 1400^{o}C range for the development of a dense structure is that the resulting grain size in an electrolyte of YSZ will be in the 0.5 to > 1 micrometer range. This is not a problem when the electrolyte thickness is > 10 micrometers, but when the thickness is reduced to essentially the diameter of the grains in the electrolyte, a problem with reliability and porosity does occur. In general, for reliability considerations, the grain size in the electrolyte layer should be no more than 10 to 25% of the layer thickness. That is well known problem in the ceramic capacitor production and we shown that the same effect takes place for thin YSZ films [8]. This means that the grain size needs to be decreased into the submicron range to have the electrolyte thickness in the range of 1 to 5 micron.

The question is:
Can we use ceramic preparation techniques to achieve dense electrolytes with submicron grain size simply by decreasing the size of the initial powder and lowering the sintering temperature?

And the answer is no, because it is difficult to process at sufficiently low temperatures to avoid grain growth into the micron range.

We will illustrate the problem with an example of YSZ tape prepared from the powder with the initial grain size of 200nm. Figure 2 shows the electrical conductivity over the temperature after sintering in the range 1000-1400^{o}C. It can be seen, that at least 1200-1300^{o}C is needed to approach maximum conductivity, and to achieve closed porosity density. The final grain size of the dense specimens exceeds 1μm at these sintering temperatures, thus we cannot expect to fabricate < 10μm thick electrolyte. As can be seen from figure 1, in order to have sufficiently low resistance per sq.cm (ASR) at 700^{o}C, an electrolyte needs to be <=10μm in thickness. This is the maximum temperature, which SECA Initiative requires. Thus this structure will not solve our problem.

The second example is ceria colloidal suspension with very small initial grain size (~5nm).

Will it solve the problem?

The answer is no again.

The films prepared from colloidal suspensions have about 50-60% initial porosity. A sintering temperature of 800^{o}C is sufficient to introduce acceptable conductivity (fig.3), but much higher sintering temperature (such as 1200-1300^{o}C) is needed to densify the material (fig.4). The grains grow during the sintering process (fig.5), and we will have a minimum thickness limit of about 10μm for the electrolyte, which presents performance problems in the 500^{o}C range.

The research that we have been doing over the last 7-8 years with support from both the Gas Research Institute and DOE has allowed us to develop the methods by which dense electrolyte layers of <5 microns in thickness can be attached to either the porous anode or porous cathode to yield an electrolyte/electrode structure which has the potential of being >100cm^{2} in area. In addition, due to the nature of the process, it has the potential of being a very cost effective method of building the electrolyte/electrode structures, which can operate in the 500 to 700^{o}C range.

The process we are using involves the use of the patented (US Patent # 5,494,700) polymeric precursor technique, which was developed with GRI funding for the electrolyte layer deposition. Our experiments show that ceria films prepared from polymeric precursors have relatively high initial density (more than 85%) at temperatures as low as 400^{o}C and the density increases quickly with increasing temmperature (we have practically dense film after annealing at 800^{o}C) (fig.6). Grain size in these dense films is less than 100nm and we now can work with electrolyte thicknesses of <5μm.

The same situation takes place with YSZ polymeric films: initial density is high (fig.7-9), and it is possible to have dense film with good electrical properties at 800^{o}C (fig.10). Grain size will be again in the submicron region (less than 100nm) and we will have no limitations on the electrolyte thickness. In addition, as shown in figure 11, the polymer precursor method allows the densification temperature to be lowered by about 500^{o}C compared to nanocrystalline powder.

The conclusion is:

<u>Nanocrystalline</u> films and <u>polymeric precursors</u> are an appropriate way to go if we want to decrease the ohmic resistance of the electrolyte by decreasing its thickness.

We have shown in our previous investigations that nanocrystalline layers prepared from polymeric precursors are strong contenders for electrolyte preparation in SOFC design. It gives the possibility of preparation temperature about 800^{o}C while maintaining the grain size in the submicron level (see fig.4-6 for SDC and fig.7, 8, 9, 11 for YSZ). At the same time the density and the conductivity of the films are high. The problem with the polymeric precursors is the low cracking limit for one deposition, so we need to go with multiple depositions to build micron thick layers [8-17]. In addition the polymer precursor process has difficulty in covering a surface which has pores with diameter >0.2micron in diameter. This presents a real limitation when we are trying to produce non-porous layers onto sintered porous electrodes. This has been a real "show stopper" for us for sometime and has not been easy to solve. However, our studies on the current DOE contract have allowed us to arrive at a very good solution. The solution has two parts:

1) the development of a graded cathode structure which has pore diameters <1 micron on the surface and
2) the combination of polymeric precursors and nanocrystalline powder, which is shown in figures 12-16. A five-micron thick nanocrystalline YSZ layer shown in fig.12 was prepared from nanocrystalline YSZ powder and YSZ polymeric precursor at a temperature as low as 400^{o}C using only one deposition. This layer has ~50% porosity, but has strong bonding between the grains and substrate. The result of the impregnation of this layer by polymeric precursor is shown in figure 13. It can be seen, that we have a dense nanocrystalline layer about 5μm thick after this impregnation.

This combination of nanocrystalline powder and polymeric precursor extends the scope of the polymeric precursor application, and can open a new path to build cost effective fuel cells with high performance which can be operated at temperatures in the 500-700^{o}C range.
This is the direction we are concentrating for the rest of this program since it looks very practical and we have shown that non-porous composite electrolytes can be fabricated at temperatures below 900^{o}C for either YSZ or CGO electrolytes.

We do not expect these electrolyte/electrode structures to give particularly good performance at 500^{o}C because the surface exchange reactions at the electrodes limit the efficiency at such a low temperature. Thus, this problem has to be address if we are to be successful at developing the electrolyte/electrode composite for operation in the 500 to 700^{o}C range. Thus, we are incorporating this into our research plan.

Direct measurements of the surface exchange coefficient show that the area specific conductance for ionic conductors is extremely low (fig.17). We need to withdraw electrons from the surface to ensure high rates of the oxygen ion exchange. Metal electrodes could perform this function, but the well-known triple-boundary problem limits the efficiency of these electrodes.

Mixed conductors as an electrode material could solve the problem. These materials have much higher exchange coefficients and there is no problem to withdraw electrons because of high electronic conductivity of mixed conductors. But these exchange coefficients are still not high enough to ensure current density of more than 1A/cm^2 (especially at low operating temperature) (fig.17). Direct permeation measurements confirm this fact: oxygen ion current is too low (fig.18).

The only way to resolve this problem is to increase the effective surface area at the electrolyte-electrode interface by building a thin reaction layer with submicron grain size and high porosity. Our colleagues at the University of Utah showed the efficiency of this approach [2]. They showed that introduction of a thin (~10μm) interlayer with the grain size of 1μm drastically improves fuel cell performance, but they had problems at low operating temperatures. Further decrease of the grain size in the reaction interlayer could solve these problems by further increasing the effective surface area. Simply sintering metal oxide powder cannot do it, because sintering temperatures (such as 1200-1300^{o}C) are too high and the grains will grow. The combination of the polymeric precursors with nanocrystalline powder offers a solution. As we showed, it is possible to decrease the sintering temperature to 800^{o}C and introduce high conductivity in the layer while maintaining the grain size in the submicron level (see fig.4-6 for SDC and fig.7, 8, 9, 11 for YSZ).

The other reason to use polymeric precursors in the reaction interlayer is the relatively low ionic conductivity of the mixed conductors shown by direct diffusion measurements (fig.19). So we need to minimize the thickness of the mixed conductor in the reaction interlayer, i.e. to use low sintering temperature.

An additional benefit of making this electrolyte/electrode composite structure is that it allows us to selectively place catalytic active oxides in the porous interfacial region near the triple phase boundary regions thereby aiding in the minimization of the influence of the interfacial reactions.

Our current status is that we are making structures of 2-5cm^2 in area, which consist of either dense YSZ or CGO infiltrated into a 2-5μm thick 50% porous layer made of either nanocrystalline CGO or YSZ powder. This composite structure coats a macroporous cathode or anode, which serves as the structural element of the bi- layer structure. Examples of these structures are illustrated in figures 12-17. These structures will be tested to determine their performance as SOFC elements.

References

1. B.C.H. Steele, Material science and engineering: The enabling technology for the commercialization of fuel cell systems, Journal of Materials Science, 36, 1053-1068 (2001).

2. Yi Jiang and Anil V. Virkar, A high performance, anode-supported solid oxide fuel cell operating on direct alcohol, Journal of the Electrochemical Society, 148 (7), A706-A709 (2001).

3. Seungdoo Park, Raymond J. Gorte, and John M. Vohs, Tape cast solid oxide fuel cells for the direct oxidation of hydrocarbons, Journal of the Electrochemical Society, 148 (5), A443-A447 (2001).

4. Conghua Wang, Wayne L. Worrell, Seungdoo Park, John M. Vohs, and Raay J. Gorte, Fabrication and performance of thin-film YSZ solid oxide fuel cells, Journal of the Electrochemical Society, 148 (8), A864-A868 (2001).

5. C. Milliken, S. Guruswamy, and A. Khandkar, Evaluation of ceria electrolytes in solid oxide fuel cells electric power generation, Journal of the Electrochemical Society, 146 (3), 872-882 (1999).

6. Rajiv Doshi, Von L. Richards, J.D. Carter, Xiaoping Wang, and Michael Krumpelt, Development of solid-oxide fuel cells that operate at 500^{o}C, Journal of the Electrochemical Society, 146 (4), 1273-1278 (1999).

7. N.Q.Minh, Recent Development in Material Science and Technology for Solid Oxide Fuell Cells", pp. 54-60 in High Temperature Materials, ed. S.C.Singhal. Proceedings volume 2002-5 The Electrochemical Society, Pennington, Inc., NJ, USA.

8. B.P.Gorman, and H.U.Anderson, "Synthesis and microstructural characterization of unsupported nanocrystalline zirconia thin films", J. Amer. Ceram. Soc., 84 (14), 890-892 (2001).

9. V. Petrovsky, B.P. Gorman, H.U. Anderson, and T. Petrovsky, Optical properties of CeO_2 films prepared from colloidal suspension, Journal of Applied Physics, 90 (5), 2517-2521 (2001).

10. Toshio Suzuki, Igor Kosacki, Vladimir Petrovsky, and Harlan U. Anderson, Optical properties of undoped and Gd-doped CeO_2 nanocrystalline thin films, Journal of Applied Physics, 91 (4), 2308-2314 (2002).

11. V.Petrovsky, H.Anderson, and T.Petrovsky, "Nanoporous alumina films prepared from alumina colloidal solution", Mat.Res.Soc.Proc., 581, pp 553-558 (2000).

12. V.Petrovsky, H.Anderson, and T.Petrovsky, "Planarization of rough substrates by alumina colloidal suspension", Proc. 102 Annual American Ceramic Society Meeting, St.Louis, (2000) – in press.

13. I.Kosacki, V.Petrovsky, and H.Anderson, "Electrical conductivity in nanocrystalline ZrO_2:Y, Mat.Res.Soc.Proc., 548, pp 505-510 (1999).

14. I.Kosacki, V.Petrovsky, and H.Anderson, "Modeling and characterization of electrical transport in oxigen conducting solid electrolites", J. of Electroceramics, 4, 1, pp 243-249 (2000).

15. I.Kosacki, T.Suzuki, V.Petrovsky, and H.Anderson, "Electrical conductivity of nanocrystalline ceria and zirconia films", Solid State Ionics, (2000) – in press.

16. V.Petrovsky, B.Gorman, H.Anderson, and T.Petrovsky, “Nanoporous ceria films prepared from colloidal suspension”, to be published in Mat.Res.Soc. (2001).

17. B.P.Gorman, V.Petrovsky and H.U.Anderson, “Microstructure – electrical properties relationship in porous, nanocrystalline CeO2 thin films”, submitted to ACerS Spring Meeting (2001).

Conductivity of YSZ and SDC and corresponding electrolyte thickness limitation

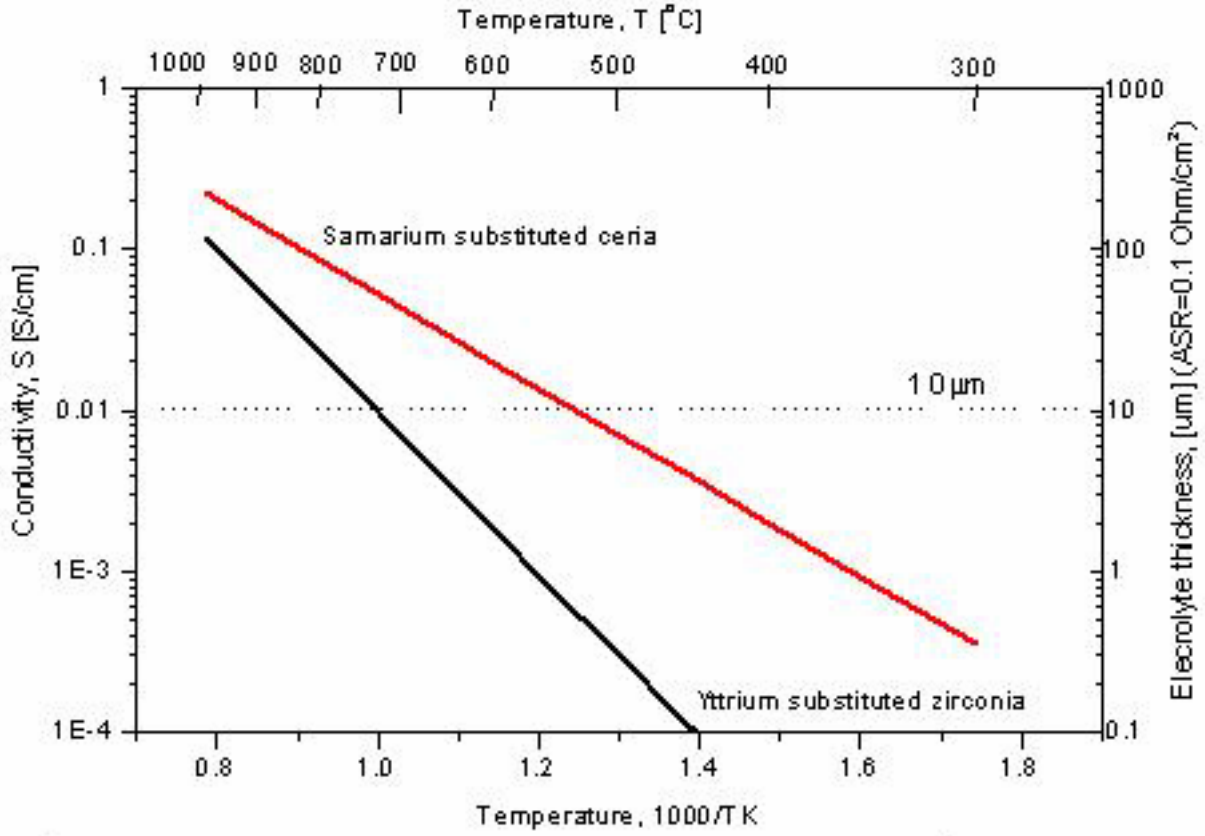

YSZ: σ=0.12 S/cm at 1000°C, E=1eV

T.H.Etsell and S.N.Flengas, Chem.Rev., 70, 339 (1970)

SDC: σ=0.085 S/cm at 800°C, E=0.58eV

H.Yahiro, E.Eguchi and H.Arai, Sol.St.Ionics, 36, 71 (1989)

Fig.1.

YSZ nanocrystalline tape sintered at different temperatures

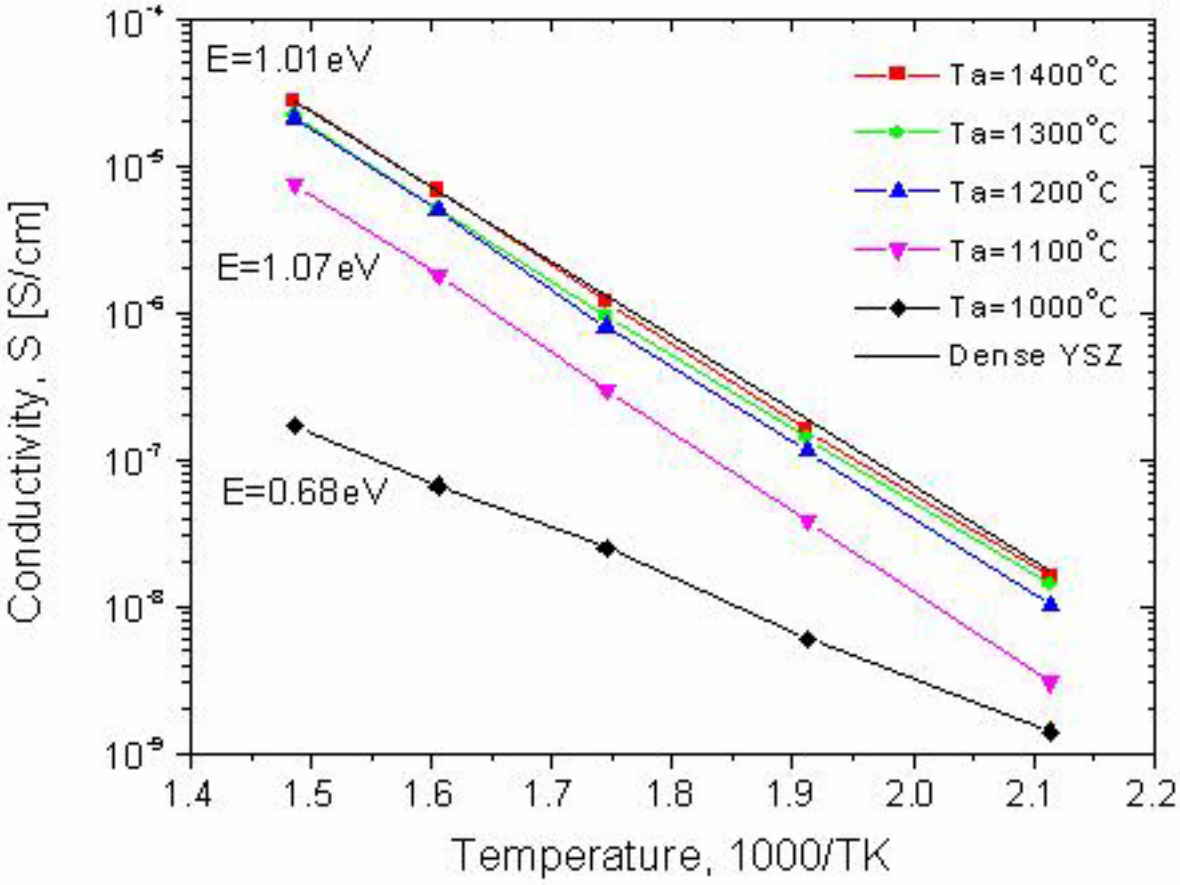

Fig. 2.

Colloidal ceria suspension as a precursor on sapphire (initial grain size in the powder ~5nm)

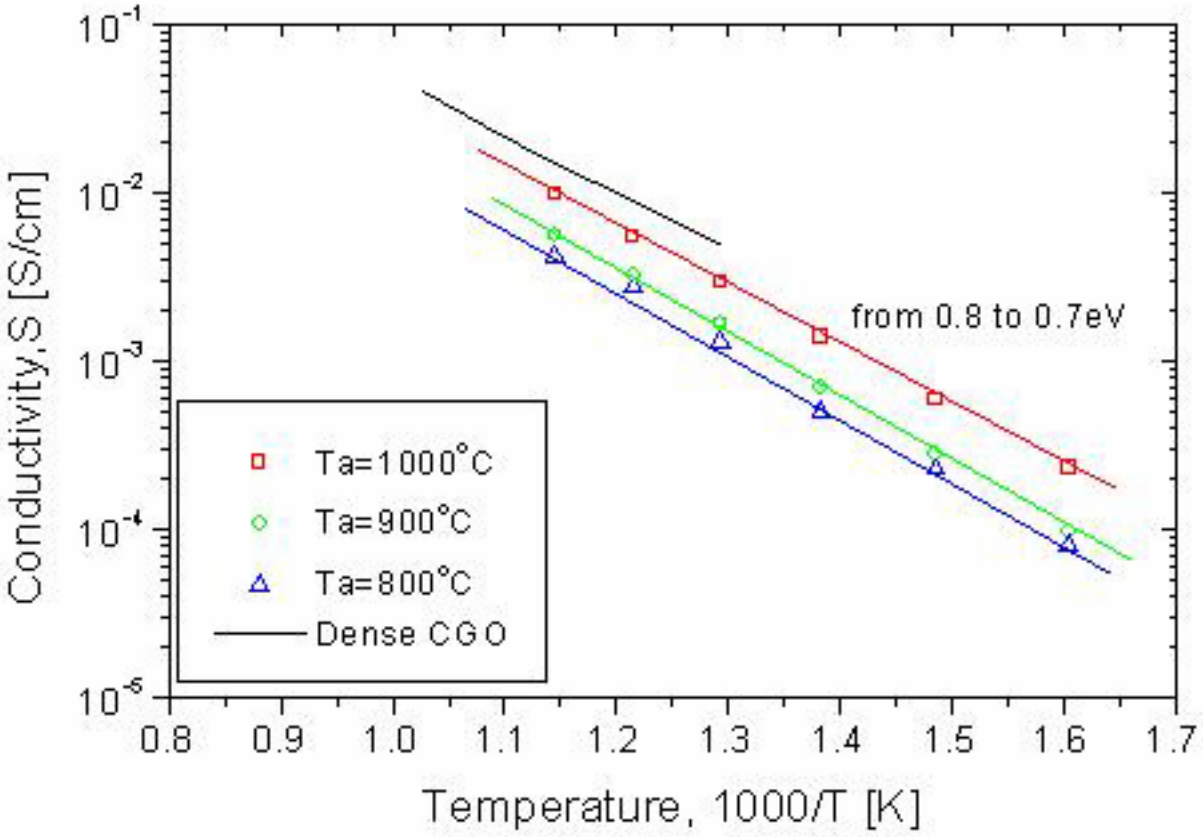

Fig.3.

Ceria films on sapphire prepared from colloidal suspension. Densification and grain growth during sintering

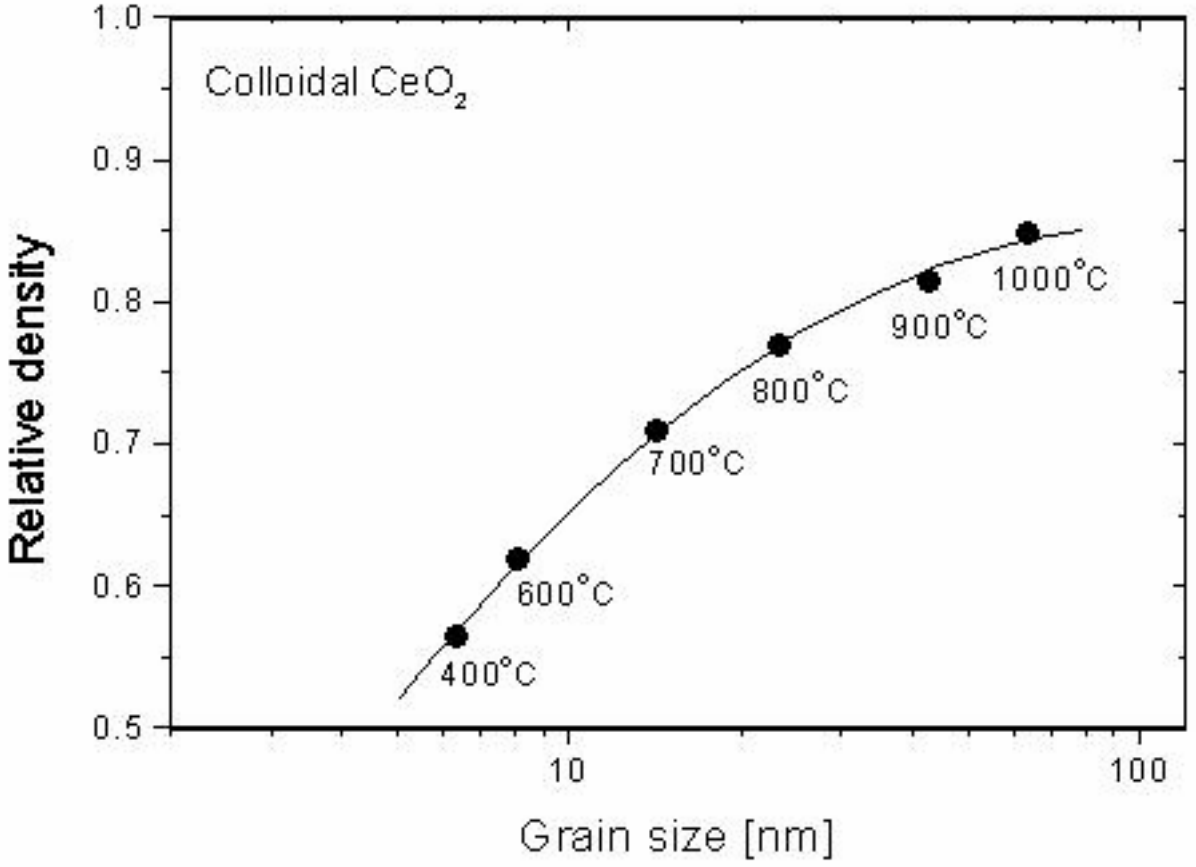

Fig.4.

Shrinkage and grain growth
in nanocrystalline ceria films on sapphire

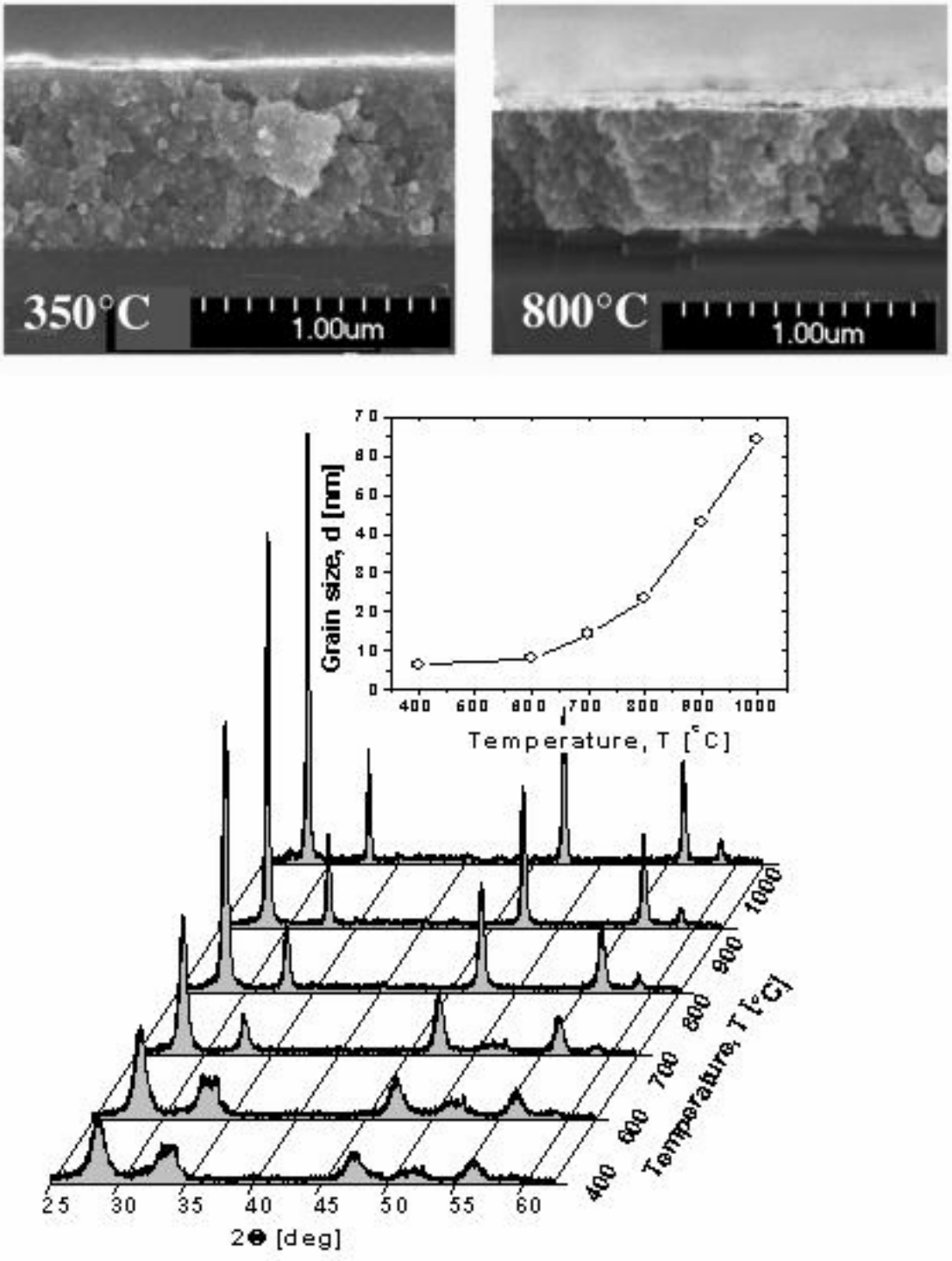

Fig.5.

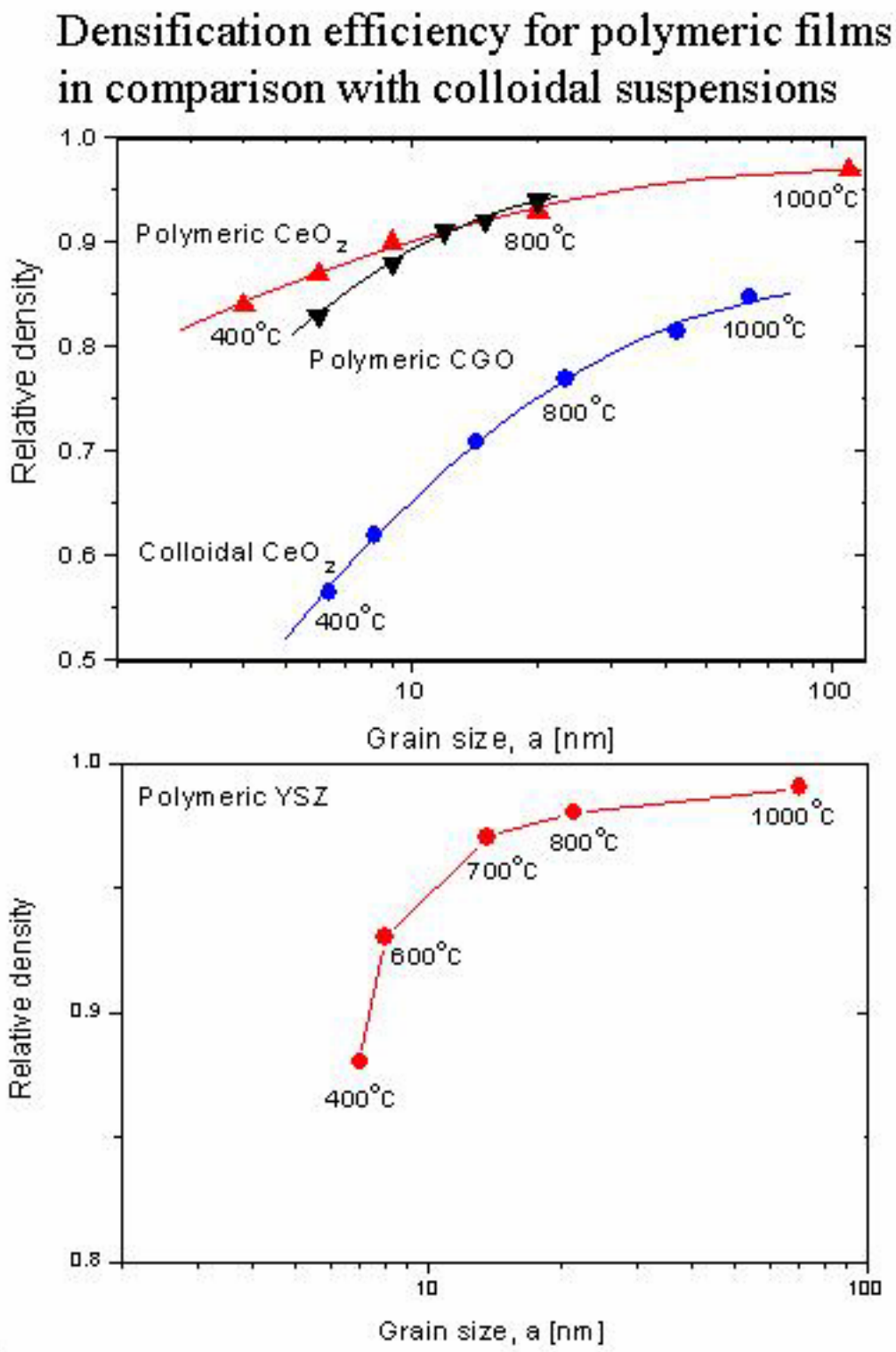
Densification efficiency for polymeric films in comparison with colloidal suspensions
Relative density
Grain size, a [nm]
Polymeric CeO2
400°C
800°C
1000°C
Polymeric CGO
Colloidal CeO2
Polymeric YSZ
600°C
700°C

Fig. 6.

Grain size versus time for different annealing temperatures.
The grain size is shown to stagnate
after approximately 2 hours at each temperature.

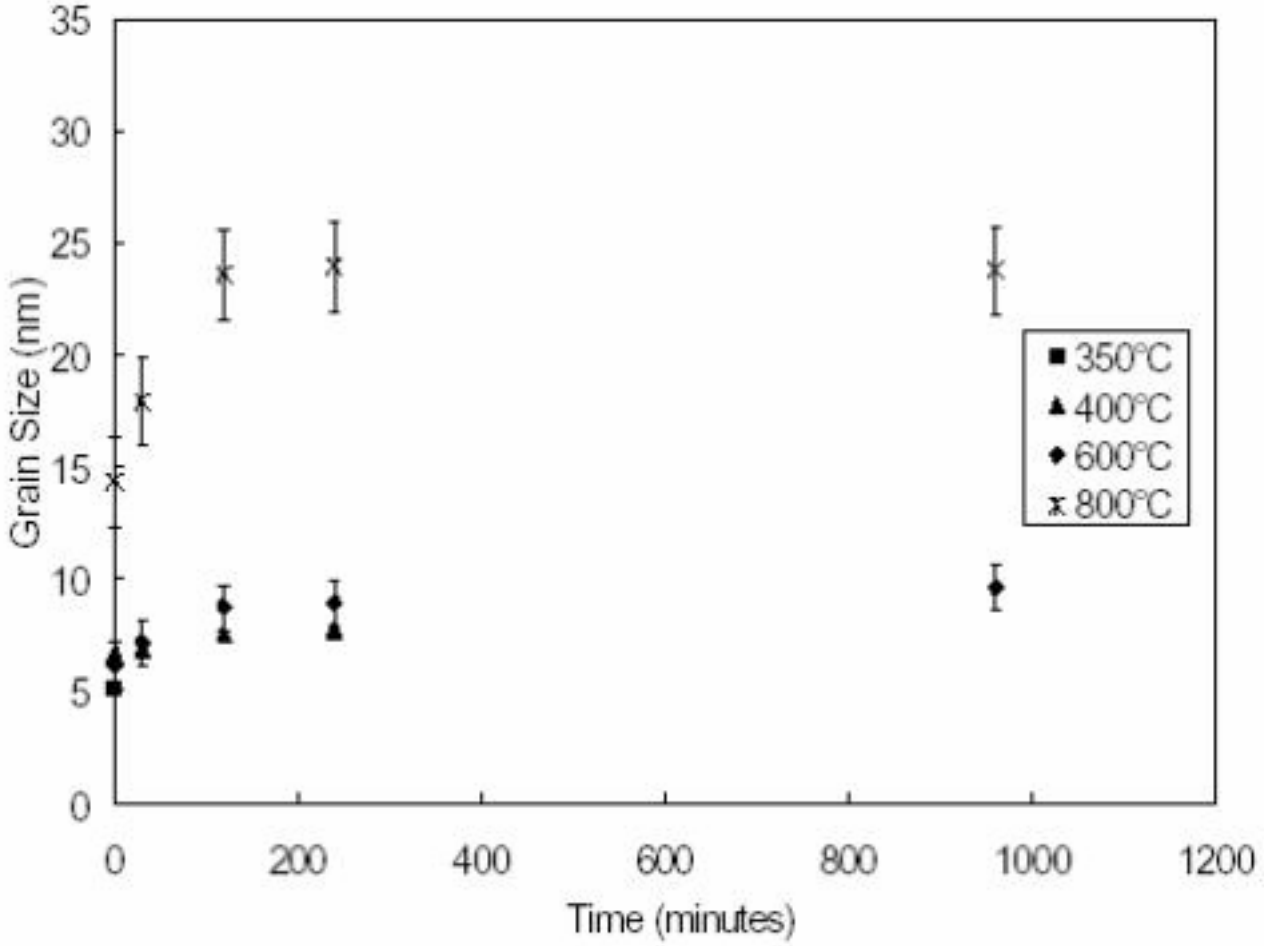

Fig.7.

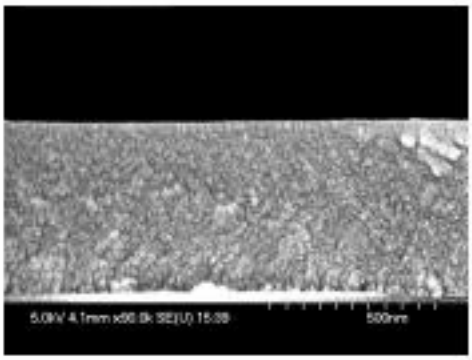

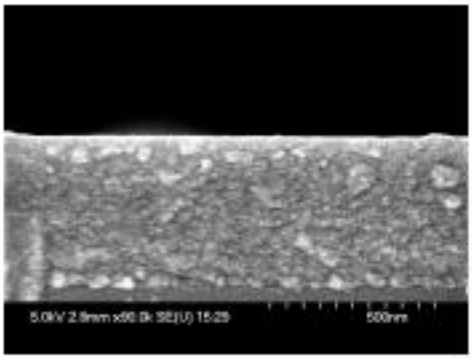

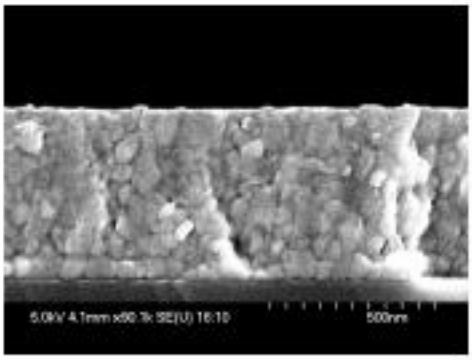

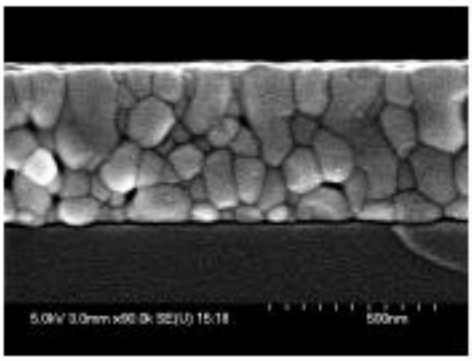

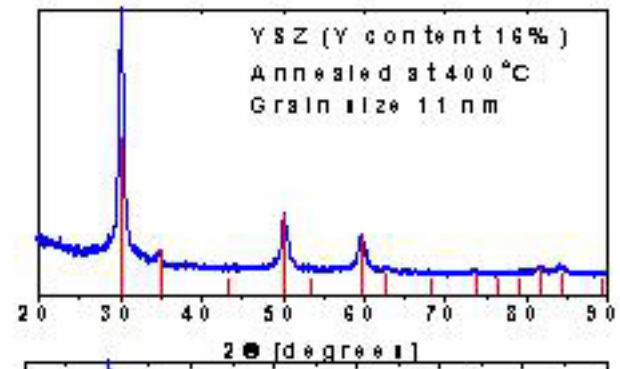
YSZ (Y content 16%)
Annealed at 400°C
Grain size 11 nm
20 30 40 50 60 70 80 90
2θ [degree]

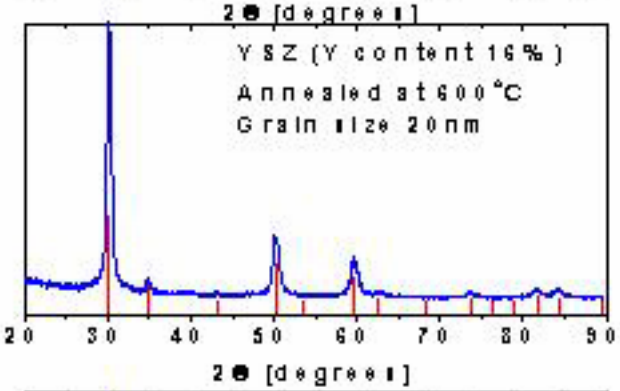
YSZ (Y content 16%)
Annealed at 600°C
Grain size 20nm
20 30 40 50 60 70 80 90
2θ [degree]

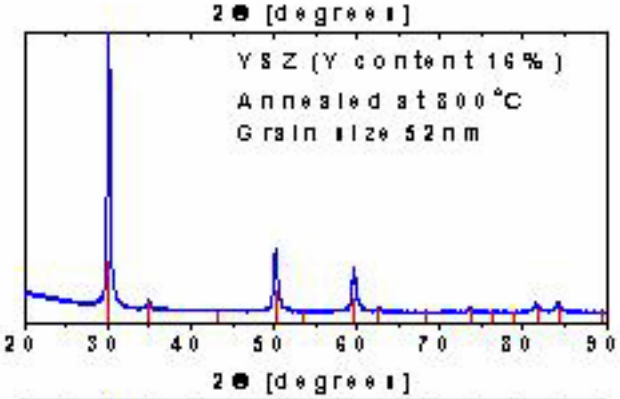
YSZ (Y content 16%)
Annealed at 800°C
Grain size 52nm
20 30 40 50 60 70 80 90
2θ [degree]

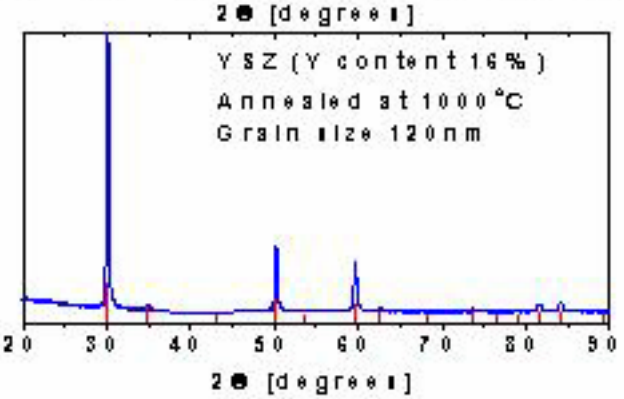
YSZ (Y content 16%)
Annealed at 1000°C
Grain size 120nm
20 30 40 50 60 70 80 90
2θ [degree]

Fig. 8.

High resolution transmission electron micrograph
of a 70 nm thick YSZ film annealed at 350°C for 1 minute.
Bar = 5nm.

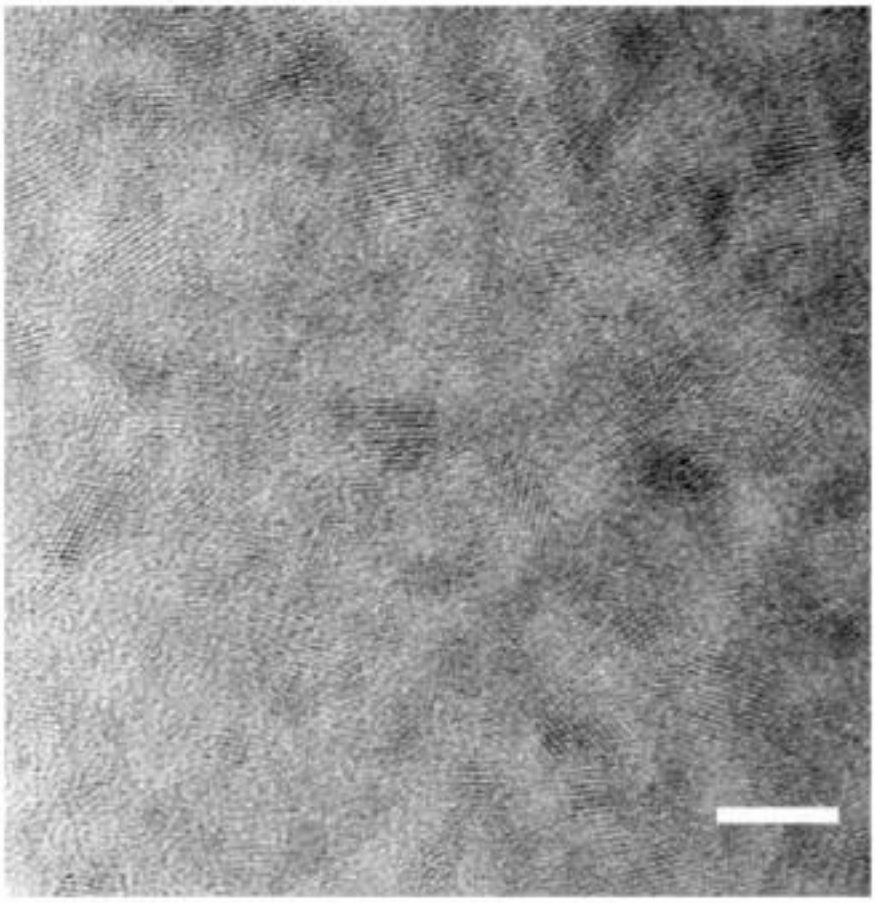

Fig.9.

Conductivity measurements of
YSZ polymeric films (8 and 16% Y) on sapphire

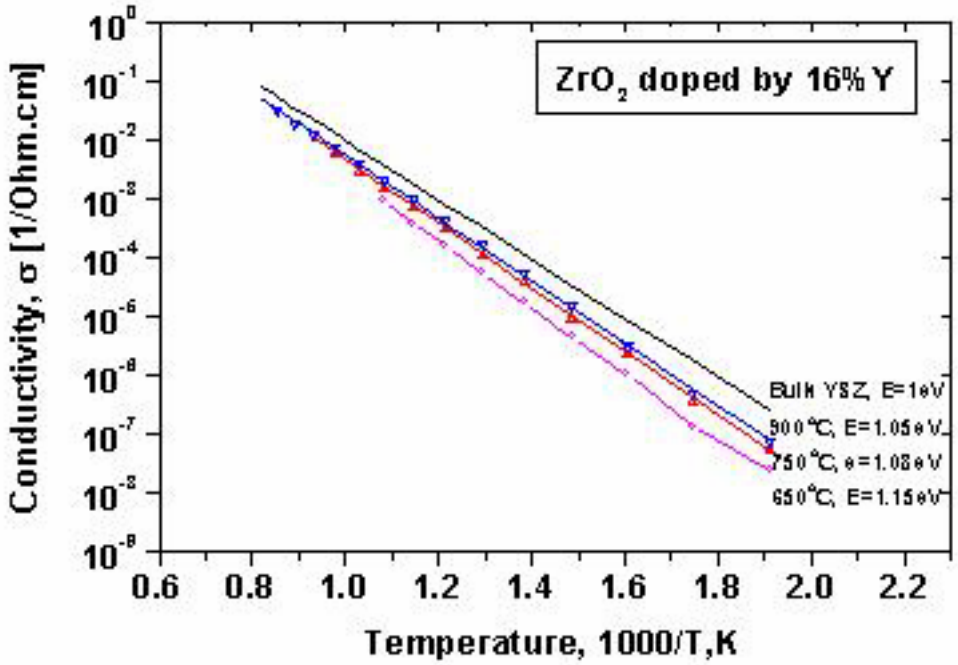

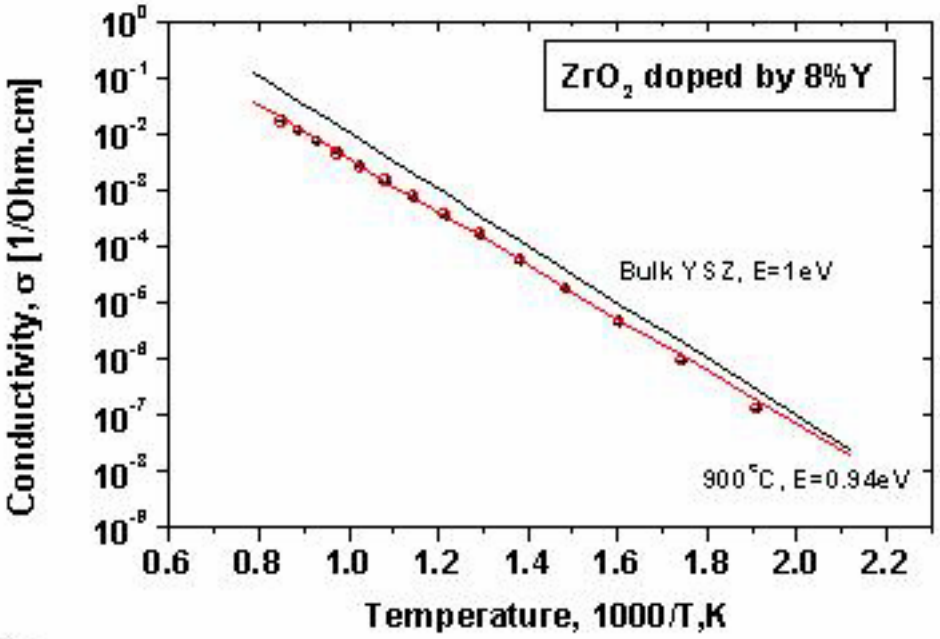

Fig. 10.

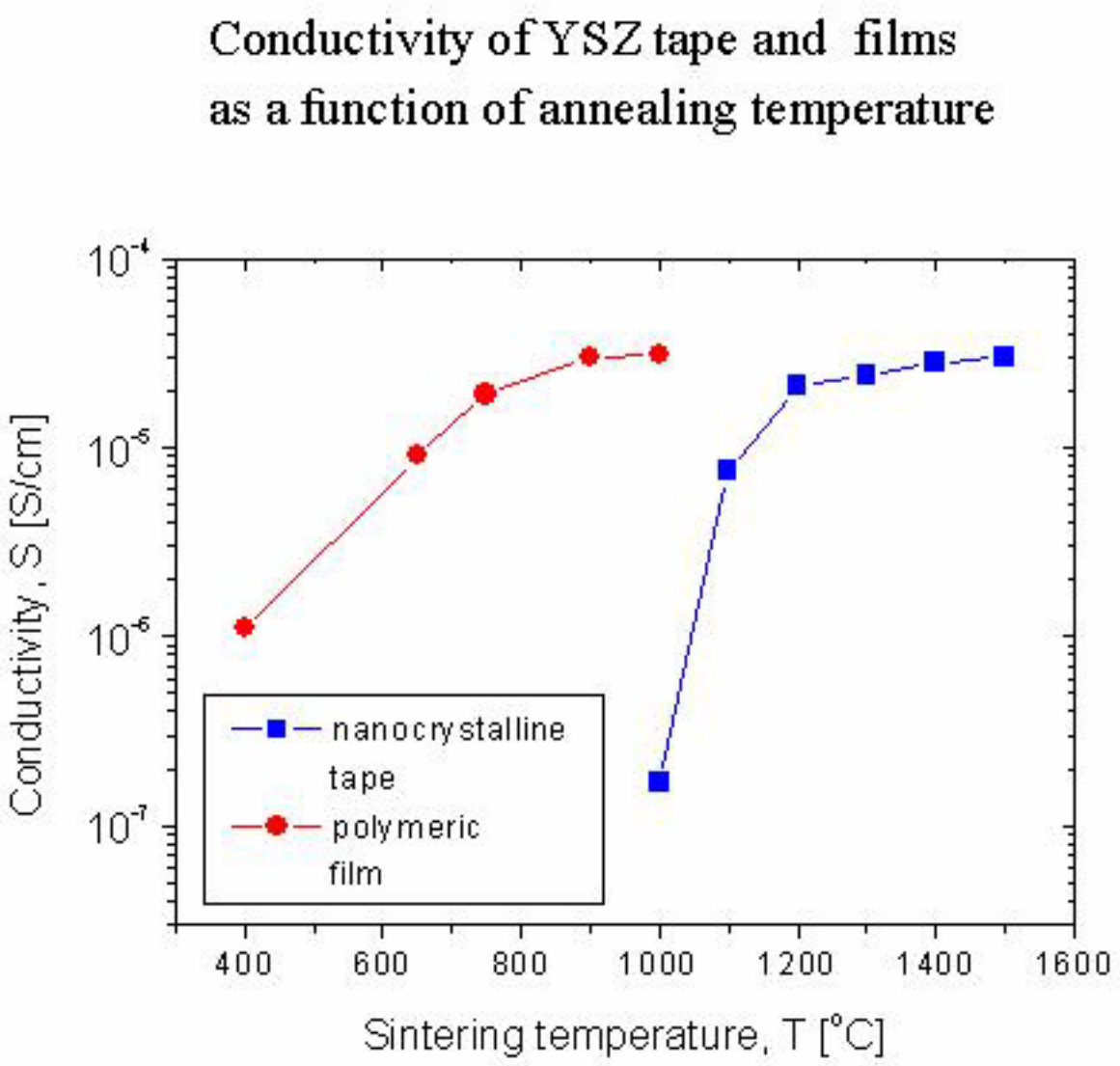
Conductivity of YSZ tape and films
as a function of annealing temperature
Conductivity, S [S/cm]
10^-4
10^-5
10^-6
10^-7
nanocrystalline tape
polymeric film
400
600
800
1000
1200
1400
1600
Sintering temperature, T [°C]

Fig.11.

Porous YSZ-CeO_2 layer on sapphire substrate. (Before densification).

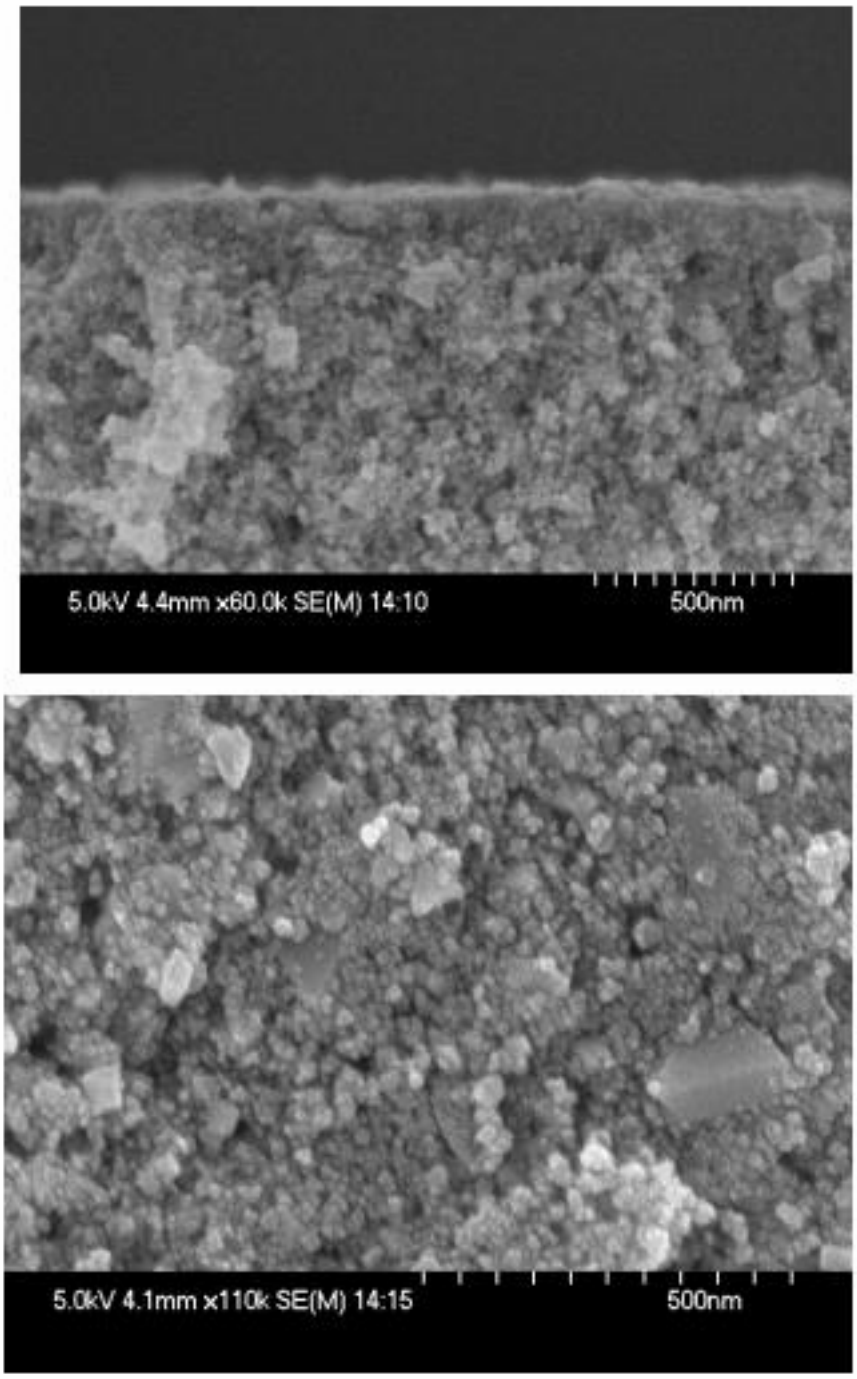

Fig. 12.

Dense YSZ-CeO_2 (from polymer precursor) layer on sapphire substrate.

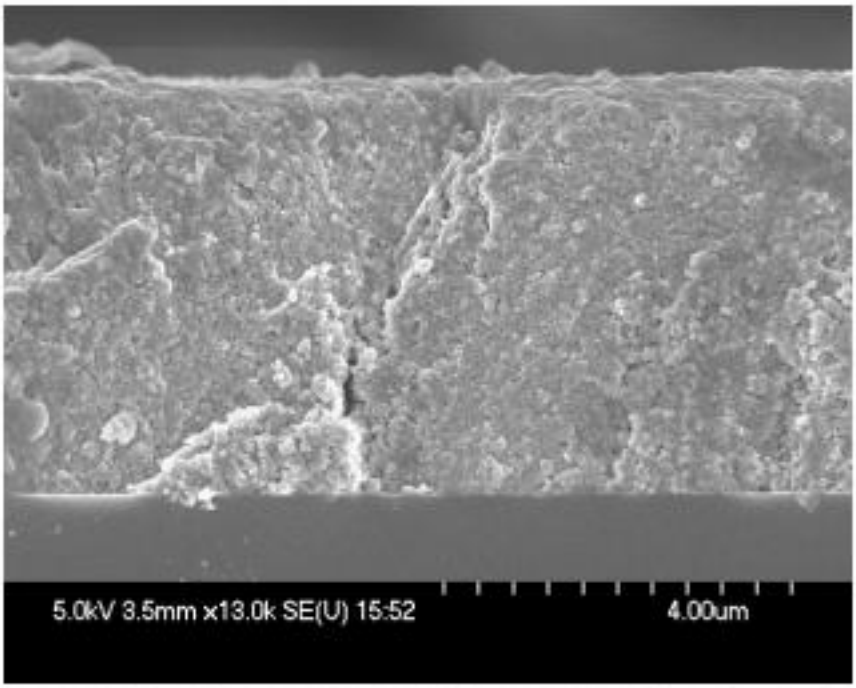

A

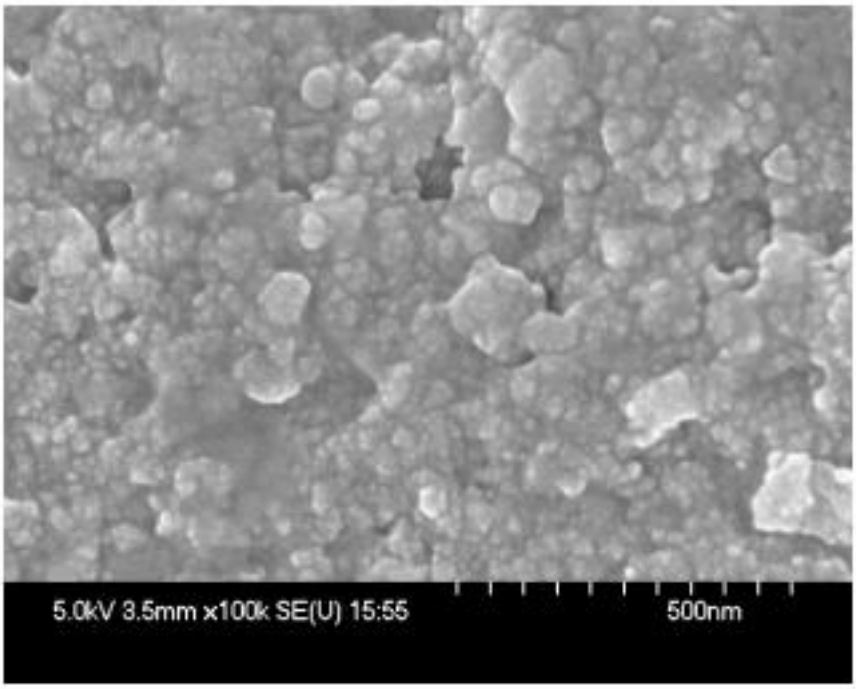

B

Fig. 13.

SEM surface images of $YSZ/CeO_2/LSM$ composite

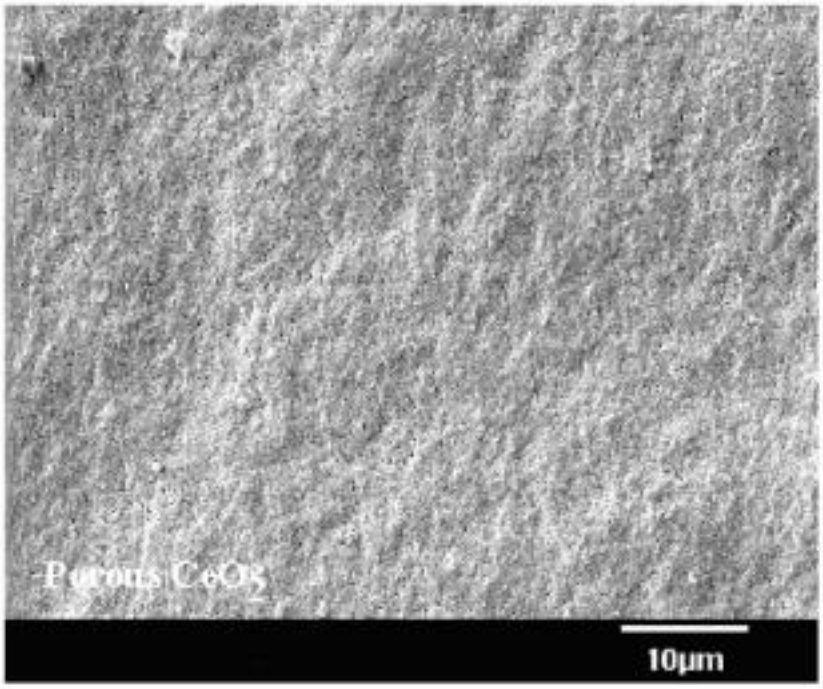

Nanoporous CeO_2 layer on LSM

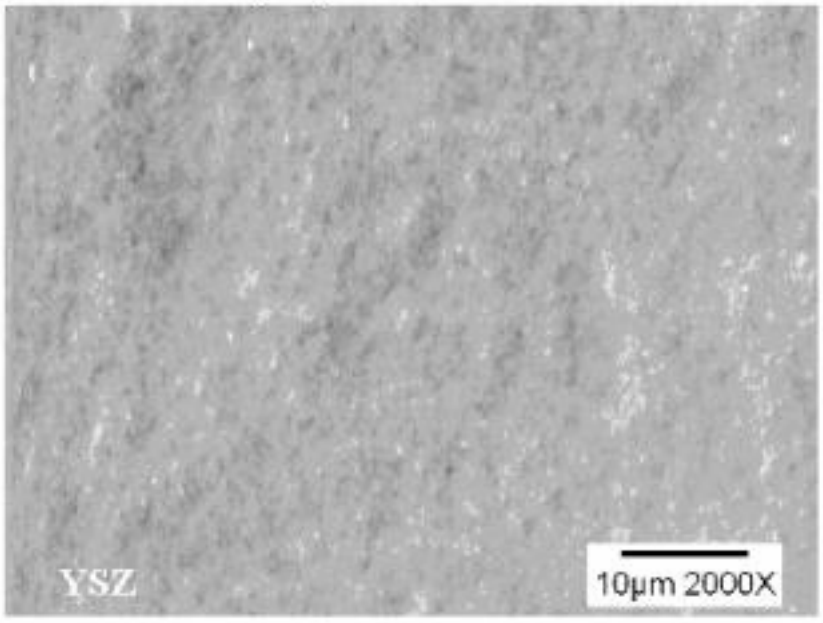

Dense YSZ layer

Fig. 14.

SEM cross section images of YSZ/CeO_2/LSM composite

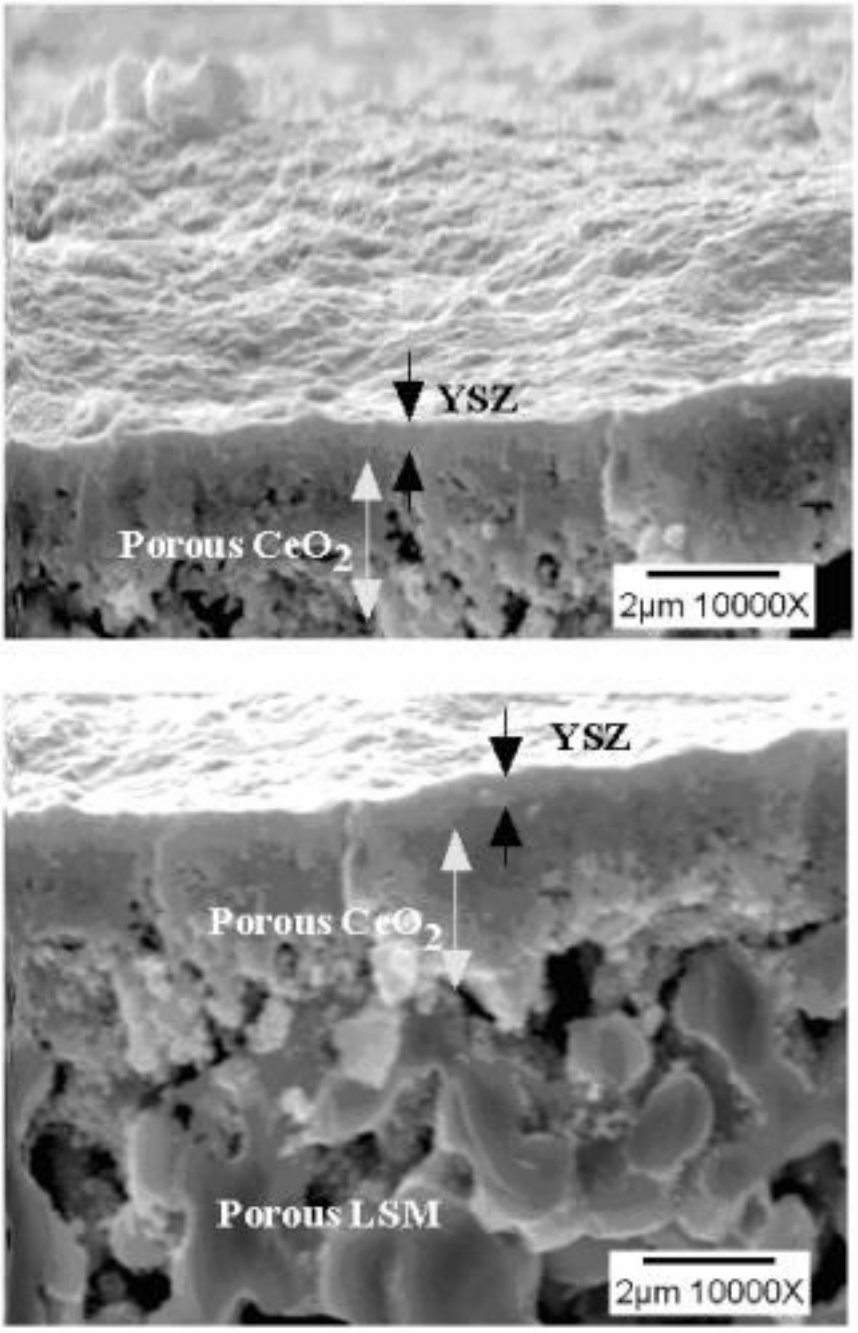

Fig. 15.

Composite structure
macroporous LSM – nanoporous CGO – dense YSZ

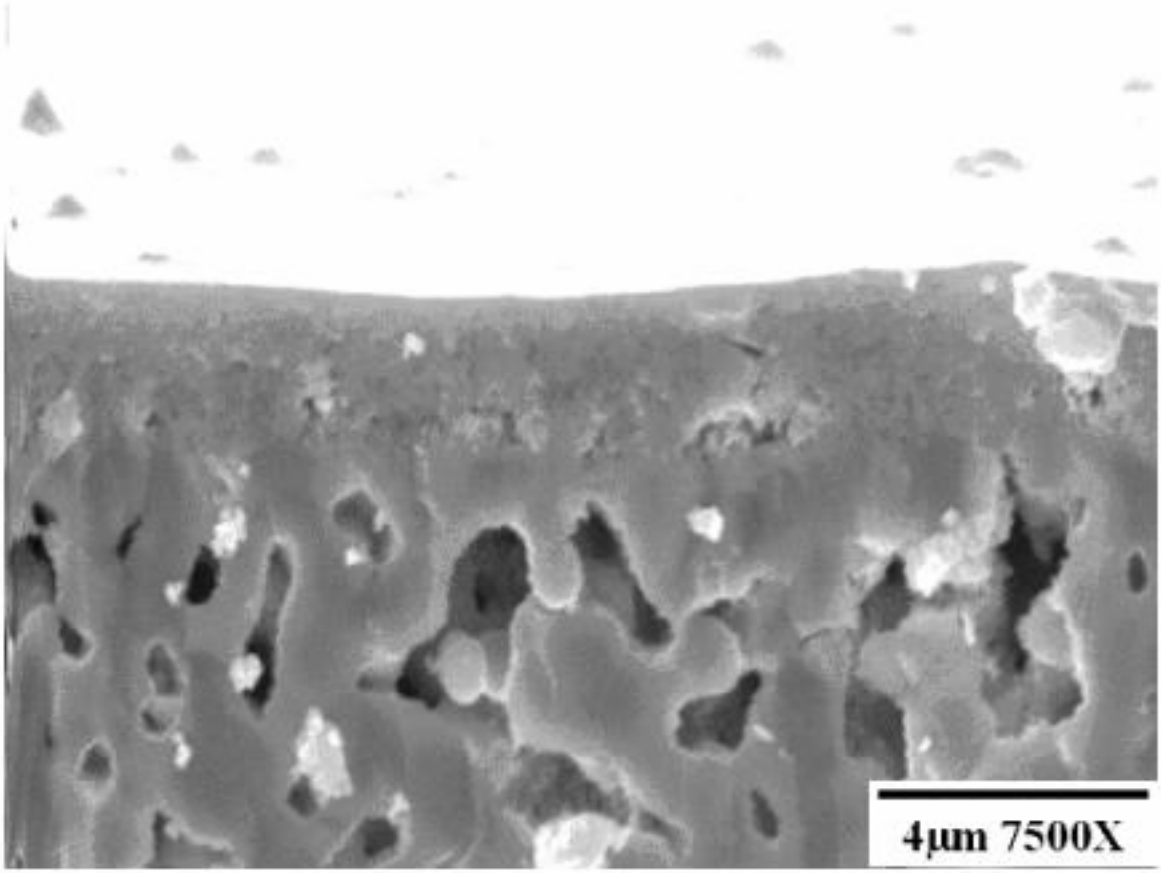

Dense YSZ layer in porous colloidal CGO layer
on porous LSM cathode annealed at 900°C

Fig. 16.

Area surface conductance of different ionic and mixed conductors calculated from surface exchange coefficient

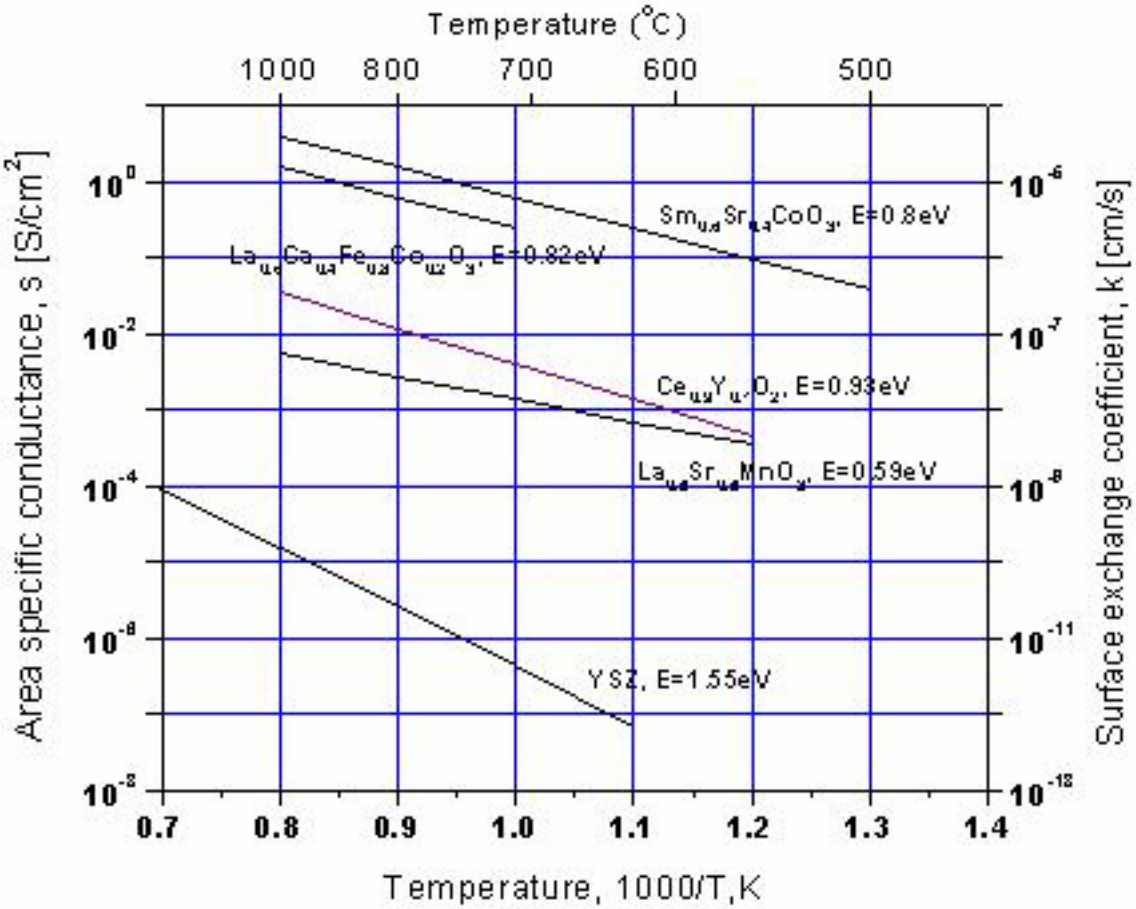

R.Doshi et all ; J.Electrochem.Soc,146 (1999);
B.Steele, Sol.St. Ionics, 75 (1995) and 86-88 (1996).

Equation used for this calculation:

$$\sigma_S = 2e^2\left(\frac{A \cdot d}{M \cdot KT}\right) \cdot k$$

where
e - electron charge;
A - Avogadro number;
d - specific weight;
M - molecular weight;
K - Boltzman constant;
T - absolute temperature.

Fig.17.

Current density calculated from surface exchange coefficient for different mixed conductors

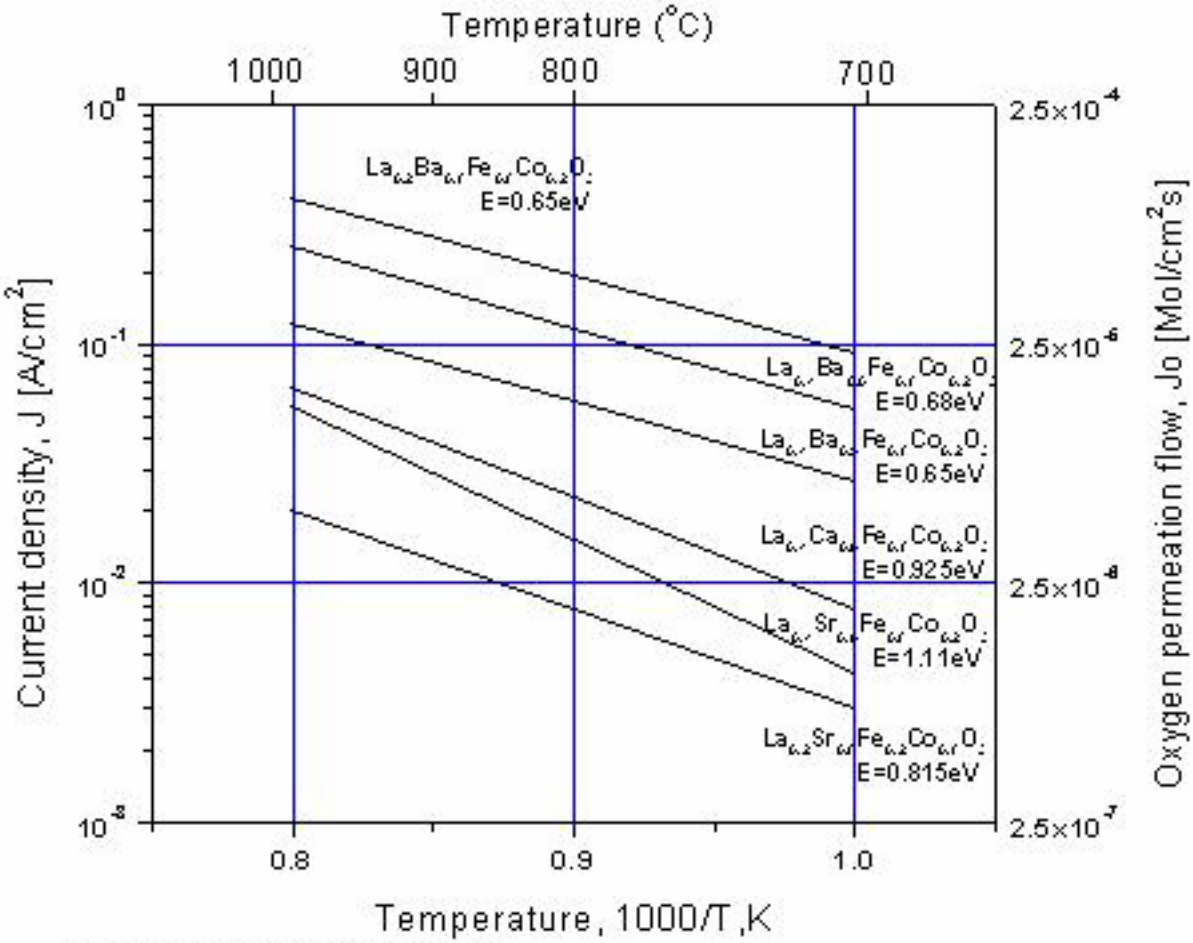

Y.Ma, "MRS Bulletin,24 (1999);
K.Huang et all, El-Chem. and Sol.-St.Lett., 2 (1999), J.El-Chem.Soc", 148 (2001);
C.Tsai et all, J. of Amer.Ceram.Soc., 81 (1998).

Equation used for this calculation: $J = 4 \cdot A \cdot e^2 J_O$

where
J - current density;
A - Avagadro number;
e - electron charge;
Jo- oxygen permeation flow

Fig.18.

Electrical conductivity of different ionic and mixed conductors calculated from diffusion coefficient

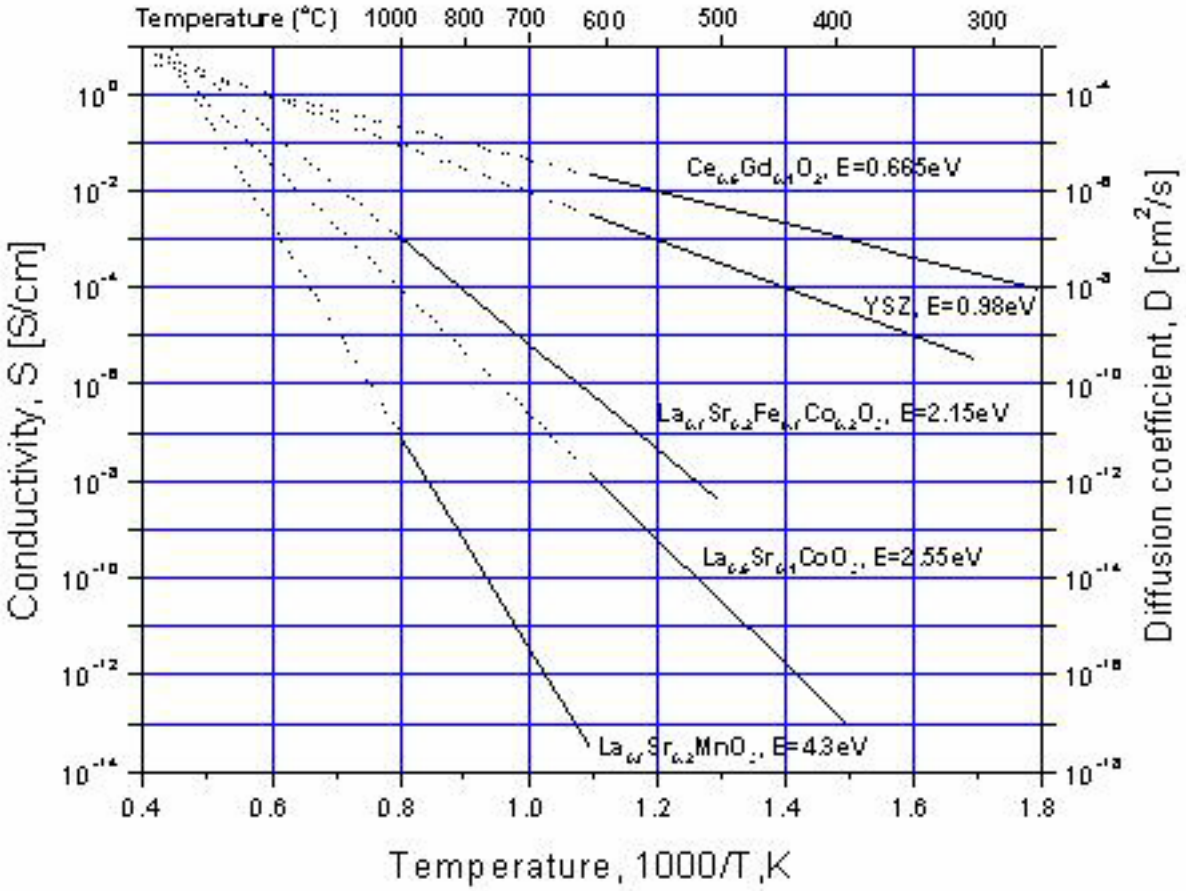

A.Belsner et all, Sol.St. Ionics, 57 (1996).
H.Inaba et all, Sol.St. Ionics, 83 (1996).

Equation used for this calculation:

$$\sigma_V = 2e^2\left(\frac{x \cdot A \cdot d}{M \cdot KT}\right) \cdot D$$

where
e - electron charge;
x – vacancy molar ratio;
A - Avagadro number;
d - specific weight;
M - molecular weight;
K - Bolzman constant;
T - absolute temperature.

Fig.19.

4.0: Appendix

- Reports prepared and presented
- Papers submitted for publication and/or published

Appendix A

Presentation at the SECA Core Technology Program Review Meeting
Pittsburgh, PA
November 16, 2001

EMARC

ELECTRONIC MATERIALS APPLIED RESEARCH CENTER

Overview of
DOE Contract No.: DE-AC-26-99FT40710
at University of Missouri-Rolla

Low Temperature Cathode Supported Electrolytes

Harlan U. Anderson (presenter)
Igor Kosacki
Vladimir Petrovsky
Wayne Huebner

Presented at
SECA Core Technology Program
Review Meeting at

Hyatt-Regency at Pittsburgh International Airport
Pittsburgh, PA

November 16, 2001

UMROLLA

EMARC
ELECTRONIC MATERIALS APPLIED RESEARCH CENTER

ACHIEVEMENTS – FY 1999-2000

- Films of 16% Y:ZrO_2 Characterized
  - Ionic conductivity of <50 nm grain one micron thick films measured to room temperature *(conductivity of the grains dominates).*
  - Grain size <50 nm for annealing temperatures <800°C.
  - Produced >95% theoretical dense YSZ at 600°C.
- Films of Undoped and Gd Doped CeO_2 Characterized
  - The electrical conductivity of both doped and undoped CeO_2 show grain size dependence.
  - Ionic conductivity of nanocrystalline Gd doped CeO_2 less than that of the microcrystalline.

UMROLLA

EMARC

ELECTRONIC MATERIALS APPLIED RESEARCH CENTER

ACHIEVEMENTS – FY 2000-2001

- Films of 16% Sc:ZrO_2 Characterized
  - o The ionic conductivity is about one order of magnitude higher than YSZ.
  - o Electronic Conductivity becomes significant for oxygen activity less than 10^{-14} atm.
- Developed Cathode Substrate for Deposition of 0.5 to 2 Micron Thick YSZ Films for Use as Electrolyte in SOFCs
  - o Fabricated porous LSM substrates
  - o Synthesized nanoscale CeO_2 suspensions for deposition onto LSM substrate
    - Control of cathode surface porosity to sizes <0.1 micron
    - 3-5 micron thick CeO_2 layers planarize LSM substrate to surface roughness <0.1 micron.
    - Developed a graded LSM substrate

UMROLLA

EMARC

ELECTRONIC MATERIALS APPLIED RESEARCH CENTER

- Developed a process by which 1-5μm thick electrolyte layers can be produced on dense and porous substrate without shrinkage.
- Improved Clean Room *(in order to make electrolyte of areas larger than 0.2 cm^2 our existing clean room must be improved)*
  - Doubled size.
  - More filters and air flow.
  - This was completed March 1, 2001.

EMARC
ELECTRONIC MATERIALS APPLIED RESEARCH CENTER

Research Planned for FY 2001-2002

- Continue Optimization of the Cathode Substrate. Evaluate:
  - The influence of porous CeO_2 layer on SOFC performance.
  - The influence of the addition of LSCF into CeO_2 layer on SOFC performance.
  - The influence of the conductivity of the CeO_2 layer on SOFC performance.
- Make Single Cell Fuel Cell Measurements
  - Cell performance as a function of electrolyte thickness and temperature.
    - YSZ electrolyte
    - CeO_2 electrolyte
  - Cell performance as a function of electrode composition.
    - Anode
    - Cathode

UMROLLA

EMARC
ELECTRONIC MATERIALS APPLIED RESEARCH CENTER

- Continue Studies Related to Placing Thin Electrolyte Films onto Porous Substrates
  - o Polymer precursor onto a graded substrate.
  - o Transfer of dense films to a porous substrate.
  - o Nanocrystalline/polymer precursor composites.

EMARC

ELECTRONIC MATERIALS APPLIED RESEARCH CENTER

Thin Film Processing

Water Soluble Salts

- *Zr chloride*
- *La carbonate*
- *Co nitrate*
- *Ce nitrate*
- *Y nitrate*
- *Sr carbonate*
- *Fe nitrate*

Precursor Preparation

Rheological Characterization

- *H_2O*
- *Nitric acid*
- *Ethylene glycol*
- *Citric acid*

Spin Coating

- *Brewer Science Spin-coater*
- *Class 100 clean room*
- *0-6000 rpm*

Repeat

Baking

- *Hot plate: ±1 °C uniformity*
- *320°C - 2 min*

Crystallization

- *400-1000°C*

Electrical Characterization

Microstructural Characterization

UMROLLA

EMARC

ELECTRONIC MATERIALS APPLIED RESEARCH CENTER

YSZ thin film annealed at 400°C for 2 hrs. dg= 6nm

UMROLLA

EMARC

ELECTRONIC MATERIALS APPLIED RESEARCH CENTER

Optical Density of YSZ thin Films on Si Substrates

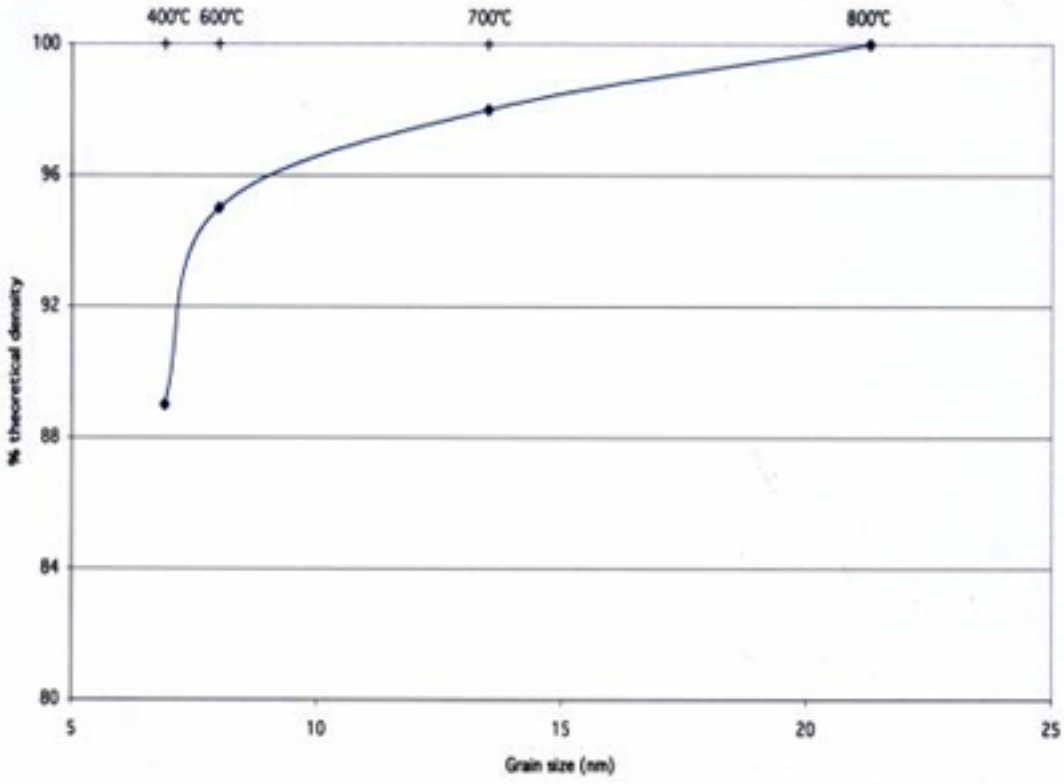

UMROLLA

EMARC

ELECTRONIC MATERIALS APPLIED RESEARCH CENTER

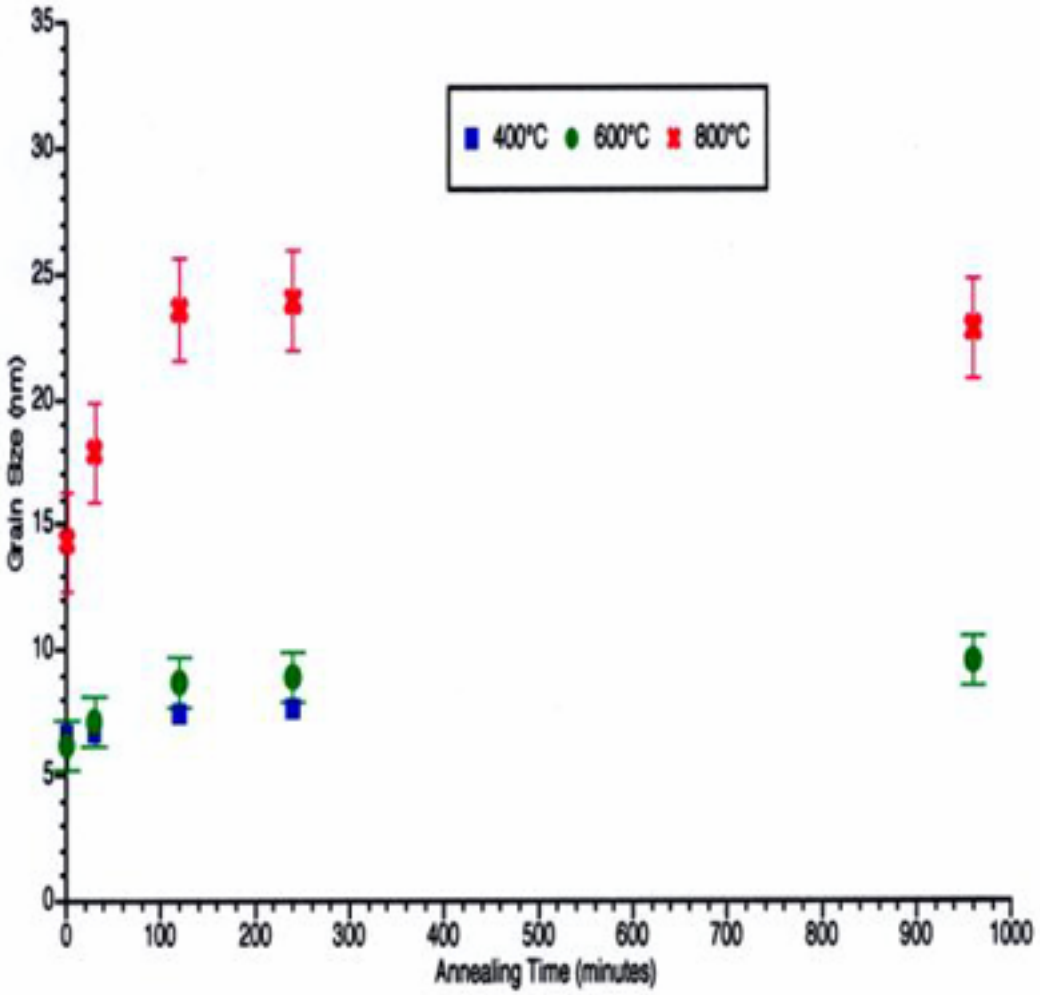

Grain size versus time for unsupported YSZ thin films at different annealing temperatures.

UMROLLA

EMARC

ELECTRONIC MATERIALS APPLIED RESEARCH CENTER

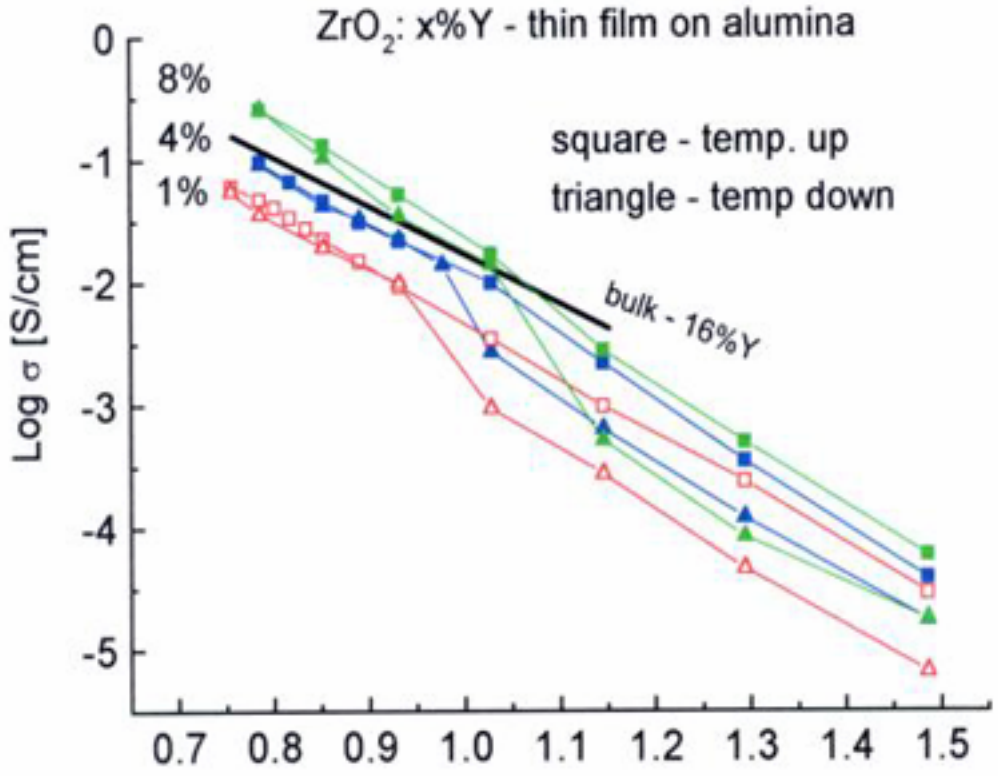

UMROLLA

EMARC

Electronic Materials Applied Research Center

- **Films of Undoped and Gd Doped CeO_2 Characterized**
  - **The electrical conductivity of both doped and undoped CeO_2 show grain size dependence**
  - **Ionic conductivity of nanocrystalline Gd doped CeO_2 less than that of the microcrystalline**
  - **Electronic conductivity enhanced as grain size decreases below 50 nm**

EMARC

ELECTRONIC MATERIALS APPLIED RESEARCH CENTER

Electronic & Ionic Conductivity of CeO_2:20Gd

Elecronic conductivity

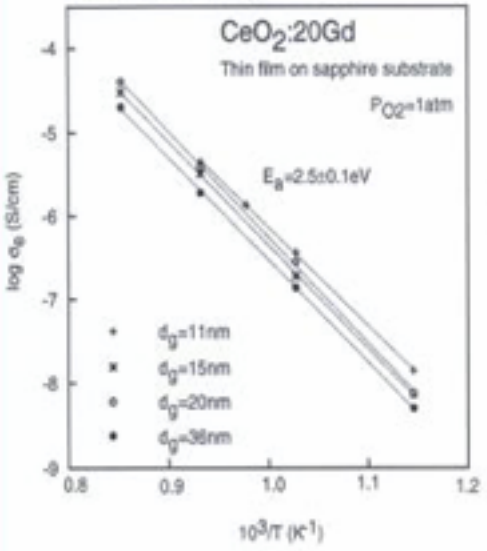

Ionic conductivity

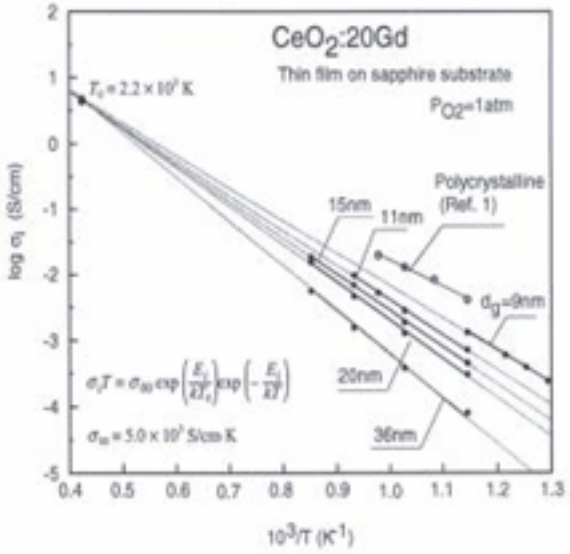

σ_i (microcrystalline) > σ_i (nanocrystalline)

E_i = 0.8eV

E_i = 1.3 → 1.0 eV

(d_g = 36 → 9 nm)

grain boundary conductivity

Ref.1 S. Lubke and H. D. Wiemhofer. Solid State Ionics, 117:229-243, (1999).

UMROLLA

EMARC

ELECTRONIC MATERIALS APPLIED RESEARCH CENTER

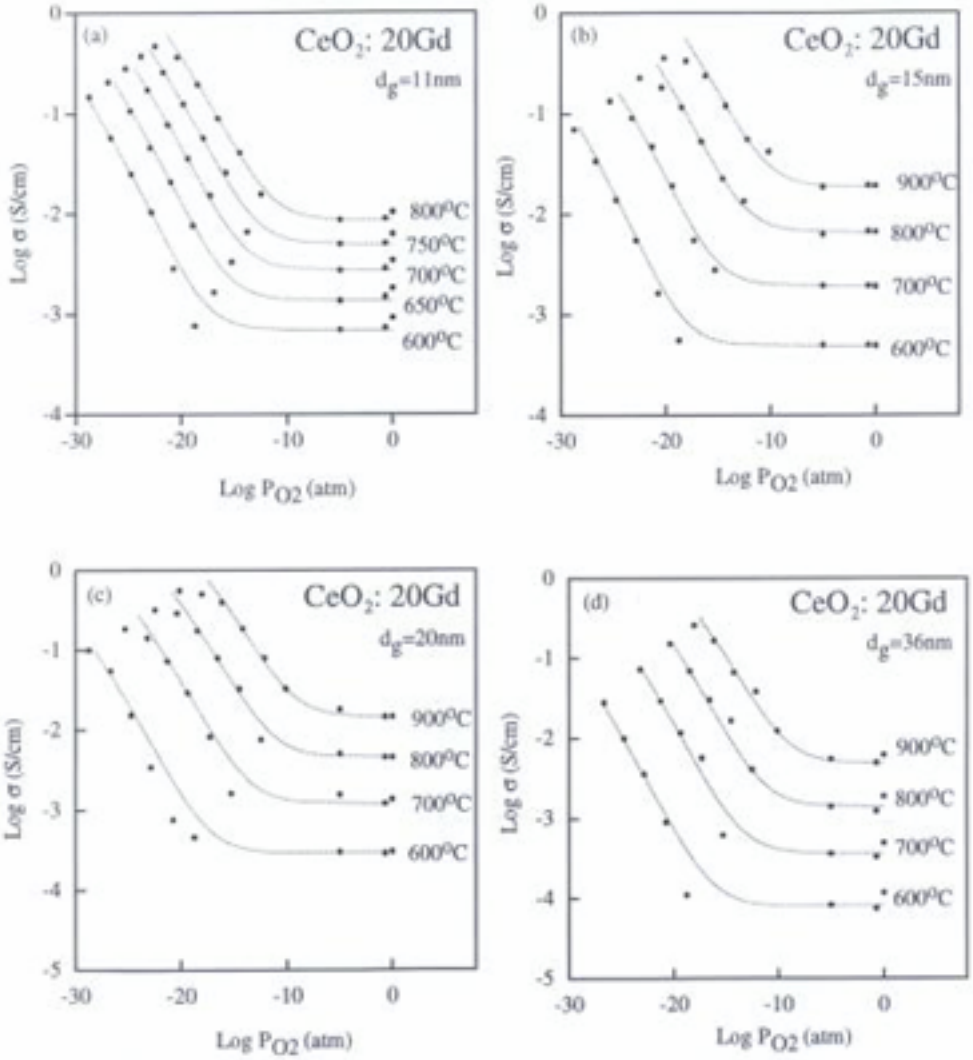

The electrical conductivity of CeO_2 :20Gd thin films as a function of oxygen partial pressure and temperature. (a) d_g = 11 nm (b) 15 nm (c) 20 nm (d)36 nm. Film thickness = 300 - 400 nm.

UMROLLA

EMARC
ELECTRONIC MATERIALS APPLIED RESEARCH CENTER

- **Electrolyte Layers Produced on Porous Cathode**
  - **Transfer from dense substrate**
    - **Rock salt substrate**
    - **Polymide substrate**
  - **From polymer precursor**

UMROLLA

EMARC
ELECTRONIC MATERIALS APPLIED RESEARCH CENTER

YSZ on $Ni:ZrO_2$

1 Layer
~ 70 nm

EMARC
ELECTRONIC MATERIALS APPLIED RESEARCH CENTER

Thin Film Membrane Research

2 Layers
~ 150 nm

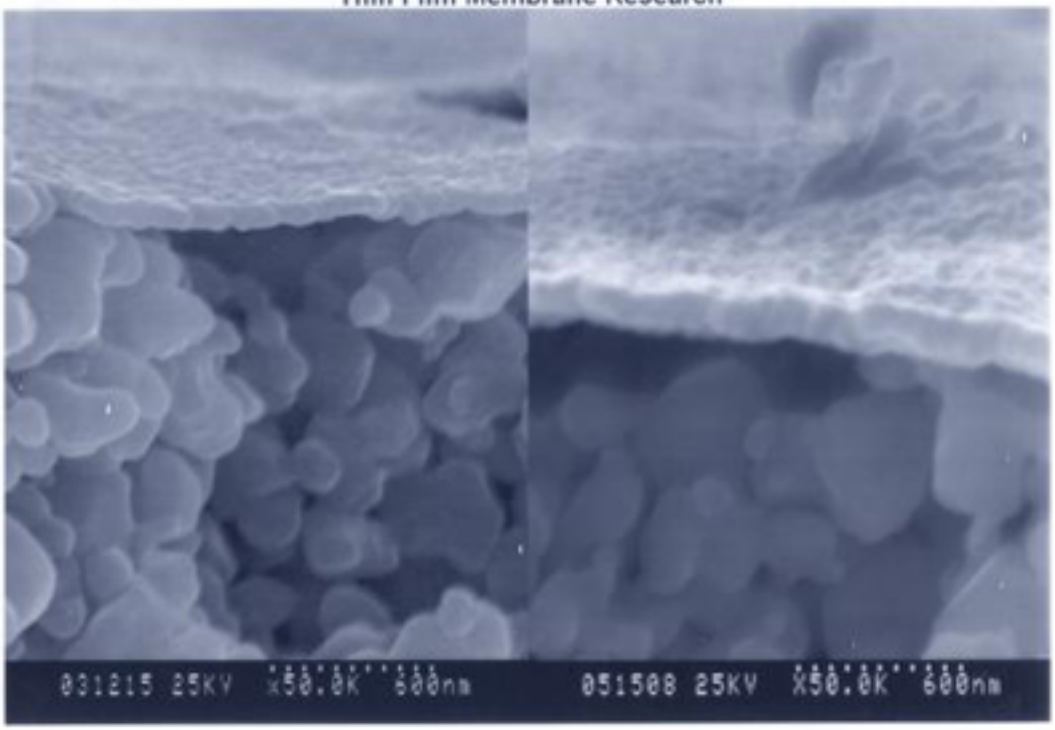

UMROLLA

EMARC

ELECTRONIC MATERIALS APPLIED RESEARCH CENTER

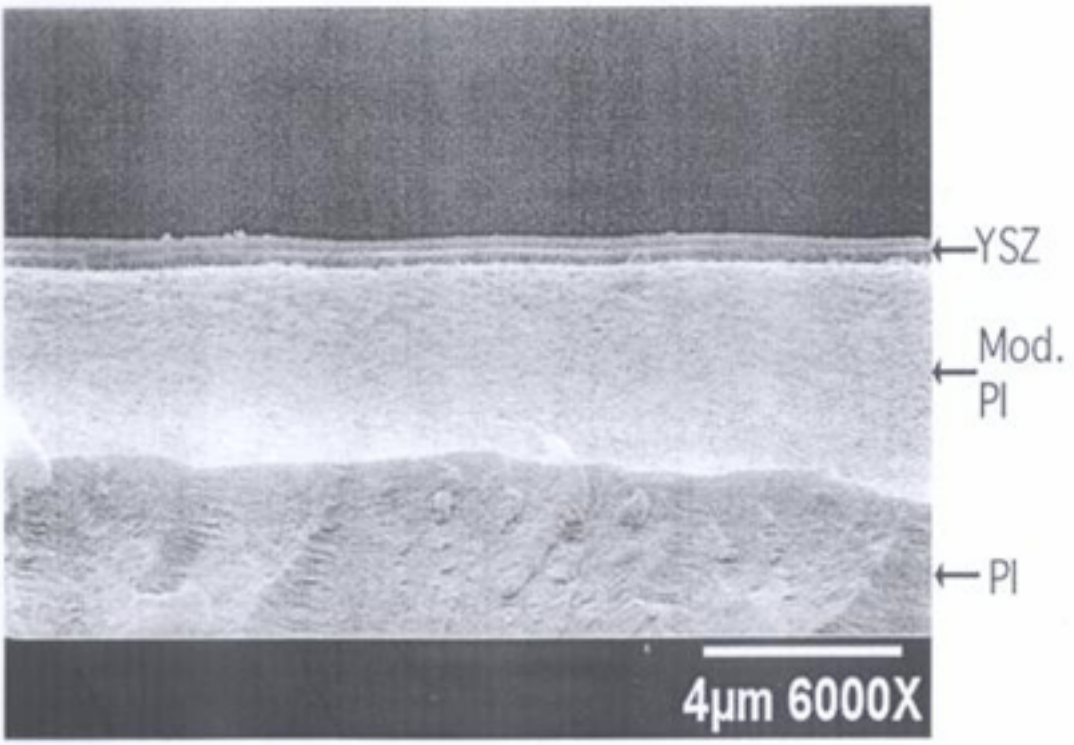

0.4 µm polymer precursor-derived YSZ film on modified polyimide (PI) substrate.

UMROLLA

EMARC

ELECTRONIC MATERIALS APPLIED RESEARCH CENTER

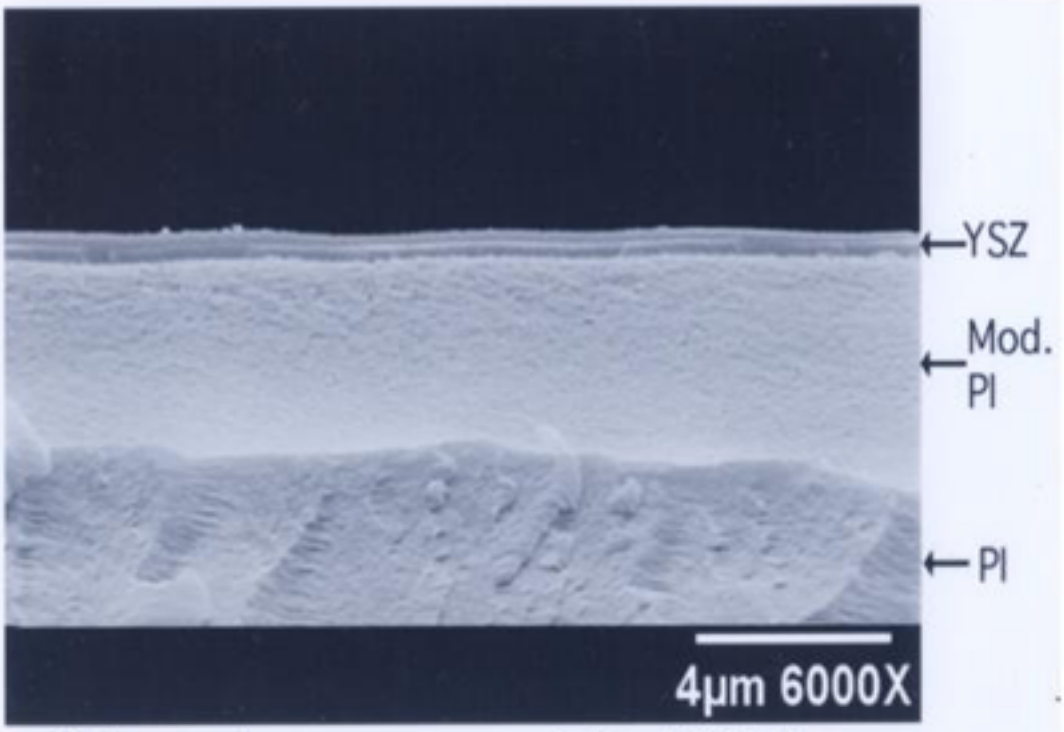

0.4 µm polymer precursor-derived YSZ film on modified polyimide (PI) substrate.

UMROLLA

EMARC
ELECTRONIC MATERIALS APPLIED RESEARCH CENTER

- **Films of 16% Sc:ZrO_2 Characterized**
  - **The ionic conductivity is about one order of magnitude higher than YSZ**
  - **Electronic conductivity becomes significant for oxygen activity less than 10^{-14} atm**

EMARC

ELECTRONIC MATERIALS APPLIED RESEARCH CENTER

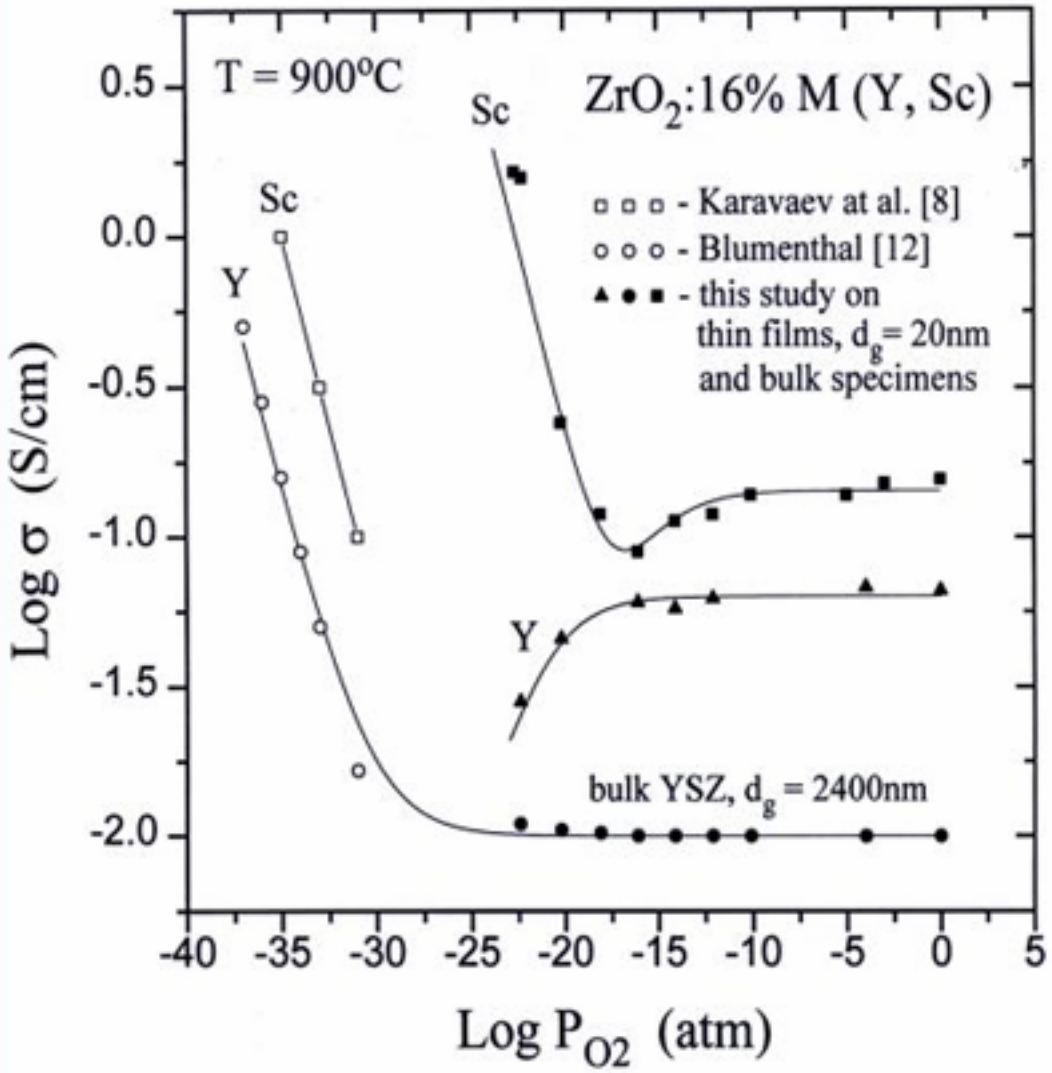

UMROLLA

EMARC

Electronic Materials Applied Research Center

- **Developed Cathode Substrate for Deposition of 0.5 to 2 Micron Thick YSZ Films for Use as Electrolyte in SOFC's.**
  - **Fabricated porous LSM substrates**
  - **Synthesized nanoscale CeO_2 suspensions for deposition onto LSM substrate**
    - **Control of cathode surface porosity to sizes < 0.1 micron**
    - **3-5 micron thick CeO2 layers planarize LSM substrate to surface roughness < 0.1 micron**

UMROLLA

EMARC

ELECTRONIC MATERIALS APPLIED RESEARCH CENTER

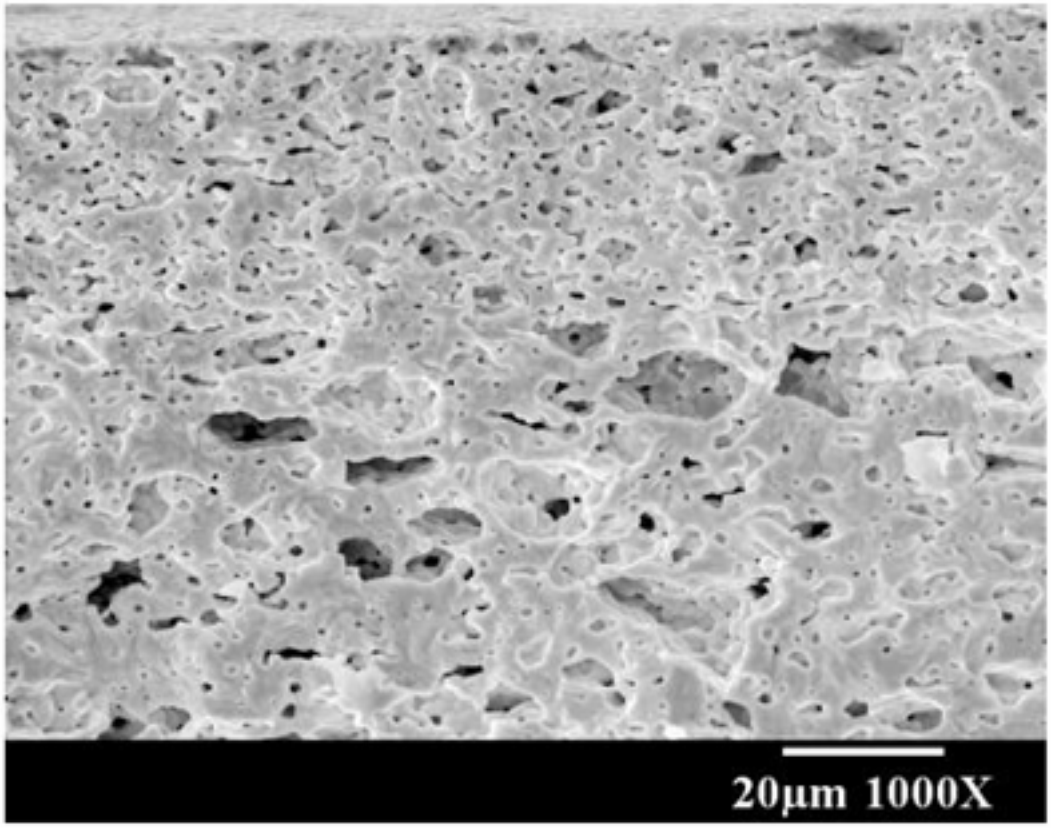

The cross section of LSM with fine carbon and coarse carbon sintered at 1350°C for 2h

UMROLLA

EMARC

ELECTRONIC MATERIALS APPLIED RESEARCH CENTER

Double layer LSM Substrate

Surface

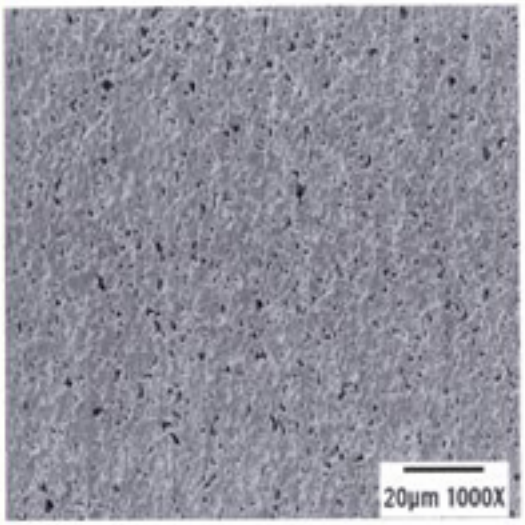

Cross Section

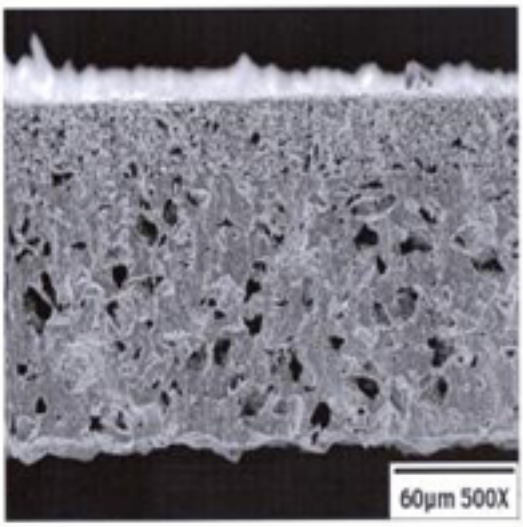

Sintered at 1350^{O}C

UMROLLA

EMARC

Electronic Materials Applied Research Center

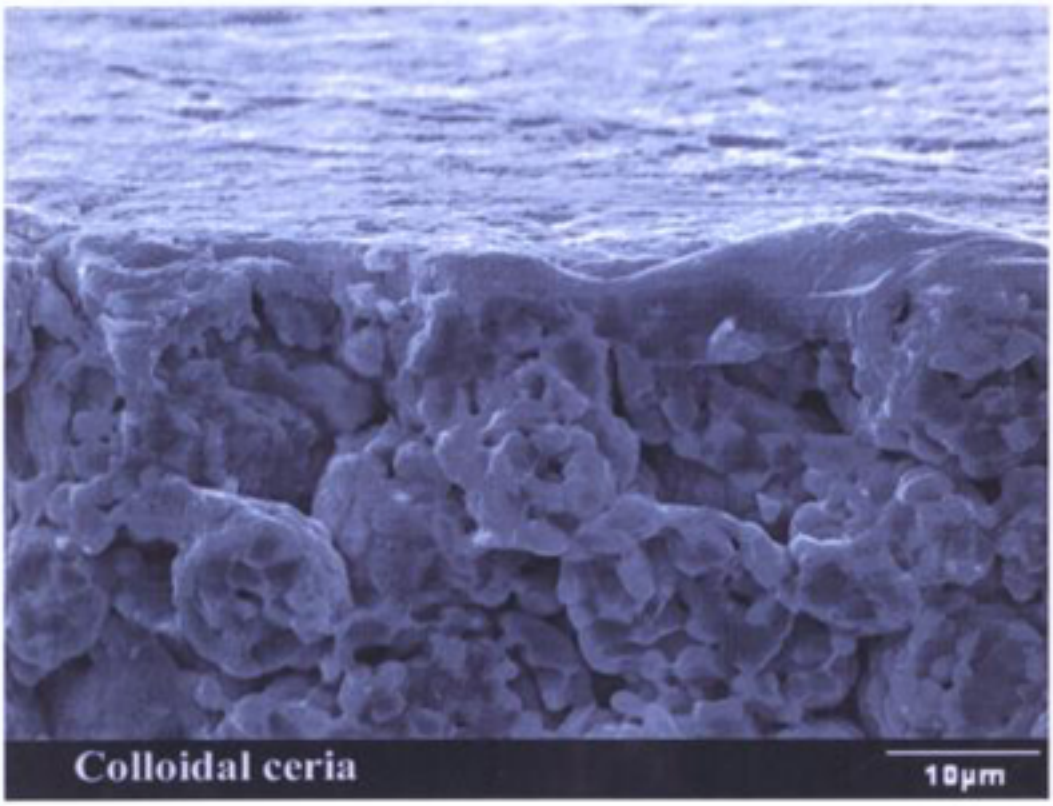

50% dense 5nm grain size ceria film on porous LSM. Sintered 600°C / 4 hours.

UMROLLA

EMARC
ELECTRONIC MATERIALS APPLIED RESEARCH CENTER

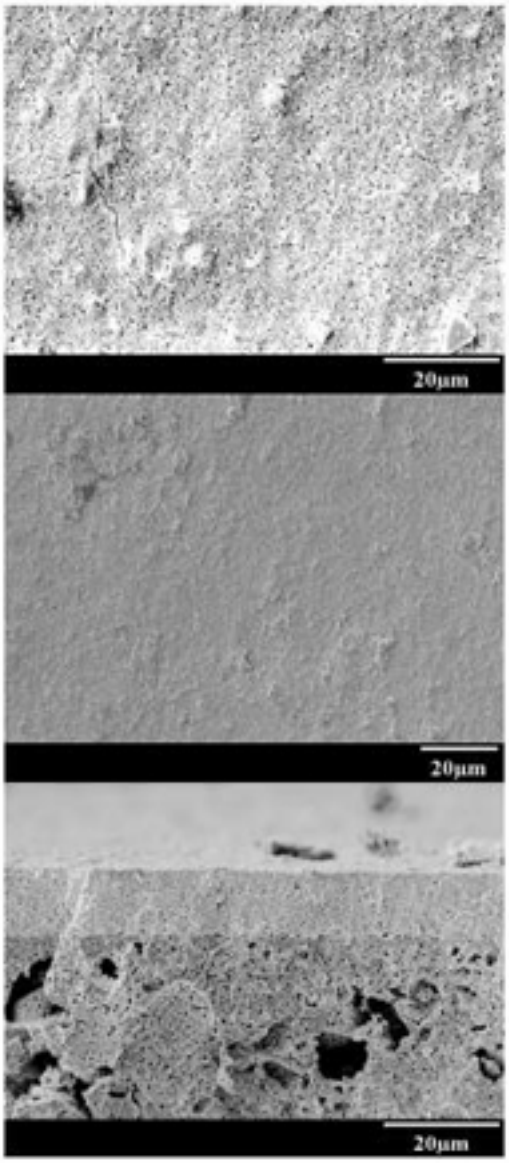

(A)

(B)

(C)

Fig. 1 YSZ layer on porous LSM substrate (low magnification). (A) – low density coating; (B) – high density coating; (C) - cross section of the structure.

UMROLLA

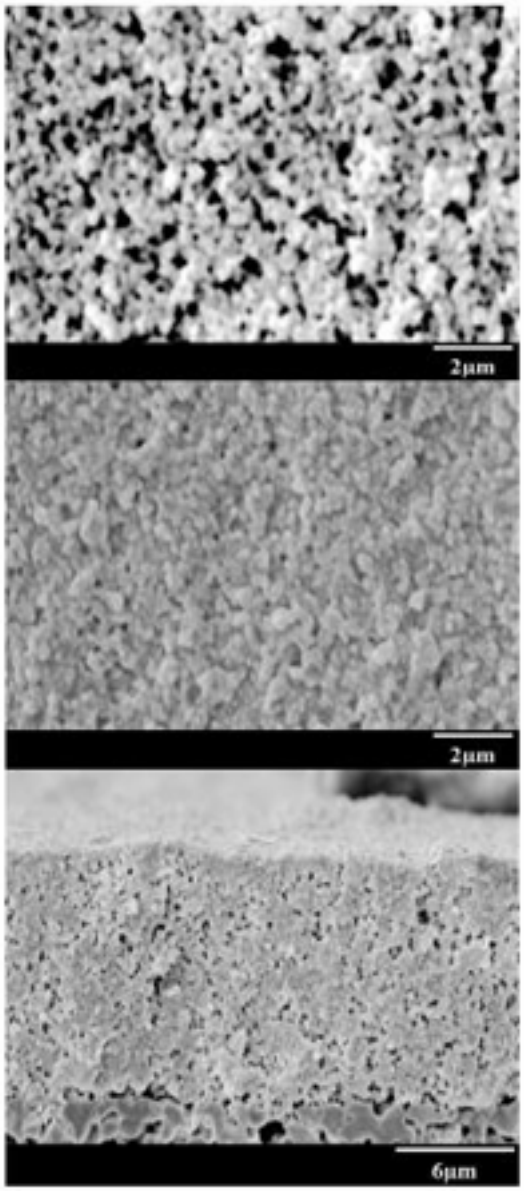

(A)

(B)

(C)

Fig. 2 YSZ layer on porous LSM substrate (high magnification). (A) – low density coating; (B) – high density coating; (C) - cross section of the structure.

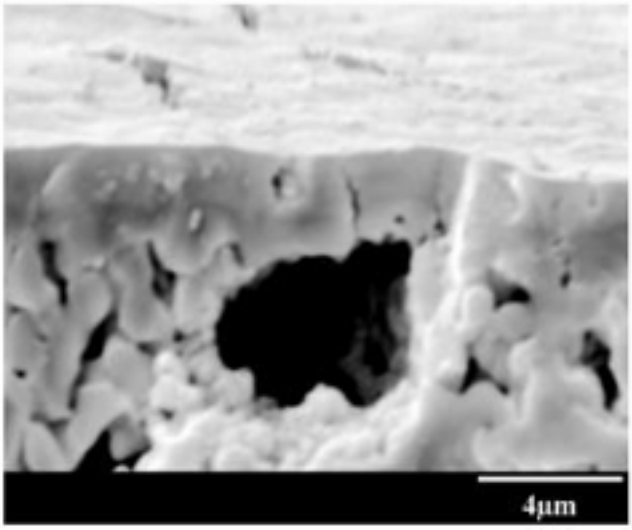

(A)

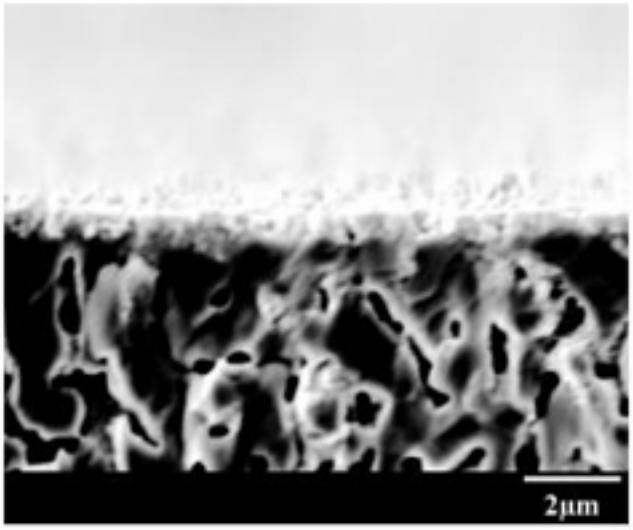

(B)

Fig. 7 Ceria layer on porous LSM substrate. The examples of the cross section (high magnification). (A) – composition 1 (~2.5μm layer); (B) – composition 3, one deposition (~0.5μm layer);

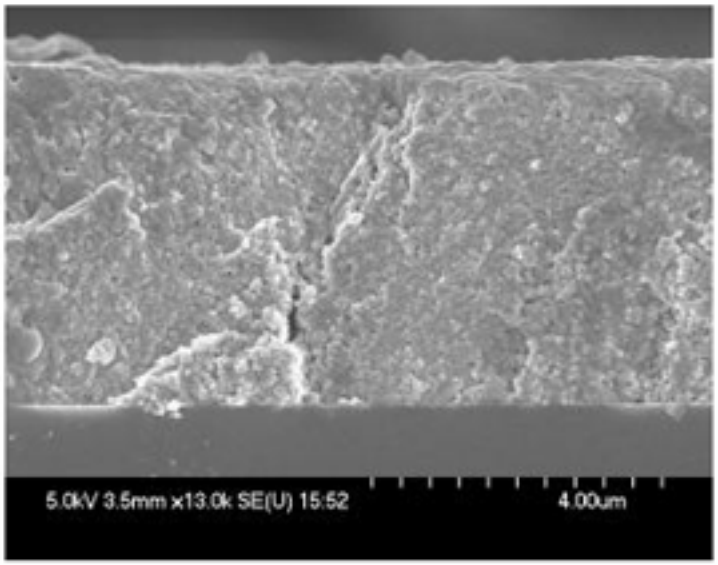

(A)

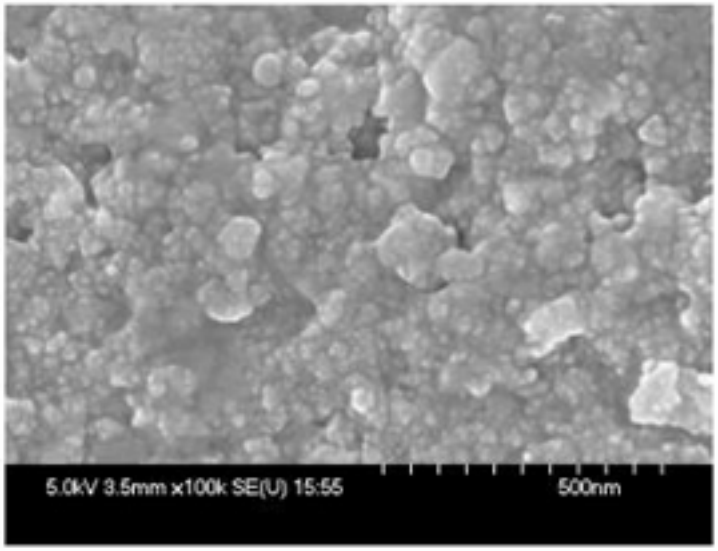

(B)

Fig. 10 Dense YSZ-CeO_2 layer on dense substrate. (After low temperature densification).(A) – cross section; (B) – surface image;

EMARC

ELECTRONIC MATERIALS APPLIED RESEARCH CENTER

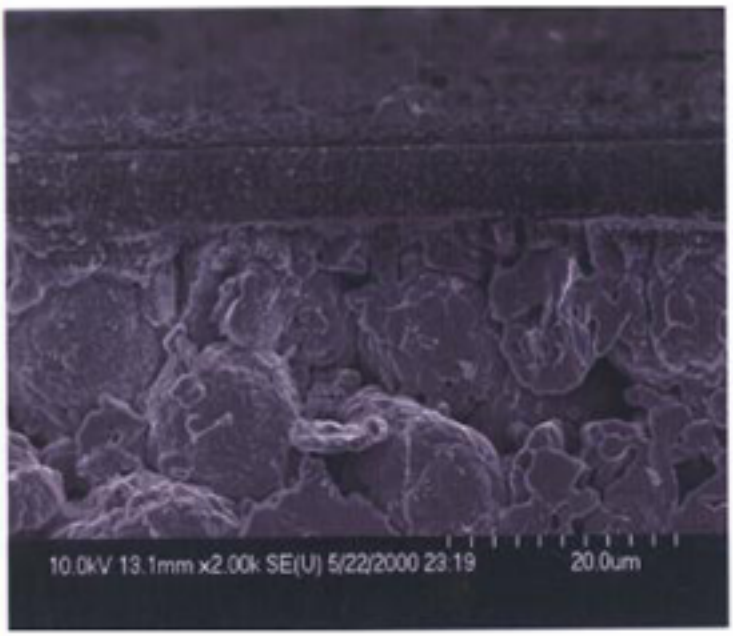

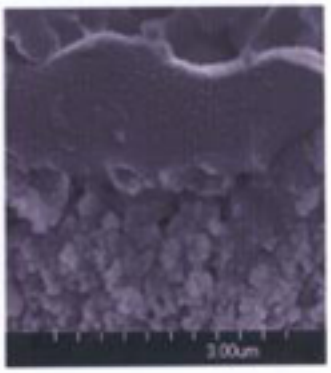

Field-emission SEM micrograph of a YSZ / Colloidal CeO_2 / spray-pyrolized LSM composite. $CeO_2 = 5\ \mu m$, $YSZ = 0.5\ \mu m$. Annealed at 800°C.

UMROLLA

Appendix B

Defect and Mixed Conductivity in Nanocrystalline Doped Cerium Oxide

T. Suzuki, I. Kosacki, and H.U. Anderson

J. Am. Ceram Soc., 85[6] 1492-98 (2002)

journal

J. Am. Ceram. Soc., 85 [6] 1492–98 (2002)

Defect and Mixed Conductivity in Nanocrystalline Doped Cerium Oxide

Toshio Suzuki, Igor Kosacki,*,† and Harlan U. Anderson*

Electronic Materials Applied Research Center, University of Missouri, Rolla, Missouri 65401

The results obtained from a study on the microstructure and the electrical properties of Gd-doped CeO_2 thin films were reported. Dense, nanocrystalline films on sapphire substrates are prepared using a polymeric precursor spin coating technique. The electrical conductivity was studied as a function of temperature and oxygen activity and correlated with the grain size. For nanocrystalline Gd-doped CeO_2 thin films, the ionic conductivity increased with decreasing activation energy as the grain size decreased. A conductivity model was developed to analyze P_{O_2} behavior of the electrical conductivity. Using the conductivity model, the hopping energy of electron conduction and the enthalpy of oxygen vacancy formation were determined for different microstructures.

I. Introduction

CERIUM OXIDE doped with divalent or trivalent cations has sufficiently high ionic conductivity to make it attractive for use in applications such as an electrolyte in solid oxide fuel cells.[1] Many dopants such as alkaline, rare-earth oxides and Y_2O_3 have extensive solubility in the Ce sublattice. Replacing Ce^{4+} with +2 or +3 cations results in the creation of anion vacancy sites to compensate charges in the lattice. As a result, a solid electrolyte with predominantly ionic conductivity for oxygen over an extended temperature and oxygen partial pressure range may be produced. Therefore, to receive higher conductivity, selection of dopant is very important, with those dopants with the ionic radius close to that of matrix being the best. From this point of view, Gd, Y, and Sm are likely candidates as dopants for CeO_2.[2]

On the other hand, doped CeO_2 displays mixed conductivity (mixture of ionic and electronic conductivity) at low oxygen partial pressure. In reducing atmospheres oxygen may be lost from the lattice, which results in reduction of Ce^{4+} to Ce^{3+}, which generates electrical carriers, oxygen vacancies, and electrons. Therefore, both electronic and ionic conductivity are enhanced in reduced atmosphere and mixed conductivity prevails.

Recent studies have shown that microstructure can be an additional influence on the electrical conductivity. So far, studies of the effects of microstructure on electrical properties of oxide materials have reported that it can alter and enhance electrical properties, as well as influence reaction kinetics in electrochemical devices. These studies show that nanocrystalline ZrO_2 displays 2 orders higher electrical conductivity than microcrystalline ZrO_2[3] and nanocrystalline undoped CeO_2 has increased electronic conductivity due to reduction in the enthalpy of oxygen vacancy formation.[4]

The objective of this research is to gain a systematic understanding of the influence of the microstructure on the nonstoichiometry and defect thermodynamics in Gd-doped CeO_2. In this paper the results of a study of the electrical properties of nanocrystalline Gd-doped CeO_2 thin films by impedance spectroscopy are presented. The electrical conductivity has been studied as a function of temperature and oxygen partial pressure (P_{O_2}). A conductivity model which had been reported[4] was used to fit the experimental data and analyze the P_{O_2} behavior of the electrical conductivity with thermodynamic parameters.

II. Electrical Conductivity Model

Information about the type of conductivity and temperature dependent parameters can be obtained by conducting measurements of electrical conductivity as a function of P_{O_2} and temperature and applying a model as shown below.

It is assumed that only ionic and electronic conductivity (σ_i and σ_e), which are controlled by the oxygen vacancy and electron concentration, exist and that the electron transport is attributed to a small polaron hopping mechanism with thermally activated electron mobility. The expression for total conductivity is given by

$$\sigma_t = \sigma_i + \sigma_e \tag{1}$$

where

$$\sigma_i = 2e[V_O^{\cdot\cdot}]\mu_{V_O^{\cdot\cdot}} = 2e[V_O^{\cdot\cdot}]\left(\frac{\mu_{io}}{T}\right)\exp\left(-\frac{E_i}{kT}\right) \tag{2}$$

$$\sigma_e = ne\mu_e = ne\left(\frac{\mu_{eo}}{T}\right)\exp\left(-\frac{E_h}{kT}\right) \tag{3}$$

where e, E_h, E_i, n, and $[V_O^{\cdot\cdot}]$ are the charge of an electron, the hopping energy, the activation energy for ionic mobility, and the electron and oxygen vacancy concentrations, respectively. μ_{eo} and μ_{io} are temperature-independent constants in the expression for mobility.

Using Kroger–Vink notation,[5] ionic defects for Gd-doped CeO_2 can be introduced by the reactions

$$O_O^{\times} \rightarrow V_O^{\cdot\cdot} + 2e' + \tfrac{1}{2}O_2 \tag{4}$$

$$Gd_2O_3 \xrightarrow{CeO_2} 2Gd'_{Ce} + V_O^{\cdot\cdot} + 3O_O^{\times} \tag{5}$$

where Eqs (4) and (5) show the intrinsic and extrinsic reactions for the formation of oxygen vacancies, respectively.

More generally, the electroneutrality relation is given by

$$2[V_O^{\cdot\cdot}] = n + [Gd'_{Ce}] \tag{6}$$

where $[Gd'_{Ce}]$ is the concentration of acceptor dopant.

E. D. Wachsman—contributing editor

Manuscript 187787. Received April 6, 2001; approved March 4, 2002.

This work was supported by the Department of Energy under Contract No. DE-AC26-99FT40710 and by Unitika Ltd.

*Member, American Ceramic Society.

†Current address: Structural Ceramic Group, Metal and Ceramics Division, Oak Ridge National Laboratory, Oak Ridge, Tennessee 37831-6068.

The oxygen stoichiometry is determined by Eqs. (4) and (5) and the temperature dependence of the equilibrium constant for Eq. (4) is given by

$$K_R(T) = K_R^0 \exp(-\Delta H/kT) = [V_O^{\cdot\cdot}]n^2 P_{O_2}^{1/2} \tag{7}$$

where ΔH is the enthalpy for oxygen vacancy formation.

Combining Eqs. (6) and (7), the equilibrium constant can be written as

$$K_R(T) = \tfrac{1}{2}n^2(n + [Gd'_{Ce}])P_{O_2}^{1/2} \tag{8}$$

For simplification, the parameter

$$\tilde{n} = \frac{n}{[Gd'_{Ce}]} \tag{9}$$

is introduced and Eq. (8) is rewritten to yield

$$\tilde{n}^2(\tilde{n} + 1)P_{O_2}^{1/2} = 2P_t^{1/2} \tag{10}$$

where

$$P_t = \left(\frac{K_R(T)}{[Gd'_{Ce}]^3}\right)^2 \tag{11}$$

is the transition pressure, which is defined as the oxygen partial pressure where $n = [Gd'_{Ce}]$ or $\tilde{n} = 1$.

From the relation in Eq. (6), the ionic conductivity in Eq. (2) becomes

$$\sigma_i = \frac{\sigma_e}{\beta} + \sigma_{i0} \tag{12}$$

where β and σ_{i0} are the ratio of electron and oxygen vacancy mobility and the ionic conductivity in the higher P_{O_2} region which does not change with P_{O_2} respectively, which are given by

$$\beta = \frac{\mu_e}{\mu_{V_O^{\cdot\cdot}}} \tag{13}$$

$$\sigma_{i0} = e[Gd'_{Ce}]\mu_{V_O^{\cdot\cdot}} \tag{14}$$

Using Eqs. (1), (2), (3), (6), and (14), the normalized electron concentration $\tilde{n}$ can be written as

$$\tilde{n} = \frac{\sigma_t - \sigma_{i0}}{(\beta + 1)\sigma_{i0}} \tag{15}$$

Substituting Eq. (15) into Eq. (10) results in the expression between oxygen partial pressure and total conductivity,

$$P_{O_2} = \frac{4P_t}{\left(\frac{\sigma_t - \sigma_{i0}}{\sigma_{i0}(\beta + 1)}\right)^4 \left(\frac{\sigma_t - \sigma_{i0}}{\sigma_{i0}(\beta + 1)} + 1\right)^2} \tag{16}$$

which was used for fitting the data.

Note that the expression in Eq. (16) includes both of the intrinsic and extrinsic effects that are shown in Eqs. (4) and (5). When the extrinsic reaction is dominant, which can be discribed as $\tilde{n} \ll 1$, $\tilde{n}$ or the electronic conductivity σ_e is proportional to $P_{O_2}^{-1/4}$. On the other hand, when the intrinsic reaction is dominant, where $\tilde{n} \gg 1$, $\tilde{n}$ or the electronic conductivity σ_e is proportional to $P_{O_2}^{-1/6}$. Since $P_{O_2} = P_t$ at $\tilde{n} = 1$, P_t stands for the oxygen partial pressure where the transition from $P_{O_2}^{-1/4}$ to $P_{O_2}^{-1/6}$ dependence of the electronic conductivity takes place as $\tilde{n}$ increases. The fitting parameters P_t and β were useful to determine the other values. From Eqs. (7) and (11), P_t becomes

$$P_t(T) = \left(\frac{(K_R^0)^2}{[Gd'_{Ce}]^6}\right) \exp\left(-\frac{2\Delta H}{kT}\right) \tag{17}$$

so that ΔH can be determined from the temperature dependence of P_t. Using Eqs. (2), (3), and (13), β becomes

$$\beta(T) = C_0 \exp\left(\frac{E_i - E_h}{kT}\right) \tag{18}$$

where $C_0 = \mu_{e0}/\mu_{i0}$ is a temperature-independent constant. Assuming that ionic conductivity can be given by Eq. (14), E_i can be estimated from temperature dependence measurements and combining with Eq. (18), E_h is also determined. Note that $E_i - E_h$ is usually a positive value.

The transference number, t_i is defined as

$$t_i = \frac{\sigma_i}{\sigma_t} = 1 - \frac{\sigma_e}{\sigma_t} \tag{19}$$

which can be described using β and P_t. Using Eqs. (14), (13), and (19), $\tilde{n}$ in Eq. (9) becomes

$$\tilde{n} = \frac{\sigma_e}{\beta\sigma_{i0}} = \frac{\sigma_t(1 - t_i)}{\beta\sigma_{i0}} \tag{20}$$

Combining Eqs. (1), (12), and (19), the following relation can be derived:

$$\left\{1 - \left(1 + \frac{1}{\beta}\right)(1 - t_i)\right\}\sigma_t = \sigma_{i0} \tag{21}$$

and Eq. (20) becomes

$$\tilde{n} = \frac{1 - t_i}{\beta t_i + t_i - 1} \tag{22}$$

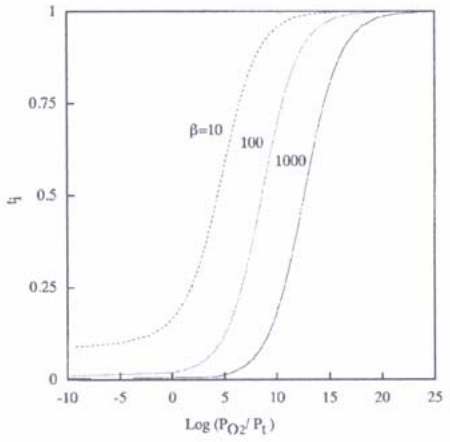

Fig. 1. P_{O_2} dependence of the transference number t_i as a function of β.

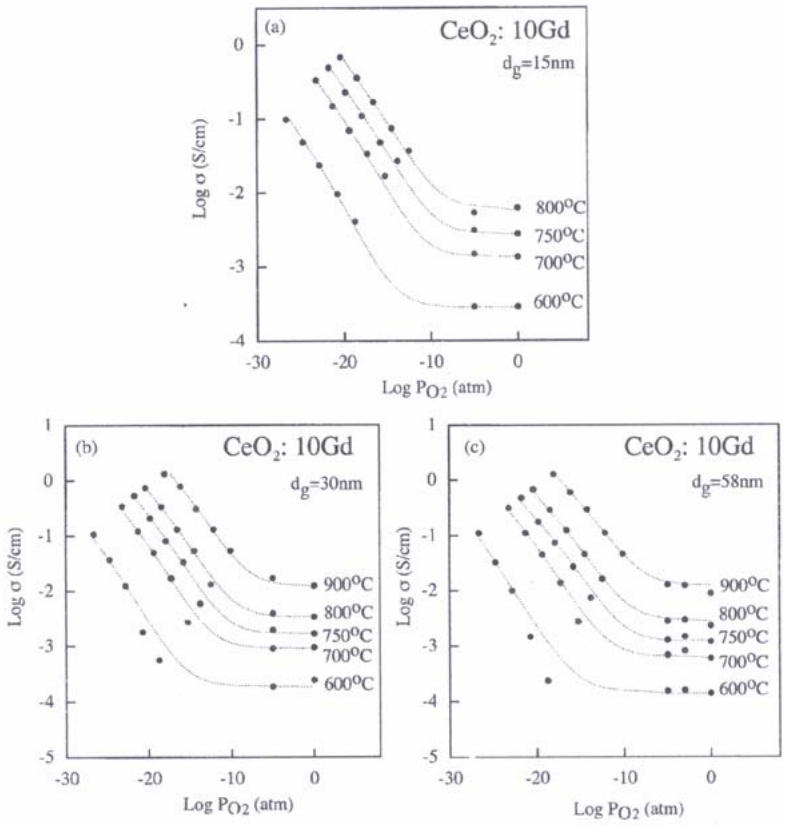

Fig. 2. Electrical conductivity of CeO_2:10Gd thin films as a function of oxygen partial pressure and temperature: (a) d_g = 15, (b) 30, (c) 58 nm. Film thickness = 300–400 nm.

Equation (10) can be described as following in the form of Eq. (16)

$$P_{O_2} = \frac{4P_t(\beta t_i + t_i - 1)^6}{(1 - t_i)^4 \beta^2 t_i^2} \tag{23}$$

This is a form that describes the relation between t_i and P_{O_2} in terms of β and P_t. The range of t_i is limited

$$\frac{1}{1 + \beta} < t_i < 1 \tag{24}$$

in this model, which is derived from the fact that the denominator of Eq. (22) must be greater than 0. As P_{O_2} decreases, t_i also decreases, and when it reaches $1/(1 + \beta)$, t_i becomes P_{O_2} independent and $t_i = 1/(1 + \beta)$.

Figure 1 shows the P_{O_2} dependence of t_i as a function of β calculated from Eq. (23). As can be seen, t_i at fixed P_{O_2} increases with decreasing β and P_t. According to Eqs. (17) and (18), P_t decreases and β increases with decreasing temperature. Therefore, at fixed P_{O_2} t_i does not always increase at decreasing temperature, especially at lower P_{O_2} where the electronic conductivity is dominant.

III. Experimental Procedure

Gd-doped CeO_2 thin films were prepared by a polymer precursor spin coating process using cerium nitrate, $Ce(NO_3)_3 \cdot 6H_2O$ and gadolinium nitrate $Gd(NO_3)_3 \cdot 6H_2O$ for doped specimens.[6] The procedure of this method is as follows: The appropriate concentrations of cations were added to ethylene glycol. After complete dissolution, the transparent solution was heated to about 80°C and stirred for up to 72 h until it turned to a gelatinous polymeric liquid. By controlling the solution viscosity, the spin rate, and the annealing temperature, oxide films with variable thickness and microstructure can be prepared on dense substrates.

For this study, 15–20 depositions of a precursor [2 wt% Ce + Gd (10, 20 mol% of Ce) solution] with a spin speed of 3000 rpm were performed on sapphire substrates. The annealing temperature varied in the range of 600–1200°C for 4 h annealing time in air. The final thickness of the films was about 300–400 nm. The grain sizes of thin films were determined from X-ray diffraction measurements[7] and correlated with the annealing temperatures. The grain size can be controlled by the annealing temperature, and the grain size in these annealing temperatures ranged from 7 to 58 nm

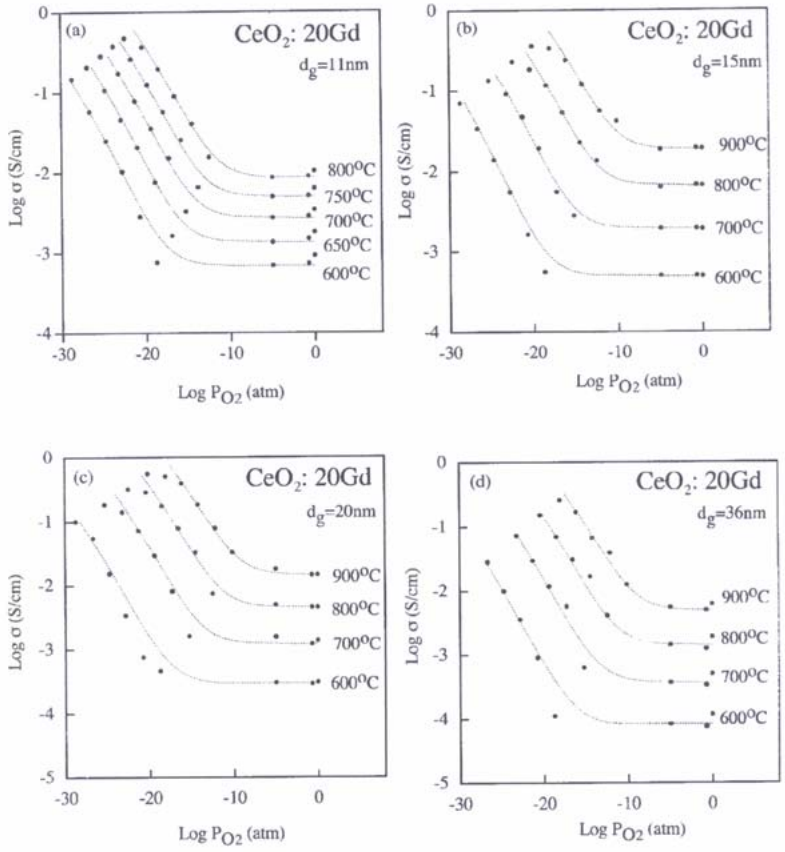

Fig. 3. Electrical conductivity of CeO_2:20Gd thin films as a function of oxygen partial pressure and temperature: (a) d_g = 11, (b) 15, (c) 20, (d) 36 nm. Film thickness = 300–400 nm.

for CeO_2:10Gd thin films and from 9 to 36 nm for CeO_2:20Gd.[8] There is the possibility of reaction between Gd and sapphire substrate at higher temperature; however, no second phases were observed in X-ray measurements up to 1200°C. Details are discussed elsewhere.[8]

The electrical conductivity of films was studied by impedance spectroscopy using a Solartron 1260 frequency response analyzer with a 1296 Interface. The impedance spectra were obtained using a two-probe method over the frequency range 1 Hz to 5 MHz. The typical size of samples was 5 mm for length and 5 mm × 400 nm for cross-section area. Silver paste was applied as electrodes for these measurements. An electrode contact was made with the cross section of the film, thereby allowing measurements to be made in the plane of the film. Conductivity, σ, was calculated using the following relation:

$$\sigma = \frac{L}{AR} \tag{25}$$

where L and A are the length and the cross-section area of samples. R is the resistance of samples determined from impedance spectra. Measurements were conducted in oxygen, air, helium, and CO/CO_2 mixtures for the oxygen partial pressure range of 10^{-26}–1 atm over the temperature range of 600–900°C.

IV. Electrical Conductivity of Gd-Doped CeO_2 Thin Films

The impedance spectra for nanocrystalline thin films showed only one semicircle;[8] therefore, only total conductivity of nanocrystalline thin films has been determined from impedance spectroscopy.

Figures 2 and 3 show the electrical conductivity of CeO_2:10Gd and 20Gd thin films as a function of P_{O_2} and temperature. As can be seen at high P_{O_2}, the electrical conductivity of both CeO_2:10Gd and 20Gd samples is independent of P_{O_2} and follows a $P_{O_2}^{-1/4}$ behavior at low P_{O_2} for all different microstructures. This behavior is considered to be related to dopants which behave as acceptors. For 15 nm grain size specimens, the conductivity of CeO_2:20Gd is almost 2 times higher than that of CeO_2:10Gd specimens in the high-P_{O_2} region.

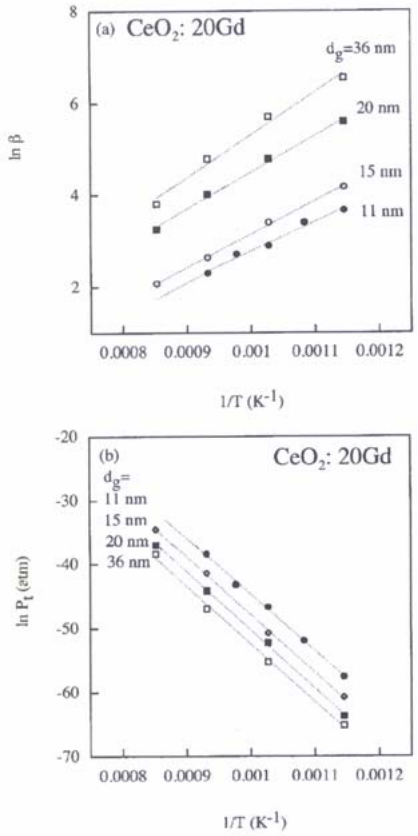

Fig. 4. Grain size dependence of (a) β and (b) P_t, determined for CeO_2:20Gd.

Dash lines in Figs. 2 and 3 show the fit of Eq. (16) using β and P_t as fitting parameters. From Eqs. (17) and (18), analysis of the temperature dependence of β and P_t gives information about ΔH and $E_i - E_h$. Figure 4 shows the temperature dependence of β and P_t as a function of grain size for CeO_2:20Gd specimens. As the grain size decreases, β decreases, which means that the ionic mobility becomes enhanced. P_t increases with decreasing grain size and with little change in the activation energy. This means intrinsic behavior in conductivity appears at higher P_{O_2}, which is consistent with

Table I. Temperature-Dependent Parameters of Nanocrystalline CeO_2:10Gd Thin Films

Grain size (nm)	E_i (eV)	E_h (eV)	ΔH (eV)
15	1.28	0.59	3.58
30	1.34	0.57	4.03
58	1.36	0.57	3.94
Error	±0.04	±0.04	±0.08

Table II. Temperature-Dependent Parameters of Nanocrystalline CeO_2:20Gd Thin Films

Grain size (nm)	E_i (eV)	E_h (eV)	ΔH (eV)
11	1.13	0.58	3.80
15	1.19	0.57	3.89
20	1.25	0.56	3.93
36	1.33	0.53	3.89
Error	±0.04	±0.04	±0.08

the previous results of conductivity measurement for undoped nanocrystalline CeO_2.[4] The results determined from Fig. 4 are shown in Tables I and II for CeO_2:10Gd and CeO_2:20Gd. Within experimental error, the hopping energy is constant with grain size and is close to the reported value of the hopping energy, 0.52[9] and 0.49 eV.[10] The enthalpy of oxygen vacancy formation ΔH is also shown in Fig. 5 as a function of grain size. As can be seen, ΔH found for the Gd-doped CeO_2 samples was almost 10% lower than that observed for undoped CeO_2 in the larger grain size region and changed only slightly as grain size decreased. The main effect of dopant content shows up as a shift of the point, where ΔH started decreasing, to lower grain size. This behavior of ΔH for doped specimens may be related to dopant segregation in the grain boundary region, which could lead to less dopant effects for smaller grain size specimens; however, this is still under investigation.

Using the values of β and P_t, the transference number t_i was calculated from Eq. (23). Figure 6(a) shows the P_{O_2} dependence of t_i with different grain size (T = 600°C) and d_g = 15 nm sample shows higher t_i at fixed P_{O_2}. As discussed before, t_i at fixed P_{O_2} increases as β and P_t decrease; however, with decreasing grain size, β decreased and P_t increased as shown in Fig. 4. Therefore, t_i does not change monotonously with grain size change, which suggests that the d_g = 15 nm sample has the more optimal values of β and P_t to obtain higher t_i.

Figure 6(b) shows the P_{O_2} dependence of t_i as a function of temperature (d_g = 15 nm). This predicts that in the higher P_{O_2} region, t_i increases as the temperature decreases, however, decreases in the lower P_{O_2} region. The behavior in the lower P_{O_2} region ($<10^{-25}$) can be explained by decreases of β, electronic

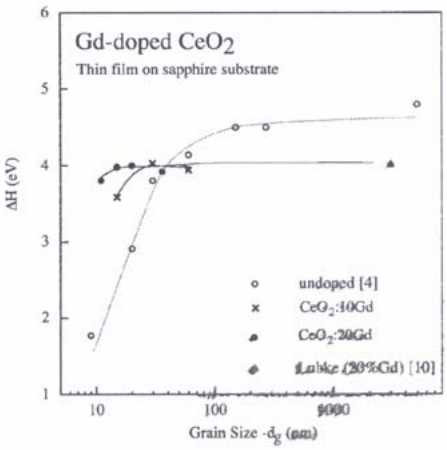

Fig. 5. Enthalpy of oxygen vacancy formation of Gd-doped CeO_2 thin films.

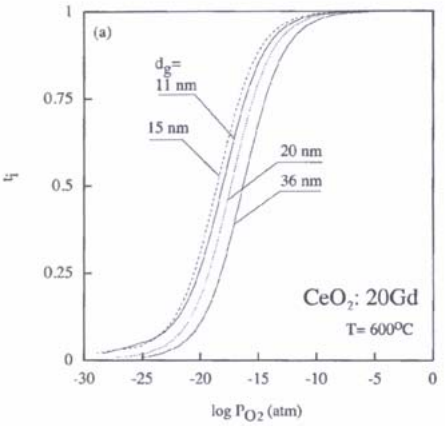

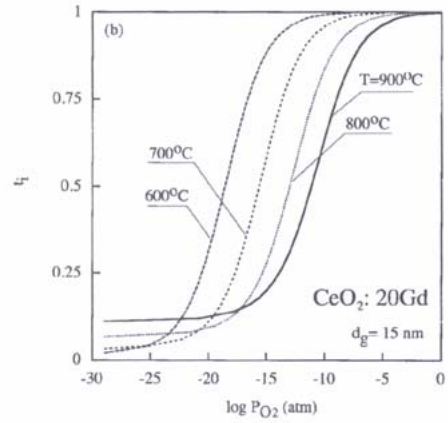

Fig. 6. Calculated P_{O_2} dependence of t_i (a) with different grain sizes (T = 600°C) and (b) with different temperatures (d_g = 15 nm).

ionic mobility ratio, as temperature increases, which leads to an increase of t_i.

Figure 7 shows the temperature dependence of the ionic conductivity of CeO_2:20Gd thin films determined for different grain size specimens at P_{O_2} = 1 atm. In this figure, for comparison the ionic conductivity of microcrystalline CeO_2:20Gd is included.[10] It is shown that nanocrystalline samples have E_i = 1.0–1.3 eV, which is close to the reported value for the grain boundary conductivity.[10,11] The ionic conductivity for nanocrystalline samples was lower than that for microcrystalline specimens. This could be explained by the fact that the grain boundary resistivity is orders of magnitude larger than that of the grain interiors in microcrystalline specimens,[12] and therefore reduced conductivity could be observed in nanocrystalline ones since grain boundary volume is enhanced in the nanocrystalline region. It appears, however, that the ionic conductivity of nanocrystalline Gd-doped CeO_2 increased with decreasing activation energy as the grain size decreased. This behavior seems to be due to the segregation of impurities in the lower grain sizes[13] and an increase in the mobility

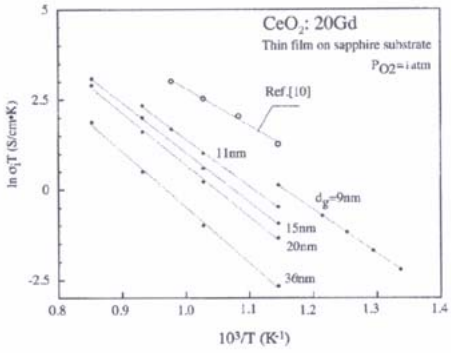

Fig. 7. Temperature dependence of the ionic conductivity determined for CeO_2:20Gd with different grain size specimens. Data from Ref. [10] show the bulk conductivity of CeO_2:20Gd.

of oxygen vacancies. This is also supported by the results from Gerhardt and Nowick, who reported that the Si-free (less than 10 ppm) Gd-doped CeO_2 sample showed lower activation energy than that with about 1000 ppm Si.[11]

V. Summary

The results of a study related to the formation and the microstructure of Gd-doped CeO_2 thin films obtained by the polymeric precursor spin coating technique have been presented. The microstructure can be altered by the presence of Gd with the grain size decreasing as the Gd concentration increased. The electrical properties of these films of varying grain size have been investigated as a function of temperature and oxygen partial pressure. These results were also analyzed using an electrical conductivity model. It was also shown that not only P_{O_2}-dependent conductivity but also the transference number can be described using the parameters β and P_i. The enthalpy of oxygen vacancy formation, ΔH, and the hopping energy were determined using these parameters. ΔH for Gd-doped CeO_2 showed less dependence on grain size compared to undoped CeO_2. This could be related to the dopant segregation at the grain boundary; however, the effects of Gd on ΔH are still unknown. The ionic conductivity of nanocrystalline Gd-doped CeO_2 increases as the grain size decreases, while the activation energy of conductivity decreases, but even at the smallest grain size, 9 nm, the ionic conductivity was about 4 times lower than that for microcrystalline specimens. The activation energy of the ionic conductivity tends to decrease with the grain size. This is probably related to increased segregation of impurities in the grain boundary region when the grain size decreased.

References

[1]B. C. H. Steele, "Appraisal of $Ce_{1-y}Gd_yO_{2-y/2}$ Electrolytes for IT-SOFC Operation at 500°C," *Solid State Ionics*, **129**, 95–110 (2000).

[2]M. Mogensen, N. M. Sammes, and G. A. Tompsett, "Physical, Chemical and Electrochemical Properties of Pure and Doped Ceria," *Solid State Ionics*, **129**, 63–94 (2000).

[3]I. Kosacki, B. Gorman, and H. U. Anderson, "Microstructure and Electrical Conductivity in Nanocrystalline Oxide Thin Films," *Electrochem. Soc., Proc.*, **97** [24] 631 (1998).

[4]T. Suzuki, I. Kosacki, H. U. Anderson, and P. Colomban, "Electrical Conductivity and Lattice Defects in Nanocrystalline CeO_2 Thin Films," *J. Am. Ceram. Soc.*, **84** [9] 2007–14 (2001).

[5]M. Barsoum, *Fundamentals of Ceramics*. McGraw-Hill, New York, 1997.

[6]H. U. Anderson, M. M. Nasrallah, and C. C. Chen, "Method of Coating a Substrate with a Metal Oxide Film from an Aqueous Solution Comprising a Metal Cation and a Polymerizable Organic Solvent," U.S. Pat. No. 5 494 700, 1996.

[7]B. D. Cullity, *Elements of X-ray Diffraction*. Addison-Wesley, Reading, MA, 1959.
[8]T. Suzuki, I. Kosacki, and H. U. Anderson, "Microstructure/Electrical Conductivity Relationships in Nanocrystalline Ceria Thin Films"; in Proceedings of the International Symposium on Soft Solution-Processing (Tokyo, Japan), in press.
[9]S. Wang, T. Kobayashi, M. Dokiya, and T. Hashimoto, "Electrical and Ionic Conductivity of Gd-Doped Ceria," *Electrochem. Soc., Proc.*, **99** [9] 193–200 (1999).
[10]S. Lubke and H. D. Wiemhofer, "Electronic Conductivity of Gd-Doped Ceria with Additional Pr-Doping," *Solid State Ionics*, **117**, 229–43 (1999).
[11]R. Gerhardt and A. S. Nowick, "Grain-Boundary Effect in Ceria Doped with Trivalent Cations: I, Electrical Measurements," *J. Am. Ceram. Soc.*, **69** [9] 641–46 (1986).
[12]J.-H. Hwang, D. S. Mclachlan, and T. O. Mason, "Brick Layer Model Analysis of Nanoscale-to-Microscale Cerium Dioxide," *J. Electroceram.*, **3** [1] 7–16 (1999).
[13]M. Aoki, Y.-M. Chiang, I. Kosacki, L. Jong-Ren Lee, H. L. Tuller, and Y. Liu, "Solute Segregation and Grain-Boundary Impedance in High-Purity Stabilized Zirconia," *J. Am. Ceram. Soc.*, **79** [5] 1169–80 (1996). □

Appendix C

Optical Properties of Undoped and Gd-doped CeO_2 Nanocrystalline Thin Films
T. Suzuki, I. Kosacki, V. Petrovsky, and H.U. Anderson
J. of Applied Physics, Volume 91, Number 4, 2308-2314, February 2002

Optical properties of undoped and Gd-doped CeO_2 nanocrystalline thin films

Toshio Suzuki,[a] Igor Kosacki, Vladimir Petrovsky, and Harlan U. Anderson
Electronic Materials Applied Research Center, University of Missouri-Rolla, Rolla, Missouri 65401

(Received 6 April 2001; accepted for publication 6 November 2001)

The results of studies of the preparation, structure, and optical properties of undoped and Gd-doped CeO_2 thin films are presented. Dense films with 4–150 nm grain size have been obtained on monocrystalline sapphire substrates using a polymeric precursor spin coating method. The results of the optical measurements are presented and correlated with the microstructure of the films. The transmission spectra have been used to determine the energy dependence of the refractive index, n and the extinction coefficient, k. Both n and k of the thin films decreased as grain size decreased and these results showed that this change could be related to the transition from crystalline to amorphous CeO_2. The effect of dopant has little influence on n, $<5\%$, but doping resulted in about a 30%–40% reduction of k compared to undoped specimens, which could be related to the decrease of absorption centers due to the replacement of Ce by Gd. © *2002 American Institute of Physics.*
[DOI: 10.1063/1.1430890]

I. INTRODUCTION

Cerium based oxides have been of interest because of their relatively high electrical conductivity, chemical stability, efficiency for absorbing UV radiation, and transmission in the visible and infrared regions. Many studies have been made of the optical properties of CeO_2 thin films by using optical transmission or reflectance spectroscopy.[1–3] Guo *et al.* investigated the optical and structural properties of cerium oxide thin films obtained by rf magnetron sputtering.[1] They investigated optical properties of highly oriented crystalline and amorphous CeO_2 thin films using variable angle spectroscopic ellipsometry (VASE) and reported that highly oriented crystalline specimens exhibited a higher refractive index and a higher band gap energy for both direct and indirect transition compared to amorphous specimens. Therefore, investigation of optical properties for nanocrystalline ceria with different grain size becomes more important to understand the optical behavior of crystalline and amorphous specimens.

Nanocrystalline materials have studied not only optical but also electrical properties since they have shown their enhanced characters which are not seen in microstrusture materials. One of the interesting phenomena regarding nanostructure is the quantum confinement effect.[4,5] This effect, which is well investigated for semiconductors, occurs when the crystal size approaches the spatial extent of an electron and/or hole, and results in shifts of the absorption edge to higher energy, in other words, increase of band gap energy. This behavior also observed for nanocrystalline ZrO_2:16%Y and CeO_2 thin films.[6,7] Recent studies have shown that nanocrystalline ceria have the electrical properties that differ from those observed for microcrystalline oxides, because of the increased surface area and grain boundary volume.[8–11] The electronic conductivity of nanocrystalline ceria is enhanced compared with microcrystalline ones

Thin film processing methods such as deposition methods and sol-gel technique have been utilized to synthesize nanocrystalline materials. Comparing consolidation and sintering of clusters, these methods are the low temperature of the methods, which can be a significant advantage. Among these methods, recent studies have shown that a polymer precursor spin coating technique,[12] which is the low temperature nanocrystalline thin film synthesis method, has turned out to be effective for a very stable precursor, low processing temperature $\geqslant 400\,^{\circ}C$ and yielding very dense and optical quality films. These features are enabled to control the grain size and to obtain stable microstructure, which is very important and makes it possible for the systematic study of microstructure-physical properties relationships, including optical and electrical properties. Application of nanocrystalline oxides is very wide and includes the electrochemical devices such as solid oxide fuel cell, ceramic oxygen generator, and partial oxidation membranes.

The purpose of this study was to investigate the influence of grain size on the optical absorption spectra and to relate the optical absorption properties of nanocrystalline and amorphous structures. In the present work, the results of transmission measurements and analysis of spectra to determine the refractive index and the extinction coefficient are presented and the influence of dopant and microstructure to the optical absorption properties including the band gap energy.

II. EXPERIMENT

A. Sample preparation

Nanocrystalline undoped and 20%Gd-doped CeO_2 thin films with a thickness of 0.3–0.4 μm have been obtained on sapphire single crystal substrates using a polymeric precursor spin coating process.[12] For this preparation, cerium nitrate,

[a]Electronic mail: toshio@umr.edu.

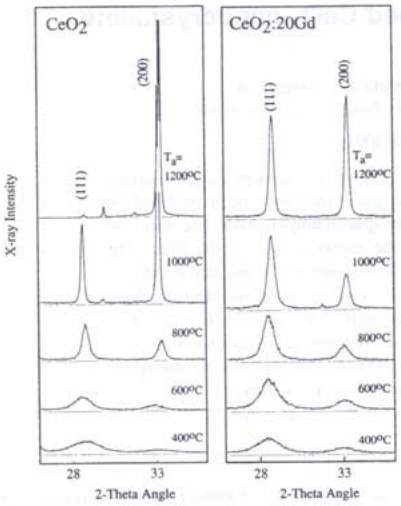

FIG. 1. X-ray diffraction patterns of undoped and Gd-doped CeO_2 thin films deposited on monocrystalline sapphire substrate annealed under different temperatures. Thickness of films ranged from 300 to 400 nm.

$Ce(NO_3)_3 \cdot 6H_2O$ and gadolinium nitrate, $Gd(NO_3)_3 \cdot 6H_2O$ for doped specimens were used as starting material. The appropriate concentrations of the cations were added to a solution containing water and ethylene glycol. A conventional spin coating technique was used to deposit the precursor on the substrate. By controlling the solution viscosity, the spin rate and annealing temperature, undoped and 20%Gd-doped CeO_2 films with variable thickness and microstructure were

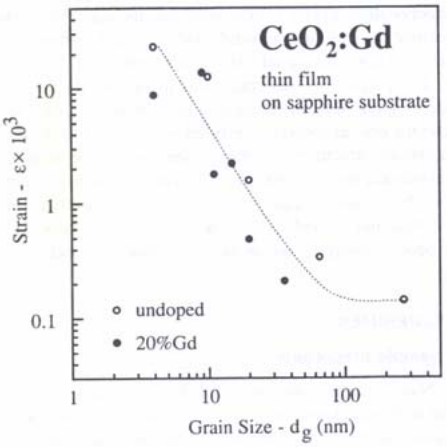

FIG. 2. Relationship between strain and grain size for undoped and Gd-doped CeO_2 thin films deposited on monocrystalline sapphire substrate. Film thickness = 300–400 nm.

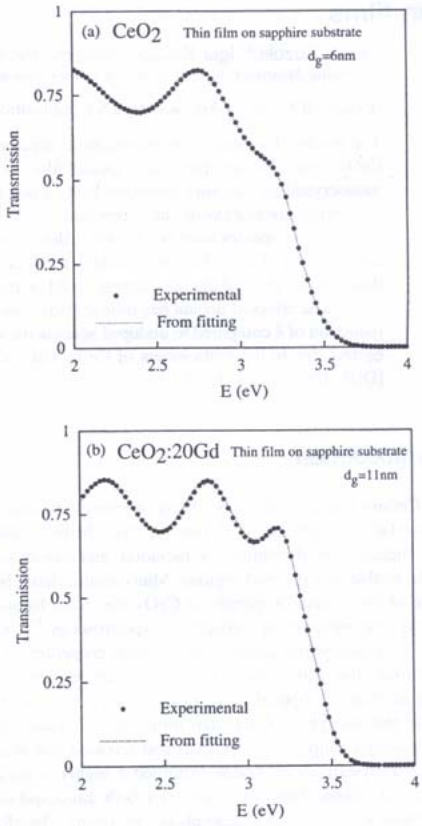

FIG. 3. Transmission spectra of (a) undoped and (b) Gd-doped CeO_2 thin films. The dash line was obtained by the curve fitting. Film thickness =300–400 nm.

prepared on the substrates. The undoped and 20%Gd-doped CeO_2 films were obtained by annealing the films for 4 hours over the temperature region of 350–1200 °C. These temperatures are low compared to those typically required by powder processing techniques (1400–1800 °C), but do allow the formation of dense, more than 90% of theoretical density, nanocrystalline specimens.

B. XRD characterization

The crystallization and grain growth of undoped and 20%Gd-doped CeO_2 films in the cubic phase were investigated using x-ray diffraction (XRD). X-ray diffraction data for thin film samples were collected using a SINTAG 2000 x-ray diffractometer operating with $Cu K\alpha 1$ radiation. A typical 2θ scan range of 20°–80° and a step size of 0.05°

were employed. The XRD spectra have been recorded in the offset configuration to reduce the signal from monocrystalline substrate [orientation (012)].

The analysis of the shape of each x-ray line has been used to determine the grain size for all specimens. Assuming that the line broadening ($\beta=\beta'+\beta''$) is the sum of the contributions attributed to the grain size(d_g) and the strain (ε), which can be written as $\beta'=1/(d_g\cos\theta)$ and $\beta''=4\varepsilon\tan\theta$, then the grain size and the strain can be determined from the linear relationship between $\beta\cos\theta$ and $4\sin\theta$, where θ is the Bragg diffraction angle. Note that the strain (ε) is defined as $\varepsilon=\Delta d/d$, where Δd is displacement of the lattice.[13]

C. Optical measurement

Undoped and 20%Gd-doped CeO_2 thin films were studied by optical transmission spectroscopy to determine the relationship between the optical related properties and the microstructure. The transmission spectra were obtained at room temperature with a Cary UV-visible spectrophotometer. Intensity of the transmission spectra can be described by the thickness of the film, the refractive index and extinction coefficient of thin film and substrate using Fresnel's equations.[14] The transmission spectra were fitted using these relations to determine the refractive index and extinction coefficient for different specimens.

III. RESULTS AND DISCUSSION

A. Microstructure of undoped and 20%Gd-doped CeO_2 thin films

Figure 1 shows the XRD spectra for the (111) and (200) diffraction lines for undoped and 20%Gd-doped CeO_2 specimens annealed at different temperatures.[15,16] Note that these are the parts of the spectra that are measured. The spectra show that the same crystal structures were obtained for both undoped and Gd-doped specimens, however the crystal growth in the (200) direction appears to be faster for the undoped specimens. It was observed that the grain size was as a function of the annealing temperature and the dopant level.[16] The doped films appeared to be about 20 nm after annealing at 1000 °C for 4 h, while that for the undoped was about 65 nm, which shows that the grain size of Gd-doped CeO_2 was substantially reduced compared to that of undoped specimens.[16]

Compared to the ionic radii of Ce^{4+} and Gd^{3+}, 1.11 and 1.19 Å (coordination number=8),[17] it can be predicted that Gd ions are most likely placed in Ce positions in the lattice. This can be confirmed by the x-ray diffraction lines, with the result that the peak positions for undoped and doped specimens do not change as shown in Fig. 1.

A strain versus grain size plot for undoped and Gd-doped CeO_2 thin films is shown in Fig. 2 which were determined from x-ray analysis. It is shown that smaller grain size specimens display higher strain for both undoped and doped specimens and no dopant effect on grain size–strain relation.

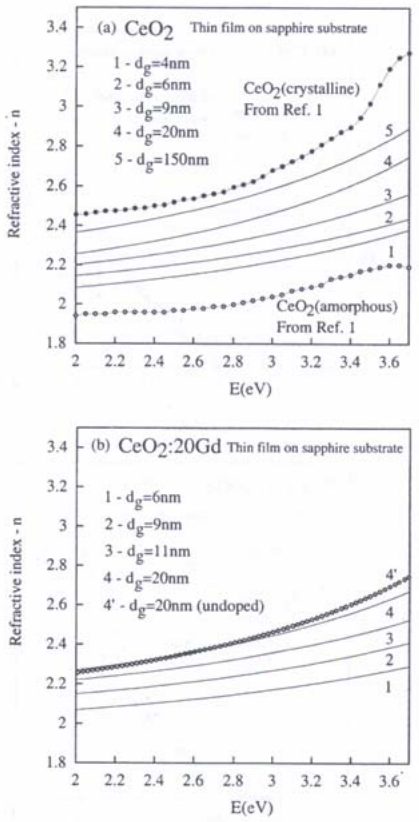

FIG. 4. The photon energy dependence refractive index of (a) undoped and (b) Gd-doped CeO_2 thin films with the reported values of crystalline and amorphous CeO_2. Film thickness = 300–400 nm.

B. Optical properties of undoped and 20%Gd-doped CeO_2 thin films

1. The refractive index and extinction coefficient of undoped and Gd-doped CeO_2 thin films

Figure 3 shows the transmission spectra of (a) undoped and (b) Gd-doped CeO_2 films with the line being calculated by a fitting procedure, where the refractive index and the extinction coefficient were determined. The results show that the experimental data were well reproduced by the calculated line. The thickness of films was obtained from this calculation and was found to range from 300 to 400 nm.

The energy dependence of the refractive index for undoped and 20%Gd-doped CeO_2 thin films is shown in Figs. 4(a) and 4(b) with the value of crystalline and amorphous CeO_2.[1] The refractive indices which were observed to decrease as the grain size decreased for both undoped and Gd-doped specimens appears to be due to density and/or the influence of the grain boundaries, since the refractive indices lie between those of crystalline and amorphous CeO_2. As

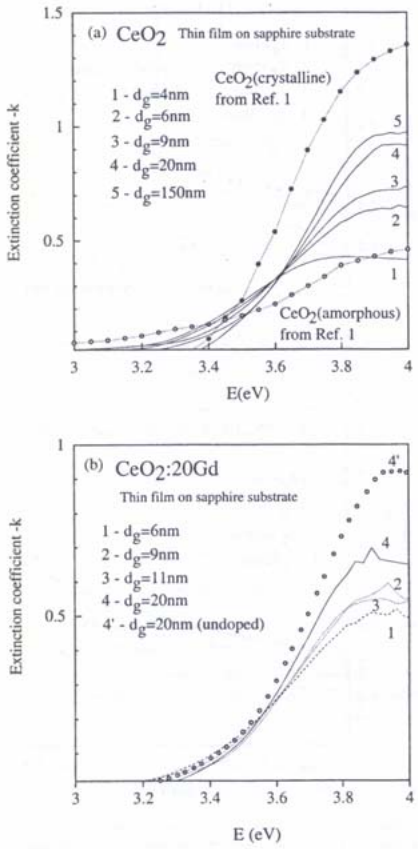

FIG. 5. Photon energy dependence extinction coefficient of (a) undoped and (b) 20%Gd-doped CeO_2 thin films with reported values. Film thickness = 300–400 nm.

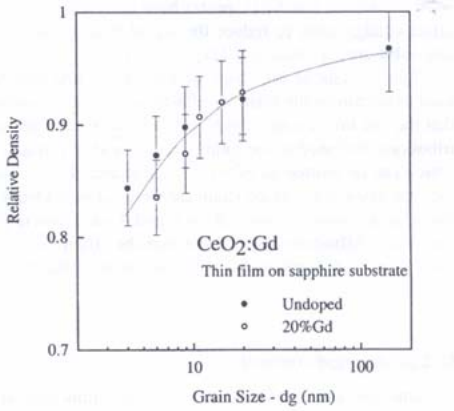

FIG. 6. Relative density for undoped and 20%Gd-doped CeO_2 thin films determined from the refractive index. Film thickness = 300–400 nm.

shown in Fig. 4(b), the refractive index of both undoped and doped CeO_2 were same (within 5%), which shows almost no effect of the dopant on n. This is to be expected since the crystal structure and density at the undoped and doped specimens did not change with dopant additions. Similar results have also reported for Sn doped-CeO_2 (Ref. 11) and Y doped ZrO_2.[18]

The extinction coefficients as a function of photon energy for the undoped and Gd-doped CeO_2 films are shown in Figs. 5(a) and 5(b). For undoped specimens, it is shown that the shape of the k curve changes and decreases as grain size decreases to be close to the value seen for amorphous CeO_2.[1] For doped specimens, on the other hands, the value of k is decreased about 30%–40% compared to those of undoped specimens. These results could be explained by the assumption that the introduction of Gd results in a decrease in the concentration of the absorption center (Ce–O–Ce) with dopant additions.

The relation between refractive index and the relative density of the specimens is given by,[19,20]

$$\frac{n_E^2-1}{n_E^2+2}=\frac{n^2-1}{n^2+2}\rho, \tag{1}$$

where n_E, n, and ρ are the effective refractive index, the refractive index of 100% dense material and the relative density of specimen, respectively. Taking n as the value of crystalline CeO_2 from literature[1] and n_E as the value of nanocrystalline specimens, the density of thin films can be obtained from Eq. (1) and shown in Fig. 6 as a function of grain size. The results showed the density of 87%±3.5%(undoped) and 84%±3.4%(Gd doped) for 6 nm grain size specimens. The relative density of the grain boundary region is reported to be about 60% of the crystalline[21] and assuming that the thickness of grain boundary is 1 nm, a 6 nm grain size specimen has about 27% of its volume as grain boundary. Therefore, the estimated density of 6 nm grain size specimen is about 89%, which is close to the value determined from optical measurements.

An attempt was made to treat the grain boundaries as being amorphous and to fit the k of the nanocrystalline specimens using the data for crystalline and amorphous specimens. This was, however, not successful which indicated that the grain boundary region could not be considered amorphous from the optical point of view.

2. Absorption coefficient and the band gap energy

The absorption coefficient, α can be calculated from the relation using k:[14]

$$\alpha=\frac{4\pi k}{\lambda}, \tag{2}$$

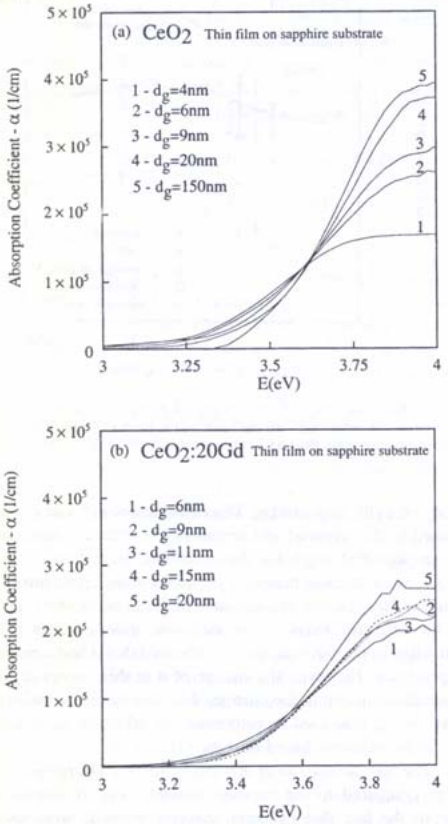

FIG. 7. Absorption coefficient, α as a function of photon energy for (a) undoped (b) 20%Gd-doped CeO_2 thin films with different grain size.

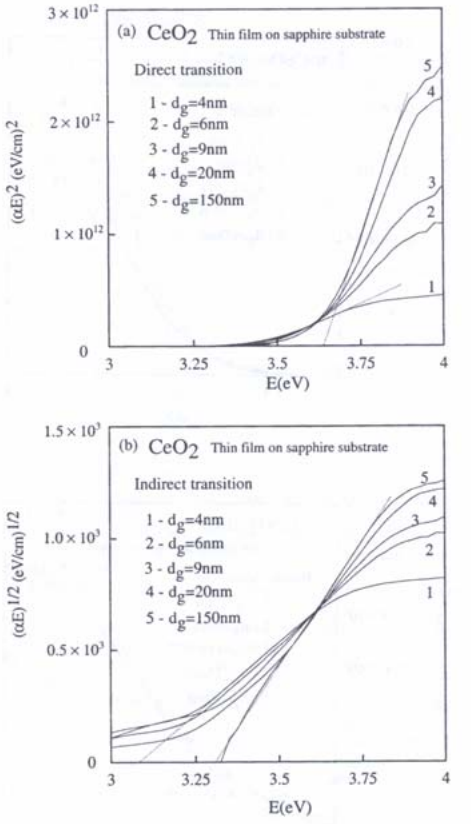

FIG. 8. Behavior of (a) $(\alpha E)^2$, (b) $(\alpha E)^{1/2}$ as a function of photon energy for CeO_2 thin films with different grain size.

where λ is the wavelength of incident light. The absorption coefficient of undoped and Gd-doped CeO_2 are shown in Fig. 7. The optical band gap energy, E_g was determined from the analysis of the absorption spectra, where a steep increase of the absorption is observed due to a band–band transition, from the general relation[1,3]

$$\alpha E = b(E - E_g)^{\eta}, \tag{3}$$

where E is the photon energy, and η is a constant with the value 1/2 for direct allowed transitions, and 2 for indirect allowed transitions. Figure 8 shows (a) direct and (b) indirect absorption of undoped specimens as a function of phonon energy. For both the direct and indirect transitions, E_g decreases as grain size decreases, where E_g is between the values reported for crystalline and amorphous specimens. The changes in band gap energy with a decreasing grain size are often correlated to quantum confinement which has been experimentally well established for semiconducting materials and theoretically understood.[4,5] For undoped CeO_2, we have reported that confinement effects occurred with grain size below 200 nm,[7] but E_g decreased for the grain size <50 nm. Similar results are also seen for direct and indirect absorption of Gd-doped specimens with grain size lower than 20 nm as shown in Figs. 9(a) and 9(b). Figure 10 shows the behavior of the band gap energy as a function of the grain size for undoped and 20%Gd-doped CeO_2 thin films determined from optical absorption spectra. As can be seen, the effect of dopant on the optical band gap energy is very small. The band gap energy determined for undoped 150 nm grain size was found to be 3.32 ± 0.10 eV for indirect transition, and 3.64 ± 0.11 eV for direct transition, which is consistent with previously reported results.[1,18] These values are close to values of the band gap energies found by Guo *et al.* 3.60 eV-(direct) and 3.30 eV(indirect) for crystalline and 3.55 eV(direct) and 2.96 eV(indirect) for amorphous.[1] The solid line in Fig. 10 shows the tendency of increasing band gap energy as a grain size decreasing to 50 nm grain size, which is possibly explained by quantum confinement effect (dashed line in Fig.

which means the density of states is changed by the decrease in grain size. The change in the density of states with grain size is probably related to the specimens becoming more amorphous as the grain size decreased. The effect is also seen in doped specimens and the values of the effective mass were about 0.1 lower than those of undoped specimens. The effect of the dopant also appeared in the effective mass, which corresponds to the reduction of the extinction coefficient.

IV. SUMMARY

The results of a study of the formation and the microstructure of undoped and Gd-doped CeO_2 thin films obtained by a polymeric precursor spin coating technique have been presented. The preparation method allowed crystalline film formation temperatures to be decreased such that it was possible to obtain dense thin films with the grain size in the nanometer range (4–150 nm) on the sapphire substrates with the annealing temperatures ranging from 350 to 1200 °C.

Using Fresnel equations, the energy dependent refractive index, n and extinction coefficient, k were calculated from transmission spectra. Both the n and k of thin films decreased as grain size decreased which could be related to the transition from the crystalline to amorphous state. The addition of Gd had little influence on n ($<5\%$), but resulted in about a 30%–40% reduction of k, which can be related to a decrease in concentration of absorption centers (Ce–O–Ce) due to replacement of Ce by Gd. The behavior of the band gap energies determined from direct and indirect transition as a function of grain size was also determined and found to decrease for grain size <50 nm for both undoped and 20%Gd-doped CeO_2. From the optical property point of view, the grain boundary region could not be considered to be amorphous, however, it showed the transition from crystalline to amorphous with the decrease of grain size for optical related properties in CeO_2 thin films. Optical properties of nanocrystalline specimens showed systematic changes which suggest that their optical character can be controlled by microstructure.

ACKNOWLEDGMENTS

The authors would like to thank the Department of Energy, Contract No. DE-AC26-99FT40710 and Unitika Ltd. for financial support of this research.

[1] S. Guo, H. Arwin, S. N. Jacobsen, K. Järrendahl, and U. Helmersson, J. Appl. Phys. **77**, 5369 (1995).
[2] R. M. Bueno, J. M. Martinez-Duart, M. Hernandez-Velez, and L. Vazquez, J. Mater. Sci. **32**, 1861 (1997).
[3] A. Hartridge, M. G. Krishna, and K. Bhattacharya, J. Phys. Chem. Solids **59**, 859 (1998).
[4] M. I. Freedhoff and A. P. Marchetti, *Optical Properties* (CRC, New York, 1997), Vol. 2, pp. 1–30.
[5] L. E. Brus, J. Chem. Phys. **80**, 4403 (1984).
[6] I. Kosacki, V. Petrovsky, and H. U. Anderson, Appl. Phys. Lett. **74**, 341 (1999).
[7] I. Kosacki, T. Suzuki, and H. U. Anderson, in *Innovative Processing/Synthesis: Ceramics, Glasses, Composites III* (The American Ceramic Society, 2000), pp. 275–284.
[8] I. Kosacki and H. U. Anderson, Mater. Res. Soc. Symp. Proc. **453**, 537 (1997).
[9] Y. M. Chiang, E. B. Lavik, I. Kosacki, H. L. Tuller, and J. Y. Ying, J. Electroceram. **1**, 7 (1997).
[10] I. Kosacki, T. Suzuki, and H. U. Anderson, Proc. Meeting Electrochem. Soc., **99**, 190 (1999).
[11] Z. Crnjak Orel and B. Orel, Phys. Status Solidi B **186**, K33 (1994).
[12] H. U. Anderson, M. M. Nasrallah, and C. C. Chen, U.S. Patent No. 5,494,700 (1996).
[13] B. D. Cullity, *Elements of X-ray Diffraction* (Addison-Wesley Reading, MA, 1959).
[14] C. F. Bohren and D. R. Huffman, *Absorption and Scattering of Light by Small Particles* (Wiley, New York, 1983).
[15] T. Suzuki, I. Kosacki, H. U. Anderson, and P. Colomban, J. Am. Ceram. Soc. **84**, (2001).
[16] T. Suzuki, I. Kosacki, and H. U. Anderson, Electrochem. Soc. Proc. **32**, 190 (2000).
[17] M. W. Barsoum, *Fundamentals of Ceramics* (McGraw-Hill, New York, 1997).
[18] L. Mechin, A. Chabli, F. Bertin, M. Burdin, G. Rolland, C. Vannuffel, and J. C. Villegier, J. Appl. Phys. **84**, 4935 (1998).
[19] C. J. Brinker and G. W. Scherer, *Sol-Gel Science: The Physics and Chemistry of Sol-Gel Processing* (Academic, San Diego, CA, 1990).
[20] V. Petrovsky, H. U. Anderson, and T. Petrovsky, Mater. Res. Soc. Symp. Proc. **581**, 553 (2000).
[21] H. Gleiter, Mater. Sci. **33**, 223 (1989).
[22] I. Kosacki, T. Suzuki, and H. U. Anderson, Ceram. Trans. **108**, 275 (2000).
[23] P. Bhattacharya, *Semiconductor Optoelectronic Devices* (Prentice-Hall, Upper Saddle River, NJ, 1993).

Appendix D

Chapter 7: Interconnects
F. Tietz, and H.U. Anderson
Solid Oxide Fuel Cells: Fundamentals and Applications

Chapter 7 Interconnects

Frank Tietz
Forschungszentrum Jülich, IWV-1, D-52425 Jülich

Harlan U. Anderson
Electronic Materials Applied Research Center (EMARC)
University of Missouri-Rolla

Introduction

The role of the interconnect in the high temperature solid oxide fuel cell (SOFC) is that of electrical connection between cells and gas separation within the cell stack. The fact that the interconnect must be compatible with all of the cell components as well as be stable with respect to both oxidising and reducing gases places very stringent materials requirements on it. These requirements plus the additional constraints of cost and ease of fabrication tends to limit the possible choices to only a few candidates. The most highly touted candidates come from either perovskite-type oxides with the rare earth chromites being the leading choices for operating temperatures in the 900 to 1000°C range or metal alloys for lower temperature operation. The primary difficulties that have been encountered are: cost of materials, fabrication and compatibility with other cell components both during fabrication and use.

The properties which an interconnect must possess are rather extensive and somewhat dependent upon the particular SOFC configuration[1]. However, typical requirements are:

1) High electronic conductivity with low ionic conductivity
2) Chemical stability in both fuel and air
3) Thermal expansion match to other cell components
4) High mechanical strength
5) High thermal conductivity
6) Chemical stability with regard to other cell components

Depending upon the particular SOFC design, additional requirements such as ease of fabrication to gas tight density, the ability to make gas tight seals between it and the other components and materials costs also play an important role.

It is the intent of this chapter to review 1) the requirements of interconnect materials; 2) the characteristics that the leading candidates possess; 3) how well the interconnect requirements are being fulfilled; and 4) what are the current and future research needs. For the sake of clarity, the discussion is separated into two parts: ceramic and metallic interconnects.

7.1 Ceramic Interconnects

The requirements on the interconnect material for the high temperature SOFC are very stringent. Of the requirements listed above, the first three are the most crucial and tend to eliminate most candidate materials. In fact, for operation at temperatures >800°C the only oxides that fit these

criteria are the acceptor substituted rare earth chromites. In particular, compositions from the system (La,Sr,Ca)(Cr,Mg)O_3 are the leading interconnect candidates. However, compositions from the system (Y,Ca)CrO_3 also have acceptable properties. These rare earth chromites fit most of the requirements, but present problems with fabrication and cost which represent the most outstanding research challenges and must be dealt with if SOFC's are to become economically viable.

The desire to decrease the operating temperature of SOFC's to the temperature range 600-800°C, may broaden the scope of available interconnect materials, but at the moment, there are no new oxide systems being considered. Thus, this review will focus on the chromite systems.

7.1.1 Properties of La & Y Chromites

7.1.1.1 *Electrical Conductivity*

The electronic conductivity that is required for an interconnect to perform adequately is a $\sigma > 1$ S/cm at 1000°C. For either $YCrO_3$ to $LaCrO_3$ to obtain this level of conductivity, acceptor doping is required. Tables 7.1 and 7.2 list typical values that are obtainable.

Table 7.1 Electrical Conductivity Data for Substituted $LaCrO_3$ (Air)

Dopant	Composition (mol %)	Electrical Conductivity (1000°C) ($\Omega^{-1}cm^{-1}$)	Activation Energy (eV) (kJ/mol)	Ref.
0	0	1	(0.19) (18)	2
Mg	10	3	(0.20) (19)	3
Sr	10	14	(0.12) (12)	4
Ca	20	35	(0.14) (13)	5
Ca, Co	20 Ca, 10 Co	34	(0.15) (14)	6

Table 7.2 Electrical Conductivity Data for Ca Substituted$YCrO_3$ (Air)

Ca Contant (mol%)	Electrical Conductivity (1000°C) (S/cm)	Activation Energy (eV) (kJ/mol)	Ref.
5	4.5	(0.17) (16)	7
10	7.7	(0.18) (17)	7
15	13.0	(0.18) (17)	7
20	15.5	(0.18) (17)	7

Upon exposure to reducing atmospheres all oxides tend to lose oxygen and form oxygen vacancies. In the case of p type oxides like Y and La chromite, the lose of oxygen results in a decrease in electrical conductivity. Figure 7.1 illustrates the behaviour that these oxides display[7]. Figures 7.2 and 7.3 show how the electrical conductivity changes with oxygen activity for both of these chromites[2,6]. What makes the chromites useful as interconnects is that at 1000°C and 10^{-16} bar oxygen, they remain single phase and do not dissociate. There are no other oxides which have these levels of electrical conductivity and can survive such reducing

conditions. Thus, the chromites are quite unique and are the only oxides available for use as interconnects. The $LaCrO_3$ doped with either Ca or Sr have sufficient conductivity in fuel to exceed 1 S/cm so are preferred to Mg doped $LaCrO_3$.

There has been some concern about the oxygen ion conductivity in $(La,SrCa)CrO_3$, particularly under reducing conditions, but studies by Yokokawa, et. al.[8] and Singhal[9] suggest that this is not a serious problem since at 1000°C the oxygen diffusion coefficient appears to be less than 10^{-7} cm^2/sec. This would yield an ionic transport number of less than 1% even at the most reducing conditions. Thus, so oxygen permeation through the interconnect should be minimal regardless of the configuration.

<INSERT FIGURE 7.1>

<INSERT FIGURE 7.2>

<INSERT FIGURE 7.3>

7.1.1.2 *Thermal Expansion*

It is important that the thermal expansion coefficients of all SOFC components match well. This is particularly true for the dense components, the electrolyte (Y_2O_3-ZrO_2, YSZ) and the interconnect. Table 7.3 compares the thermal expansion coefficients (TEC's) and shows that the TEC's of $LaCrO_3$ and $YCrO_3$ do not match that of YSZ, but the addition of acceptors makes the match possible. Thus, thermal expansion is not a significant problem. However, as has been previously reported, the loss of oxygen in a reducing atmosphere leads to lattice expansion which has the potential of causing cracking problems[10-18]. For example, at 1000°C, when exposed to hydrogen, $LaCr_{0.85}Mg_{0.15}O_3$ and $La_{0.8}Sr_{0.2}CrO_3$ each expand about 0.1% and 0.3% respectively (see Figure 7.4). The amount of expansion due to oxygen loss is directly related to the oxygen vacancy concentration. Several studies have shown that this expansion can be minimised by the addition of elements such as Al and Ti, but it is difficult to completely avoid this behaviour without the loss of other desirable properties, such as the electrical conductivity.[16,18] Thus, it is important to allow for this in the cell design.

Table 7.3 Thermal Expansion Coefficient of $LaCrO_3$ & $YCrO_3$[1-13]

Composition (Nominal)	Thermal Expansion Coefficient ($\times 10^{-6}$ K^{-1})
$LaCrO_3$	9.5
$LaCr_{0.9}Mg_{0.1}O_3$	9.5
$La_{0.9}Sr_{0.1}CrO_3$	10.7
$La_{0.8}Sr_{0.2}CrO_3$	11.1
$La_{0.65}Ca_{0.35}CrO_3$	10.8
$LaCr_{0.9}Co_{0.1}O_3$	13.1
$La_{0.8}Ca_{0.2}Cr_{0.9}Co_{0.1}O_3$	11.1
$YCrO_3$	7.8
$Y_{0.9}Ca_{0.1}CrO_3$	8.9
$Y_{0.8}Ca_{0.2}CrO_3$	9.6

Y stabilized ZrO_2	9.4-11

<INSERT FIGURE 7.4>

7.1.1.3 *Thermal Conductivity and Mechanical Strength*

The thermal conductivity of the SOFC components are all in the order of 1.5-2 $Wm^{-1}K^{-1}$ [3]. These are low compared to 20 $Wm^{-1}K^{-1}$ for stainless steel and 400 $Wm^{-1}K^{-1}$ for copper, so heat dissipation is a problem which is inherent in the materials so must be considered in the SOFC design. This is particularly true for the higher power density monolithic and planar SOFC's, but is less of a problem in the tubular design.

The mechanical strength of many compositions of $LaCrO_3$ is low compared to YSZ (see Table 7.4) and appears to be variable. The low strength and variability appears to be related to structural flaws due to inhomogeneities in composition, grain size and/or density and not to the $LaCrO_3$ itself. Thus, improvements in processing can alleviate this problem.

Table 7.4 Mechanical Strength of $LaCrO_3$ (MPa)

Dopant	Temperature			Ref.
	25°C	1000° (air)	1000° (H_2)	
10% Mg	390-418			20
20% Mg	300			20
10% Sr	268	166		20
10% Sr	245	77		20
20% Sr	234			19
20% Sr		100	140	21
10% Ca	140	36		20
15% Ca		80	40	13
20% Ca	100-150	20-60	50-60	13,22
30% Ca	100-140	60-130	20	13
YSZ		200		13

7.1.2 Processing

In general, Cr containing oxides are difficult to sinter. The primary problem is related to the vaporisation of Cr-O which leads to enhancement of the evaporation-condensation mechanism of sintering which tends to suppress densification and causes coarsening of the powder.[22,23]

In the case of $LaCrO_3$ this problem was initially addressed by Groupp & Anderson who demonstrated that densification could be achieved by sintering at temperatures exceeding 1700°C in an oxygen partial pressure in the 10^{-10} – 10^{-9} bar range[24]. Under these conditions the Cr-O volatility is suppressed; thus, minimising the evaporation-condensation mechanism thereby allowing densification to occur. They showed that densification of stoichiometric $LaCrO_3$ is possible through a solid state sintering mechanism by controlling the sintering atmosphere, but unfortunately the required conditions are so extreme, that they are not compatible with the processing of the other SOFC components and are uneconomical.

Hot pressing has been considered as an alternative for densifying $LaCrO_3$. A number of studies have shown that hot pressing at temperatures in the 1500-1600°C range in graphite dies achieve > 93% of theoretical density. However, due to the low oxygen activity due to the C-O reaction, the $LaCrO_3$ dissociated to Cr metal both at the C/$LaCrO_3$ interface and in the grain boundaries. As a result upon reoxidation cracking occurred due to the Cr oxidation. Therefore, hot pressing has proven to be unsatisfactory both from a structural as well as economical point of view.

The densification problem has lead researchers to search for sintering aids which promote densification by suppressing of the Cr-O volatility and enhance mass transport through liquid phase mechanisms. Perhaps the first successful demonstration of this process was done by a group at Argonne National Laboratory who were attempting to co-sinter $LaCrO_3$ with the other SOFC components in their monolithic SOFC[25]. They showed that the addition of boron and fluorides of Sr and La promoted densification in air at temperatures as low as 1300°C. Due to the volatility and the interaction of the liquid phase with other components, this is a difficult process to control, but it does show that liquid phase sintering is a viable option.

Since this initial work, a number of other liquid promoters have been investigated and several systems have been rather successful. For example, Koc showed that compositions within the system $(La,Ca)(Co,Cr)O_3$ sintered well and yield nearly theoretically dense structures at temperatures as low as 1350°C[6]. These compositions are stable in a fuel atmosphere at 1000°C so are potential interconnect candidates. The main problem with these compositions is that the Ca, and Co tend to react with other cell components so long time stability is suspect[21].

In an effort to alleviate the Co migration problem a number of investigators have investigated the $(La,Cr)Cr_{1-y}O_3$ and $(La,Sr)Cr_{1-y}O_3$ systems[12,17,26-29]. What has been found is that when powders of these compositions are prepared at temperatures below 700°C, the powders tend to be multiphase with substantial quantities of either La, Ca, or Sr chromates present. These chromate phases melt incongruently in the 1000 to 1200°C range and the liquid promotes liquid phase sintering. Unfortunately, the best sintering compositions are Cr deficient and the excess A site components, La, Ca, or Sr tend to segregate to the grain boundaries and create hydration and cracking problems under both SOFC operating and ambient conditions. Thus, this method of sintering has not been entirely satisfactory, but until a better one is discovered, it is the one being most frequently employed in the planar SOFC configuration.

The search is still on to develop a method of densifying stoichiometric $LaCrO_3$ which is both economical and yields stable interconnects.

There are a number of methods used to fabricate the interconnect in the SOFC stack. The method used depends on the SOFC design.[30]

For the tubular design fabrication methods such as:

Electrochemical vapour deposition (EVD)
Plasma spraying
Laser ablation

Slurry coating and sintering

have been used, with EVD and plasma spraying being favoured. Economics is a problem with EVD while porosity and interfacial cracking are difficulties with plasma spraying. For the tubular design, economical deposition and the achievement of nonporous, crack free interconnects remains a problem with no apparent solution.

In the early 1980's the monolithic design attracted much attention and lead to a renewed interest in SOFC's. The design makes use of tape casting, lamination and calendaring technology to produce a structure which is then sintered to produce a completed SOFC stack. On the surface, this process is attractive since it offers the potential of low cost and high power density. In practice, it is a very difficult process because it requires the simultaneous sintering of all cell components. This means that the sintering shrinkages and shrinkage rates must be matched for all four cell components and interactions between components must be minimal. As a result, this design has been abandoned. Hopefully as we learn how to control the processes better, this monolithic design will become practical.

A variation of the monolithic design was introduced by Allied Signal[31] (now GE). This design co-sinters the electrolyte, cathode and anode, but fabricates the interconnect separately. This design has eliminated the fabrication incompatibility problem between the interconnect and other cell components, but it does have the seal problems with the planar design. The main advantage of this design is the densification of the interconnect by itself so it gives the option of liquid phase sintering the interconnect without inducing problems with the other cell components. Thus, the design offers nearer-term development than the monolithic cell.

The conventional planar cell designs build the gas distribution channels into the interconnect in a bipolar structure. In this design, good electrical contact between the cell components must be maintained and the edges sealed gas tight. These seals are made by either making glasses or cements which, when heated, both give gas tight seals and electrical contact. In addition to interlayer seals, side seals are required which are both electrically insulating and gas tight. A number of different schemes have been tried to provide these two seals, but at the moment they are a problem whose solutions are carefully protected by individual SOFC developers.

7.1.3 What Are The Challenges in Ceramic Interconnects?

There are a number of factors that can be listed which need to be addressed before a completely acceptable interconnect can be developed (see Table 7.5). However, most of them are of secondary importance when compared to the two major challenges:

REDUCTION OF FABRICATION COSTS

Reduction of material costs

These two items will probably determine whether SOFC's will become economically feasible. At the moment for all SOFC designs, the planar and monolithic in particular, these two items are the show stoppers. The most important challenge we have is to get fabrication and material costs under control. The reduction in material costs can be influenced by both design and the quantity of interconnect oxides required. However, reduction in fabrication costs will only come with improved processing and automation.[1,31,32]

Table 7.5 Current Interconnect Problems	
Of Most Importance	Of Next Most Importance
1) Fabrication and Processing Costs 2) Materials Costs	1) Thermal Expansion Matches to YSZ 2) Chemical Compatibility to YSZ and Sealing Glass or Cement 3) Expansion Due to Loss of Oxygen 4) Mechanical Strength and Durability in Reducing Atmosphere 5) Electrical Conductivity in Reducing Atmosphere

7.2 Metallic Interconnects

The advantages of metallic interconnects against ceramic interconnects are obvious: lower material and production cost, easier and more complex shaping, better electrical and thermal conductivity and no deformation or failure due to the different gas atmospheres across the plate. The interconnects can be structured by machining, pressing or, in the case of powder metallurgical alloys, by near-net-shape sintering. The gas distribution is usually realised by parallel channels and the ridges separating the channels serve as electrical contact with the electrodes.

Historically, metallic interconnects were introduced in SOFC development in the early nineties. To our knowledge the first reports on SOFC stacks built with metallic interconnect plates were published by NKK Corp.[33] and Sanyo.[34] Before, already very first experiments with FeNiCr alloys have shown a steady decrease in power output during fuel cell operation[35], and later also in stack tests.[36] Already in 1994 this deterioration was ascribed to the release of chromium from the alloy leading to catalytic poisoning of the cathode.[37,38] This phenomenon has been investigated intensively, is fairly well understood today and described in chapter 7.2.4. All early attempts in using metals as interconnect were not very successful, because the heat-resistant steels often contained a significant amount of Ni leading to large mismatches between the metal and the ceramic SOFC components.

7.2.1. Chromium-based alloys

This situation changed when after a screening of different chromium-based alloys the Metallwerke Plansee AG proposed an alloy of the composition Cr 5Fe 1Y_2O_3, so-called Durolloy, to be used for electrolyte-supported SOFC's.[39] In a close collaboration with Siemens AG this alloy was used for assembling SOFC stacks in the 1-10 kW range.[41,42] The alloy composition was optimised with respect to the thermal expansion of yttria-stabilised zirconia (YSZ) to guarantee thermal cycling of stacks.[43] The good match of thermal expansion is shown in Figure 7.5. Only at temperatures above 800°C the increased thermal expansion of the alloy leads to deviations from the thermal expansion of YSZ and the two materials differ at 1000°C by 8 %.

<INSERT FIGURE 7.5>

Beside the stack development the alloy was investigated in detail with respect to corrosion behaviour[43,44] and contact resistance across the interfaces towards the electrodes.[45] Typically, Cr 5Fe 1Y_2O_3 is a chromia former and even after long-term exposure in oxygen or air the chromia scales are very thin. Thicker corrosion scales grow in carbon containing atmospheres (methane, coal gas) due to formation of carbides.[44]

The processing of interconnect plates of Cr 5Fe 1Y_2O_3 has been carried out by powder metallurgical methods and starts with the alloying of Fe and Y_2O_3 to Cr flakes by high energy milling.[46] Then pressing and sintering in hydrogen atmosphere is followed by hot forming like hot rolling in vacuum. This sophisticated processing is the reason why such parts are almost as expensive as ceramic interconnects. Although a decrease in costs of about one order of magnitude (from about 1500 US$ for one interconnect plate in the R&D stage to about 100-150 US$ in mass production) have been estimated,[47] the Ducrolloy interconnects remain an expensive stack component. For the shaping of interconnects for the Siemens stacks electrochemical machining was applied.[39,47]
Recently the fabrication of near net-shape parts were reported.[48] The aim of this near net-shaping processing is the price objective of 10 US$ per current collector (∅ 120 mm) by avoiding machining and efficient use of the chromium powder.[49] For this purpose, however, a new materials development had to be carried out with different Cr powder grades, additional alloying elements and different oxide dispersoids to improve sinterability, pressing behaviour, resulting density, corrosion and contact resistance with thermally sprayed protective coating.[49,50] The best alloy compositions were found to be Cr 5Fe 0.3Ti 0.5CeO_2 and Cr 5Fe 0.5CeO_2 and an endurance stack test with one of these near net-shaped alloys showed very stable performance over time.

7.2.2. Ferritic steels

The first SOFC stacks built with ferritic steel were reported by Forschungszentrum Jülich.[51] A year later Ceramic Fuel Cells Ltd. (CFCL) reported on SOFC stacks in the kW range using ferritic interconnects and housing.[52] Sanyo tested ferritic steels and obtained good thermal cycling results.[53] Compared with Cr 5Fe 1Y_2O_3 the advantages of ferritic steels are the lower cost of the material, the easier processing and fabrication of components, weldability and the fitting thermal expansion with the anode substrate (Figure 7.5).

On the contrary, long-term stack tests have shown enhanced degradation of power output (a degradation rate between 2% and 25%/1000 h of operation[52,54] is typical) and that the corrosion behaviour for instance of the ferritic steel X10CrAl18 (DIN 1.4742) is not sufficient for the targeted 40000 h of operation of an SOFC system. Already after 3000 h of operation the growth of humpy corrosion products led to a partial detachment of the cathode contact layer from the cathode (Figure 7.6). Therefore it became evident to develop new steel compositions fulfilling better corrosion behaviour than the actual commercially available ferritic steels.

<INSERT FIGURE 7.6>

As a first attempt, Malkow et al. systematically investigated the thermal expansion and corrosion behaviour of commercial steels and model alloys.[55] The thermal expansion coefficient of ferritic steels decreases with increasing Cr content up to 20 wt.% and increases with increasing Al content. In this way the thermal expansion of the steel can be well adjusted to the anode substrate, but not to the YSZ electrolyte. The oxidation of the steels depends not only on the Cr content, but also on small amounts of alloyed elements, especially Al and Si. As soon as a compositional threshold is passed, alumina and silica layers are formed instead of chromia layer and reduce the weight gain during oxidation experiments. However, such insulating layers have to be avoided when the steel is in contact with a contact or electrode material. In a comparative study[56] of commercially available ferritic steels with chromium contents between 12 and 28% the contact resistance against the $La_{0.6}Sr_{0.4}Fe_{0.8}Co_{0.2}O_3$ perovskite strongly increased with time for those steels containing Al and Si in the range of 1-2 wt%. Best contact resistances were obtained with the steels X3CrTi17 (DIN 1.4509) and X2CrTiNb18 (DIN 1.4510) remaining below 10 $m\Omega\ cm^2$ after 4000 h of exposure. In corrosion experiments both steels formed scales composed of chromia and Fe-Mn-Cr spinels together with an inner oxidation of the stabilising elements Ti and Nb.[56]

Further progress have been made in steel development aiming at ferritic steels a) forming thin spinel-type corrosion scales with significant electrical conductivity and b) having well-adherent corrosion scales which reduce the release of volatile Cr species.[26,27]

By adding various alloying elements in the range of 0.1-2.5 wt% to FeCr17-25 alloys, the following classification was found:

- Ni: does not support a stable and protective scale formation
- Ti: leads to high weight changes due to enhanced growth rate of the chromia scale and formation of internal Ti oxidation
- Y, La, Ce, Zr: reduce the oxide growth rate independent of Cr content, especially La forms very thin oxide scales
- Mn: increases the scale growth rate even if a lanthanide elements is present, forms preferably a Cr-Mn spinel on top of a chromia scale with small electrical resistance

This systematic study led to the definition of an optimised steel composition – on laboratory scale – with small additions of Mn, La, and Ti but without any Al and Si. This steels has shown the desired thin and conductive oxide scales[57,58] as well as good contact resistances with ceramic coatings (Figure 7.7 and Ref. 59) and reduced permeability for volatile chromium species.[60]

<INSERT FIGURE 7.7>

A similar approach was made using FeCr18 steels containing 7-10 wt% W.[61] The increasing tungsten content resulted in thermal expansion coefficients close to YSZ and small additions of Ce, La or Zr led to reduced weight gains in corrosion experiments. In contact with lanthanum manganite always a Cr-Mn spinel/Cr_2O_3 double layer was formed.

Honegger et al.[62] investigated powder metallurgically made model steels containing 22-26% Cr and minor additions of Mo, Ti, Nb and Y_2O_3. After oxidation in air all samples showed a double-

layered oxide scale composed of chromia directly in contact with the alloy and Mn-Cr spinel at the outer surface. In humidified hydrogen (20 vol% H_2O) the corrosion experiments also revealed a Cr_2O_3/Cr-Mn spinel double layer at 700°C, but at higher temperatures a Fe-Cr spinel/Cr-Mn-Fe spinel system was formed. The contact resistance measurements performed on {steel/$La_{0.6}Sr_{0.4}CoO_3$ paste/$La_{0.8}Sr_{0.2}MnO_3$ ceramic} samples gave very small contact resistances at 800°C in air after 15000 h of exposure. With Mo-containing model alloys (FeCr22Mo2TiY_2O_3 and FeCr26Mo2TiY_2O_3) a contact resistance of 20 mΩ cm^2 for 40000 h can be deduced from the parabolic increase during the measurements.

Beside the materials development the improvement of stack design is an important issue to reach acceptable power densities in terms of W/kg and W/dm^3. Therefore the metallic interconnects are designed significantly thinner than several years ago as listed in Table 7.6 and thin steel foils (0.1-1 mm) are considered as stacking component.[63,64] Such foil interconnects can easily be mass produced by pressing, stamping, cutting and punching. How such a production line can look like is outlined in.[65] However, so far there are no results available about the corrosion behaviour of thin foils of ferritic steels which can be very different compared with thick sheets due to the effect of selective oxidation and depletion of alloyed elements leading to composition changes in the foil. Therefore stack tests over several thousand hours have to demonstrate the reliability of these light weight designs.

Table 7.6 Stack Developer and the Interconnect Materials They Have Used

Company	Interconnect material	Interconnect thickness (mm)	Method to avoid poisoning of the cathode by volatile chromium species	Ref.
Sanyo	Inconel 600	5-6	Additions of La_2O_3 in cathode	36
Siemens	Cr 5Fe 1Y_2O_3	ca. 3.5	Wet coating of $LaCoO_3$	39
Siemens	Cr 5Fe 1Y_2O_3	ca. 3.5	Plasma-sprayed coating of (La,Sr)CrO_3	78
Sulzer HEXIS	Cr 5Fe 1Y_2O_3		HVOF-sprayed coating of (Y,Ca)MnO_3	79
Sulzer HEXIS	Cr 5Fe 1Y_2O_3		HVOF-sprayed coating of $La_{0.8}Sr_{0.2}MnO_3$	49
Forschungszentrum Jülich	Ferritic steel	6	$LaCoO_3$ coatings	51
CFCL	Ferritic steel	3	Al_2O_3 coatings in gas channels, conductive coatings on the ribs	52

7.2.3. Other Metals

Sanyo and Fuji Electric started their stack development with metallic interconnects using nickel-based alloys such as Inconel 600 and Ni 22Cr, respectively.[36,66] In a long-term exposure experiment of 12000 h duration the electrical resistance of a Ni 20Cr alloy coated with $La_{0.6}Sr_{0.4}CoO_3$ did not change significantly and maintained below 10 mΩ cm^2, although the formation of $SrCrO_4$ was formed at the interface.[67] However, it was realised very early that thermal cycling with these steels is difficult and continuously led to voltage drops after each

cycle due to the mismatch in thermal expansion with the other cell components (Figure 7.5) leading to cracks at the interconnect/electrode interfaces.[66]

Nevertheless, few laboratories continued to explore the properties of austenitic steels and Ni-based superalloys to be applied in SOFC stacks. Linderoth et al.[68] investigated the oxidation resistance of the corrosion products of two Fe-Cr-Ni steels (Haynes 230, Inconel 601), one Ni-Cr steel (Inconel 657), and one Fe-Cr-Al steel (APM-Kanthal) beside the Plansee alloy. Among the Ni-containing steels the Haynes 230 showed the best oxidation resistance and the oxide scale composed of Cr_2O_3 and spinel might have better electronic conductivity than a pure chromia scale.

England and Virkar[69,70] selected thin foils of Ni-based superalloys (Inconel 625, Inconel 718, Hastelloy X and Haynes 230) as possible interconnect materials. In air, also in this study Haynes 230 showed the slowest oxidation with time and the formation of a Cr-Mn spinel at the outer surface of the samples leading to complete depletion of Mn in the inner part of the thin foil. Hastelloy X also formed a spinel layer in the beginning of the oxidation experiments and both alloys exhibited the lowest electronic resistance of the oxide scale formed. In wet hydrogen, the oxidation resistance was also the best for Haynes 230 but the oxide scale growth was much faster than in air,[70] chromia was the dominating phase in the oxide scale and hence the electronic resistance of the oxide scale was 1-2 orders of magnitude higher than after oxidation in air.

A new concept for interconnection is the application of FeCrAlY steels in combination with silver pins.[64] The FeCrAlY steels is used as a thin foil and forms quickly an alumina scale inhibiting the release of Cr from the steel. To avoid high resistances of the alumina scales, the steel foil is perforated with Ag pins acting as contacts between the anode of one cell to the cathode of the other cell. The use of silver is very attractive due to the low contact resistances observed.[64,71,72] However, the experiments were carried out for only short terms and problems regarding silver evaporation at temperatures > 700°C[64] and during thermal cycling[71] were already addressed.

7.2.4. Focal points of actual development

As mentioned before, the cell and stack performance decreased continuously as soon as metallic parts are attached to the fuel cells. The reason is one of the two main disadvantages of metallic interconnects: the release of volatile Cr species. In atmospheres containing water vapour the most volatile molecule is chromium acid, $H_2Cr(VI)O_4$,[38,73] which is transported with the oxidant gas through the cathode to the cathode/electrolyte interface, competes with the oxygen molecules for the electrochemically active sites and is blocking them after reduction to Cr(III).[73] The resulting increase in cathode polarisation can be detected by impedance measurements.[74,75] After the effect of catalytic blocking the ongoing transport and reduction of chromium species leads decomposition of the cathode perovskite material and the formation of spinels.[76,77] That is why much effort has been spent on minimising the chromium transport in the cathode compartment, either by using “getter” materials like additions of La_2O_3[36] in the cathode or by applying protective coatings of lanthanum chromites,[45,78] lanthanum manganites[49] or yttrium manganites[79] (Table 7.6). The thermally sprayed coatings of Sulzer have led to stable long-term

performance lasting about 12000 h with a degradation rate of cell voltage of less than 1%/1000 h.[80]

Today the Cr evaporation from steels or alloys and the effectiveness of such protective coatings can be measured before stack assembling by transpiration experiments.[74,81] These investigations give on the one hand a clear guideline for materials development and on the other hand a better understanding of the high degradation rates during cell and stack testing.
Matsuzaki and Yasuda reported that $La_{0.6}Sr_{0.4}Fe_{0.8}Co_{0.2}O_3$ cathodes are much more stable against Cr poisoning than $La_{0.85}Sr_{0.15}MnO_3$ or $Pr_{0.6}Sr_{0.4}MnO_3$ cathodes,[82] especially when ceria-based solid electrolytes are used and that no enrichment of chromium is found at the $La_{0.6}Sr_{0.4}Fe_{0.8}Co_{0.2}O_3$/ceria interface (after 10 h of testing). A possible explanation might be the different overvoltages of the cathodes for oxygen and $H_2Cr(VI)O_4$ reduction. While for the manganites the reduction of the chromium oxyhydroxide is the energetically preferred reaction, in the presence of the ferrite the reduction of oxygen seems to need less activation energy. Although the exposure times are short in their experiments and more information has to be collected in further studies, the modification of cathodes may be a possible alternative to avoid Cr poisoning and protective coatings.

The second major disadvantage of metallic interconnects is the formation of corrosion scales leading to significant Ohmic losses. Therefore the interaction of the steel with the adjacent ceramic material and the resulting time-dependent resistance of these material combinations is highly important. In the case of Cr 5Fe $1Y_2O_3$ the best contact material for the cathode compartment was found to be $LaCoO_3$[45] before protective layers of $(La,Sr)CrO_3$ were applied to avoid the Cr evaporation. Also in combination with ferritic steel $LaCoO_3$ was successfully used,[51] although the thermal expansion coefficient of the cobaltite is by far higher[45,83] than the other SOFC materials.[84] Beside the lower contact resistance (Figure 7.7) the $LaCoO_3$ seems to react with and therefore to retain the Cr vapour.

7.3. Contact Materials

In general contact materials are used in stack assembling for better contact between the interconnect plates and the electrodes but also for compensation of tolerances after fabrication of the parts. Such contact layers have no direct electrochemical impact on stack performance but they can guarantee a homogeneous contact over the whole area of the fuel cell and minimise the Ohmic losses within the stack. For former SOFC types, which were made of ceramic components only,[85,86] the join between the SOFC and the $LaCrO_3$ interconnect was realised by a sintering process at about 1300°C and a solid, stiff bond with good electrical contact was obtained. The maximum assembling temperature depends on the interconnect material used. In the case of Cr 5Fe $1Y_2O_3$ the assembling can also be carried out by a sintering step due to the high melting point of 1700°C of the alloy.[39] However, using ferritic steels the assembling temperature should not be higher than 900-950°C due to enhanced corrosion.

Because there are no electrochemical requirements to be obeyed for the contact materials, they can vary significantly from the electrode materials and be optimised with regard to other physical and chemical properties than the electrodes. Most important physical properties are electrical

conductivity and thermal expansion. Because the contact layer thickness may vary between 30 and 200 µm and ceramic materials heat treated below 1000°C are usually very porous, the specific conductivity of the material should be high. This is in fact the case for lanthanum cobaltites having specific conductivities up to 1700 S/cm.[83] On the contrary the thermal expansion of these cobaltites has a strong mismatch with the other cell components as mentioned before. For electrically conductive ceramics therefore a compromise between acceptable conductivity and tolerable mismatch in thermal expansion has to be made.

A chemical interaction between contact layer and electrode as well as interconnect should not occur, but cannot be avoided in most cases due to the reaction of the contact material with the chromia scale formed. In all cases where alkaline earth-containing contact material was used, the formation of chromates was observed[45,59,67,87,88] leading to progressive decomposition of the perovskite material. A detrimental failure due to strong interface reaction was found for the alkaline earth-rich high-temperature superconductors like $Bi_2Sr_2CuO_{6+x}$.[89]

Therefore the change in contact resistance (Figure 7.7) is not only the reason of the scale formation on the surface of the interconnect but also driven by the reaction with the contact material, by the products formed and the steady depletion of material at the interface due to the volatility of the chromates. The latter process was unintentionally demonstrated by Hou et al.[90] applying different cathode materials – (i) Pt, (ii) $La_{0.6}Sr_{0.4}CoO_3$, (iii) $La_{0.85}Sr_{0.15}MnO_3$ + $La_{0.8}Sr_{0.2}Ga_{0.83}SMg_{0.17}O_3$ – onto an un-oxidised Fe-based alloy with composition similar to X18CrN28. They found that the area-specific resistance of the cobaltite specimen increased much stronger with time than the two other material combinations although the cobaltite is more conductive than the manganite/gallate mixture. Hence, for the development of stacking material it is not only important to have small contact resistances in the beginning but also constant resistance with time (or even a decreasing resistance as shown in Figure 7.7).

Often the corrosion on the anode side is neglected because Ni meshes are used and make good electrical contact with the interconnect. However, also the Ni wires are corrosively attacked during long-term stack tests (Figure 7.8). The reason is the interdiffusion of the metals across the interface: Fe and Cr diffuse into the Ni wire and Ni diffuses into the interconnect.[59] Such deterioration of contacts can be effectively avoided by an additional Ni coating on the interconnect.[91] In this case an interdiffusion cannot be avoided either, but the diffusion zone is not in contact with the gas atmosphere and no inner oxidation can occur, i.e. the formation of Ni-Cr oxides as shown in Figure 7.8.

<INSERT FIGURE 7.8>

7.4 Conclusions

The improvement of metallic interconnect materials as well as the contact layers between fuel cells and interconnect plates is still an issue for materials development. Especially the metal/ceramic interface is very challenging because low corrosion and interaction, low contact resistance as well as low permeability of chromium species shall be realised, if possible, with only one functional layer. The recent results have shown that a) optimised steels for SOFC applications are figured out and, b) alkaline earth-free and cobalt-containing perovskites are the

most suitable materials for contact layers. However, solutions for stacking with permanently low resistances can only be reliably evaluated in long-lasting experiments of more than a year, i.e. in tests of about 10000 h duration or more.

Acknowledgement

Harlan U. Anderson wishes to thank the Department of Energy and the Gas Research Institute for financial support and all of the hardworking graduate students who did the work which contributed to this review. Frank Tietz thanks the whole SOFC team at FZJ for excellent cooperation.

References

1. N. Q. Minh, T. Takahashi, in: Science and Technology of Ceramic Fuel Cells, Elsevier, Amsterdam, 1995
2. D. P. Karim, A.T. Aldred, *Phys. Rev. B* 20 (1979) 2255
3. B. F. Flandermeyer, M. M. Nasrallah, D. M. Sparlin, H. U. Anderson, *High Temp. Sci*. 20 (1985) 259
4. W. J. Weber, C. W. Griffin, J. B. Bates, *JACS* 70 (1987) 265
5. I. Yasuda & T. Hikita, in: Proc. 2nd Int. Symp. Solid Oxide Fuel Cells (SOFC-II), Athens, Greece, p. 632, eds. F. Grosz, P. Zegers, S. C. Singhal, O. Yamamoto, Commission of the European Committees, Luxenbourg (1991)
6. R. Koc, H. U. Anderson, *J. Mat. Sci*. 27 (1992) 5477
7. G. F. Carini II, H. U. Anderson, D. M. Sparlin, M. M. Nasrallah, *Solid State Ionics* 49 (1991) 233
8. H. U. Anderson, C. C. Chen, L-W. Tai, M. M. Nasrallah, in: Proc. 2nd Int. Symp. Ionic and Mixed Conducting Oxides, p. 376, eds. T. A. Ramanarayanan, H. L. Tuller, and W. L. Worrell, The Electrochemical Society, Pennington, NJ (1994)
9. H. Yokokawa, T. Horita, N. Sakai, B. A. Van Hassel, T. Kawada, M. Dokiya, in: Proc. 3rd Int. Symp. Solid Oxide Fuel Cells (SOFC-III), eds.: S. C. Singhal, H. Iwahara, Honolulu, USA, p. 364, The Electrochemical Society, Pennington, NJ (1993)
10. S. C. Singhal, "Interconnection Material Development for Solid Oxide Fuel Cells", DOE contract #DE-AC21-84MC21184, Final Report (1985)
11. S. Srilomsak, D. P. Schilling, H. U. Anderson in: Proc. 1st Int. Symp. Solid Oxide Fuel Cells, p. 129, ed. S.C. Singhal, The Electrochemical Society., Pennington, NJ (1989)
12. M. M. Nasrallah, J. D. Carter, H. U. Anderson, R. Koc, in: Proc. 2nd Int. Symp. Solid Oxide Fuel Cells (SOFC-II), Athens, Greece, p. 637, eds. F. Grosz, P. Zegers, S. C. Singhal, O. Yamamoto, Commission of the European Committees, Luxenbourg (1991)
13. M. Dokiya, T. Horita, N. Sakai, T. Kawada, H. Yokokawa, B. A. van Hassel, C. S. Montross, in: High Temperature Electrochemical Behaviour of Fast Ion and Mixed Conductors, Roskilde, Denmark, p. 33, eds. F. W. Poulsen, J. J. Bertzen, T. Jacobson, E. Skou, M. J. L. Østergård, Risø Natl. Lab., Denmark (1993)
14. A. Zuev, L. Singheiser, K. Hilpert, *Solid State Ionics* 147 (2002) 1
15. F. Boroomand, E. Wessel, H. Bausinger, K. Hilpert, *Solid State Ionics* 129 (2000) 251
16. M. Mori, Y. Hiei, *J. Am. Ceram. Soc*. 84 (2001) 2573
17. S. P. Simner, J. S. Hardy, J. W. Stevenson, *J. Electrochem. Soc*. 148 (2001) A351

18. G. Pudmich, B. A. Boukamp, M. Gonzalez-Cuenca, W. Jungen, W. Zipprich, F. Tietz, *Solid State Ionics* 135 (2000) 433
19. N. M. Sammes, R. Ratnaray, in: High Temperature Electrochemical Behaviour of Fast Ion and Mixed Conductors, Roskilde, Denmark, p. 403, eds. F. W. Poulsen, J. J. Bertzen, T. Jacobson, E. Skou, M. J. L. Østergård, Risø Natl. Lab., Denmark (1993)
20. M. Mori, H. Itoh, N. Mori, & T. Abe in "Proceedings of the 3rd Intl. Symp. on Solid Oxide Fuel Cells", Proceedings Vol. 93-4, Electrochem. Soc., eds. S. C. Singhal & H. Iwahara, pp. 325-335 (1993)
21. C. Milliken, S. Elangovan, A. Khandhar, in: Proc. 3rd Int. Symp. Solid Oxide Fuel Cells (SOFC-III), Honolulu, USA, p. 335, eds.: S. C. Singhal, H. Iwahara, The Electrochemical Society, Pennington, NJ (1993)
22. S. W. Paulik, S. Baskaran, T. R. Armstrong, *J. Mat. Sci*. 33 (1998) 2397
23. D-H. Peck, M. Miller, K. Hilpert, *Solid State Ionics* 143 (2001) 391
24. L. Groupp, H. U. Anderson, *J. Am. Ceram. Soc*. 59 (1976) 449
25. B. K. Flandermeyer, R. B. Poeppel, J. T. Dusek, H. U. Anderson, U.S. Patent #4749632, June 7, 1988
26. J. D. Carter, V. Sprenkle, M. M. Nasrallah, H. U. Anderson, in: Proc. 3rd Int. Symp. Solid Oxide Fuel Cells (SOFC-III), Honolulu, USA, p. 344, eds.: S. C. Singhal, H. Iwahara, The Electrochemical Society, Pennington, NJ (1993)
27. L. A. Click, T. R. Armstrong, D. E. McCready, G. W. Coffey, G. D. Maupin, J. L. Bates, in: Proc. 3rd Int. Symp. Solid Oxide Fuel Cells (SOFC-III), Honolulu, USA, p. 374, eds.: S. C. Singhal, H. Iwahara, The Electrochemical Society, Pennington, NJ (1993)
28. M. Mori, Y. Hiei, N. M. Sammes, *Solid State Ionics* 135 (2000) 743
29. L. A. Click, J. Liu, J. W. Stevenson, T. R. Armstrong, D. E. McCready, G. D. Maupin, G. W. Coffey, C. A. Coyle, *J. Am. Ceram. Soc*. 80 (1997) 2109
30. S. C. Singhal, *Solid State Ionics* 135 (2000) 305
31. N. Q. Minh, *J. Am. Cer. Soc*. 76 (1993) 563
32. B. C. H. Steele, *Solid State Ionics* 134 (2000) 3
33. H. Tsuneizumi, E. Matsuda, T. Kadowaki, T. Shiomitsu, H. Nakagawa, Y. Watanabe, T. Yokosuka, in: Proc. 1st Int. Fuel Cell Conf. (IFCC-1), Makuhari, Japan, p. 293, NEDO/MITI (1992)
34. Y. Akiyama, T. Yasuo, N. Ishida, in: Proc. 3rd Int. Symp. Solid Oxide Fuel Cells (SOFC-III), Honolulu, USA, p. 724, eds.: S. C. Singhal, H. Iwahara, The Electrochemical Society, Pennington, NJ (1993)
35. J. Jung, Th. Martens, H. Runge, M. Turwitt, in: Proc. 2nd Int. Symp. SOFC (SOFC-II), Athens, Greece, eds.: F. Grosz, P. Zegers, S. C. Singhal, O. Yamamoto, p. 144, Commission of the European Communities, Luxembourg (1991)
36. Y. Miyake, T. Yasuo, Y. Akiyama, S. Taniguchi, M. Kadowaki, H. Kawamura, T. Saitoh, in: Proc. 4th Int. Symp. Solid Oxide Fuel Cells (SOFC-IV), Yokohama, Japan, p. 100, eds.: M. Dokiya, O. Yamamoto, H. Tagawa, S. C. Singhal, The Electrochemical Society, Pennington, NJ (1995)
37. Y. Akiyama, S. Taniguchi, T. Yasuo, M. Kadowaki and T. Saitoh, *J. Power Sources* 50 (1994) 361
38. D. Das, M. Miller, H. Nickel, K. Hilpert, in: Proc. 1st Eur. SOFC Forum, Lucerne, Switzerland, Vol. 2, p. 703, ed.: U. Bossel, European SOFC Forum, Oberrohrdorf, Switzerland (1994)

39. W. Köck, H.-P. Martinz, H. Greiner, M. Janousek, in: Proc. 4th Int. Symp. Solid Oxide Fuel Cells (SOFC-IV), Yokohama, Japan, p. 841, eds.: M. Dokiya, O. Yamamoto, H. Tagawa, S. C. Singhal, The Electrochemical Society, Pennington, NJ (1995)
40. L. Blum, W. Drenckhahn, H. Greiner, E. Ivers-Tiffée, in: Proc. 4th Int. Symp. Solid Oxide Fuel Cells (SOFC-IV), Yokohama, Japan, p. 163, eds.: M. Dokiya, O. Yamamoto, H. Tagawa, S. C. Singhal, The Electrochemical Society, Pennington, NJ (1995)
41. H. J. Beie, L. Blum, W. Drenckhahn, H. Greiner, B. Rudolf, H. Schichl, in: Proc. 5th Int. Symp. Solid Oxide Fuel Cells (SOFC-V), Aachen, Germany, p. 51, eds.: U. Stimming, S. C. Singhal, H. Tagawa, W. Lehnert, The Electrochemical Society, Pennington, NJ (1997)
42. W. Quadakkers, H. Greiner, W. Köck, in: Proc. 1st Eur. SOFC Forum, Lucerne, Switzerland, p. 525, ed.: U. Bossel, European Fuel Cell Forum, Oberrohrdorf (1994)
43. H. Greiner, Th. Grögler, W. Köck, R. F. Singer, in: Proc. 4th Int. Symp. Solid Oxide Fuel Cells (SOFC-IV), Yokohama, Japan, p. 879, eds.: M. Dokiya, O. Yamamoto, H. Tagawa, S. C. Singhal, The Electrochemical Society, Pennington, NJ (1995)
44. W. Thierfelder, H. Greiner, W. Köck, in: Proc. 5th Int. Symp. Solid Oxide Fuel Cells (SOFC-V), Aachen, Germany, p. 1306, eds.: U. Stimming, S. C. Singhal, H. Tagawa, W. Lehnert, The Electrochemical Society, Pennington, NJ (1997)
45. H. Schmidt, B. Brückner, K. Fischer, in: Proc. 4th Int. Symp. Solid Oxide Fuel Cells (SOFC-IV), Yokohama, Japan, p. 869, eds.: M. Dokiya, O. Yamamoto, H. Tagawa, S. C. Singhal, The Electrochemical Society, Pennington, NJ (1995)
46. R. Eck, H.-P. Martinz, T. Sasaki, Mater. Sci. Eng. A, 120 (1989) 307
47. M. Janousek, W. Köck, M. Baumgärtner, H. Greiner, in: Proc. 5th Int. Symp. Solid Oxide Fuel Cells (SOFC-V), Aachen, Germany, p. 1225, eds.: U. Stimming, S. C. Singhal, H. Tagawa, W. Lehnert, The Electrochemical Society, Pennington, NJ (1997)
48. Glatz, M. Janousek, E. Batawi, K. Honegger, in: Proc. 4th Eur. SOFC Forum, Lucerne, Switzerland, Vol. 2, p. 855, ed.: A. McEvoy, Eur. Fuel Cell Forum, Oberrohrdorf, Switzerland (2000)
49. E. Batawi, W. Glatz, W. Kraussler, M. Janousek, B. Doggwiler, R. Diethelm, in: Proc. 6th Int. Symp. Solid Oxide Fuel Cells (SOFC-VI), Honolulu, Hawaii, p. 731, eds.: S. C. Singhal, M. Dokiya, The Electrochemical Society, Pennington, NJ (1999)
50. W. Glatz, E. Batawi, M. Janousek, W. Kraussler, R. Zach, G. Zobl, in: Proc. 6th Int. Symp. Solid Oxide Fuel Cells (SOFC-VI), Honolulu, Hawaii, p. 783, eds.: S. C. Singhal, M. Dokiya, The Electrochemical Society, Pennington, NJ (1999)
51. H. P. Buchkremer, U. Diekmann, L. G. J. de Haart, H. Kabs, U. Stimming, D. Stöver, in: Proc. 5th Int. Symp. Solid Oxide Fuel Cells (SOFC-V), Aachen, Germany, p. 160, eds.: U. Stimming, S. C. Singhal, H. Tagawa, W. Lehnert, The Electrochemical Society, Pennington, NJ (1997)
52. S. P. S. Badwal, R. Bolden, K. Föger, in: Proc. 3rd Eur. SOFC Forum, Nantes, France, Vol. 1, p. 105, ed.: Ph. Stevens, Eur. Fuel Cell Forum, Oberrohrdorf, Switzerland (1998)
53. S. Taniguchi, M. Kadowaki, T. Yasuo, Y. Akiyama, Y. Miyake, K. Nishio, *Denki Kagaku* 65 (1997) 574
54. H. P. Buchkremer, U. Diekmann, L. G. J. de Haart, H. Kabs, D. Stöver, I. C. Vinke, in: Proc. 3rd Eur. SOFC Forum, Nantes, France, Vol. 1, p. 143, ed.: Ph. Stevens, Eur. Fuel Cell Forum, Oberrohrdorf, Switzerland (1998)
55. Th. Malkow, U. v. d. Crone, A. M. Laptev, T. Koppitz, U. Breuer, W. J. Quadakkers, in: Proc. 5th Int. Symp. Solid Oxide Fuel Cells (SOFC-V), Aachen, Germany, p. 1245, eds.: U.

Stimming, S. C. Singhal, H. Tagawa, W. Lehnert, The Electrochemical Society, Pennington, NJ (1997)
56. D. Dulieu, J. Cotton, H. Greiner, K. Honegger, A. Scholten, M. Christie, T. Seguelong, in: Proc. 3rd Eur. SOFC Forum, Nantes, France, Vol. 1, p. 447, ed.: Ph. Stevens, Eur. Fuel Cell Forum, Oberrohrdorf, Switzerland (1998)
57. W. J. Quadakkers, T. Malkow, J. Pirón-Abellán, U. Flesch, V. Shemet, L. Singheiser, in: Proc. 4th Eur. SOFC Forum, Lucerne, Switzerland, Vol. 2, p. 827, ed.: A. McEvoy, Eur. Fuel Cell Forum, Oberrohrdorf, Switzerland (2000)
58. J. Pirón-Abellán, V. Shemet, F. Tietz, L. Singheiser, W.J. Quadakkers, A. Gil, in: Proc. 7th Int. Symp. Solid Oxide Fuel Cells (SOFC-VII), Tsukuba, Japan, p. 811, eds.: H. Yokokawa, S. C. Singhal, The Electrochemical Society, Pennington, NJ (2001)
59. O. Teller, W. A. Meulenberg, F. Tietz, E. Wessel, W. J. Quadakkers, in: Proc. 7th Int. Symp. Solid Oxide Fuel Cells (SOFC-VII), Tsukuba, Japan, p. 895, eds.: H. Yokokawa, S. C. Singhal, The Electrochemical Society, Pennington, NJ (2001)
60. Ch. Gindorf, K. Hilpert, L. Singheiser, in: Proc. 7th Int. Symp. Solid Oxide Fuel Cells (SOFC-VII), Tsukuba, Japan, p. 793, eds.: H. Yokokawa, S. C. Singhal, The Electrochemical Society, Pennington, NJ (2001)
61. M. Ueda, H. Taimatsu, in: Proc. 4th Eur. SOFC Forum, Lucerne, Switzerland, Vol. 2, p. 837, ed.: A. McEvoy, Eur. Fuel Cell Forum, Oberrohrdorf, Switzerland (2000)
62. K. Honegger, A. Plas, R. Diethelm, W. Glatz, in: Proc. 7th Int. Symp. Solid Oxide Fuel Cells (SOFC-VII), Tsukuba, Japan, p. 803, eds.: H. Yokokawa, S. C. Singhal, The Electrochemical Society, Pennington, NJ (2001)
63. N. Q. Minh, R. Doshi, J. Guan, S. Huss, G. Lear, K. Montgomery, E. Ong, in: Proc. 2000 Fuel Cell Seminar, Portland, Oregon, p. 593 (2000), eds.: Fuel Cell Seminar Organizing Committee
64. W. A. Meulenberg, O. Teller, U. Flesch, H. P. Buchkremer, D. Stöver, *J. Mater. Sci.* 36 (2001) 3189
65. J. P. Allen, in: Proc. 2000 Fuel Cell Seminar, Portland, Oregon, p. 55 (2000), eds.: Fuel Cell Seminar Organizing Committee
66. T. Iwata, N. Kadokawa, S. Takenoiri, in: Proc. 4th Int. Symp. Solid Oxide Fuel Cells (SOFC-IV), Yokohama, Japan, p. 110, eds.: M. Dokiya, O. Yamamoto, H. Tagawa, S. C. Singhal, The Electrochemical Society, Pennington, NJ (1995)
67. T. Shiomitsu, T. Kadowaki, T. Ogawa, T. Maruyama, in: Proc. 4th Int. Symp. Solid Oxide Fuel Cells (SOFC-IV), Yokohama, Japan, p. 850, eds.: M. Dokiya, O. Yamamoto, H. Tagawa, S. C. Singhal, The Electrochemical Society, Pennington, NJ (1995)
68. S. Linderoth, P. V. Hendriksen, M. Mogensen, N. Langvad, *J. Mater. Sci.* 31 (1996) 5077
69. D. M. England, A. V. Virkar, *J. Electrochem. Soc.* 146 (1999) 3196
70. D. M. England, A. V. Virkar, *J. Electrochem. Soc.* 148 (2001) A330
71. K. Föger, R. Donelson, R. Ratnaraj, in: Proc. 6th Int. Symp. Solid Oxide Fuel Cells (SOFC-VI), Honolulu, Hawaii, p. 95, eds.: S. C. Singhal, M. Dokiya, The Electrochemical Society, Pennington, NJ (1999)
72. K. Ahmed, J. Love, R. Ratnaraj, in: Proc. 7th Int. Symp. Solid Oxide Fuel Cells (SOFC-VII), Tsukuba, Japan, p. 904, eds.: H. Yokokawa, S. C. Singhal, The Electrochemical Society, Pennington, NJ (2001)

73. D. H. Peck, M. Miller, H. Nickel, D. Das, K. Hilpert, in: Proc. 4th Int. Symp. Solid Oxide Fuel Cells (SOFC-IV), Yokohama, Japan, p. 858, eds.: M. Dokiya, O. Yamamoto, H. Tagawa, S. C. Singhal, The Electrochemical Society, Pennington, NJ (1995)
74. Ch. Gindorf, L. Singheiser, K. Hilpert, M. Schroeder, M. Martin, H. Greiner, F. Richter, in: Proc. 6th Int. Symp. Solid Oxide Fuel Cells (SOFC-VI), Honolulu, Hawaii, p. 774, eds.: S. C. Singhal, M. Dokiya, The Electrochemical Society, Pennington, NJ (1999)
75. Y. Matsuzaki, M. Hishinuma, I. Yasuda, , in: Proc. 6th Int. Symp. Solid Oxide Fuel Cells (SOFC-VI), Honolulu, Hawaii, p. 981, eds.: S. C. Singhal, M. Dokiya, The Electrochemical Society, Pennington, NJ (1999)
76. S. P. S. Badwal, R. Deller, K. Föger, Y. Ramprakash, J. P. Zhang, *Solid State Ionics* 99 (1997) 297
77. S. P. Jiang, J. P. Zhang, L. Apateanu, K. Föger, *J. Electrochem. Soc.* 147 (2000) 4013
78. R. Ruckdäschel, R. Henne, G. Schiller, H. Greiner, in: Proc. 5th Int. Symp. Solid Oxide Fuel Cells (SOFC-V), Aachen, Germany, p. 1273, eds.: U. Stimming, S. C. Singhal, H. Tagawa, W. Lehnert, The Electrochemical Society, Pennington, NJ (1997)
79. A. Plas, E. Batawi, W. Straub, K. Honegger, R. Diethelm, in: Proc. 4th Eur. SOFC Forum, Lucerne, Switzerland, Vol. 2, p. 889, ed.: A. McEvoy, Eur. Fuel Cell Forum, Oberrohrdorf, Switzerland (2000)
80. R. Diethelm, M. Schmidt, K. Honegger, E. Batawi, in: Proc. 6th Int. Symp. Solid Oxide Fuel Cells (SOFC-VI), Honolulu, Hawaii, p. 60, eds.: S. C. Singhal, M. Dokiya, The Electrochemical Society, Pennington, NJ (1999)
81. Ch. Gindorf, L. Singheiser, K. Hilpert, *Steel Research* 72 (2001) 528
82. Y. Matsuzaki, I. Yasuda, *J. Electrochem. Soc.* 148 (2001) A126
83. A. Petric, P. Huang, F. Tietz, *Solid State Ionics* 135 (2000) 719
84. F. Tietz, *Ionics* 5 (1999) 129
85. D. Stolten, R. Späh, R. Schamm, in: Proc. 5th Int. Symp. Solid Oxide Fuel Cells (SOFC-V), Aachen, Germany, p. 88, eds.: U. Stimming, S. C. Singhal, H. Tagawa, W. Lehnert, The Electrochemical Society, Pennington, NJ (1997)
86. Y. Sakaki, Y. Esaki, M. Hattori, H. Miyamoto, T. Satake, F. Nanjo, T. Matsudaira, K. Takenubo, in: Proc. 5th Int. Symp. Solid Oxide Fuel Cells (SOFC-V), Aachen, Germany, p. 61, eds.: U. Stimming, S. C. Singhal, H. Tagawa, W. Lehnert, The Electrochemical Society, Pennington, NJ (1997)
87. W. J. Quadakkers, H. Greiner, M. Hänsel, A. Pattanaik, A. S. Khanna, W. Malléner, *Solid State Ionics* 91 (1996) 55
88. Y. Larring, T. Norby, *J. Electrochem. Soc.* 147 (2000) 3251
89. I. Arul Raj, F. Tietz, A. Gupta, W. Jungen, D. Stöver, *Acta Materialia*, 49 (2001) 1987
90. P. Y. Hou, K. Huang, W. T. Bakker, in: Proc. 6th Int. Symp. Solid Oxide Fuel Cells (SOFC-VI), Honolulu, Hawaii, p. 737, eds.: S. C. Singhal, M. Dokiya, The Electrochemical Society, Pennington, NJ (1999)
91. Y. Yamazaki, T. Namikawa, T. Ide, H. Kabumoto, N. Oishi, T. Motoki, T. Yamazaki, in: Proc. 5th Int. Symp. Solid Oxide Fuel Cells (SOFC-V), Aachen, Germany, p. 1291, eds.: U. Stimming, S. C. Singhal, H. Tagawa, W. Lehnert, The Electrochemical Society, Pennington, NJ (1997)
92. D. Stöver, U. Diekmann, U. Flesch, H. Kabs, W. J. Quadakkers, F. Tietz, I. C. Vinke, in: Proc. 6th Int. Symp. Solid Oxide Fuel Cells (SOFC-VI), Honolulu, USA, p. 812, eds.: S. C. Singhal, M. Dokiya, The Electrochemical Society, Pennington, NJ (1999)

Appendix E

Lattice Defects in Nanocrystalline CeO_2 Thin Films
I. Kosacki, T. Suzuki, V. Petrovsky, H.U. Anderson, and P. Colomban
Radiation Effects & Defects in Solids, Vol. 156, pp. 109-115

Radiation Effects & Defects in Solids, Vol. 156, pp. 109–115
Reprints available directly from the publisher
Photocopying permitted by license only

LATTICE DEFECTS IN NANOCRYSTALLINE CeO_2 THIN FILMS

I. KOSACKI[a,*], T. SUZUKI[a], V PETROVSKY[a], H. U. ANDERSON[a] and P. COLOMBAN[b]

[a]*Electronic Materials Applied Research Center, University of Missouri-Rolla 303 MRC, Rolla MO 65401, USA;* [b]*LADIR, UMR 7075 CNRS & Universite Pierre et Marie Curie 2 rue Henry Dunant, 94230 Thiais, France*

(Received 7 April 2000; In final form 7 August 2000)

The results of Raman scattering studies of nanocrystalline CeO_2 thin films are presented. The spectra have been described using the spatial correlation model from which the coherence length has been determined as a function of grain size. A direct comparison between the concentration of defects related to coherence length and microstructure of CeO_2 has been achieved.

Keywords: Ceria; Nanomaterials; Raman scattering; Thin films; Nonstoichiometry

1. INTRODUCTION

CeO_2 is an exceptionally important technological ceramic with a variety of applications including oxygen sensors, fuel cells and ionic membranes. Its electrical properties are strongly related to the microstructure such that an enhancement of about 4 orders of magnitude in electronic conductivity was observed when the microstructure changed from the micro- to nanocrystalline region [1–3]. This effect is probably attributed to extended interfacial area and reduced enthalpy of defect formation [3, 4]. Since the physical properties of nanocrystalline materials are dominated by the grain boundary phase, it is very important to understand and clarify its

* Corresponding author. E-mail: ikosacki@umr.edu

nature. Raman spectroscopy, which yields the information about the interaction between the ions can be very helpful in this study.

In this paper the results of a study of the dynamical properties of nanocrystalline CeO_2 thin films by Raman spectroscopy are presented. The objective of this study was to determine the crystalline quality of CeO_2 thin films by the analysis of Raman spectra and compare them with the grain size. A relationship between the lattice defects determined from Raman spectroscopy and microstructure of CeO_2 has been found.

2. EXPERIMENTAL

Dense nanocrystalline CeO_2 thin films were prepared on sapphire substrates using a polymeric precursor spin coating technique reported in detail elsewhere [3–5]. This process allows the preparation of the oxides from a precursor, which can be converted to dense oxide films by spin coating the precursor onto a dense substrate, followed by drying and crystallizing the resulting film at temperatures in the range of 300–1200°C. The microstructure of the films are characterized by very uniform distributions of grains whose size ranges from 4 to 300 nm depending upon the annealing temperature [3, 4].

The Raman spectra were recorded at room temperature using a Dilor XY spectrograph equipped with Spex CCD detector (2000×800 pixels). The spectra were recorded in microconfiguration with laser impact of $\sim 1\ \mu m$ diameter. The excitation source was the 514.5 nm line of an argon laser at the power level of 5.4 mW.

3. RESULTS AND DISCUSSION

Figure 1 presents the Raman spectra of nanocrystalline CeO_2 thin films compared to that from a single crystal. The Raman-active mode in this material corresponds to the frequency of $\omega_R = 466\ cm^{-1}$, which is attributed to a symmetrical stretching mode of a CeO8 vibrational unit. Therefore, this mode should be very sensitive to any disorder in the oxygen sublattice resulting from thermal and/or grain size induced non-stoichiometry. The influence of the microstructure of CeO_2 on the shape of Raman spectrum

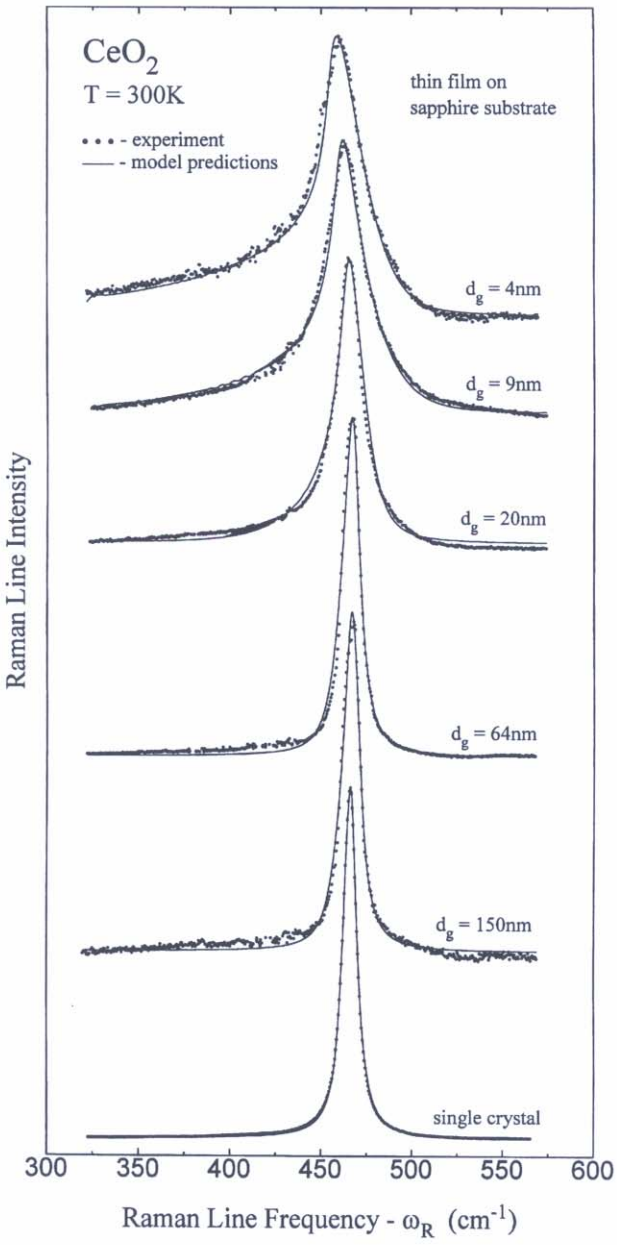

FIGURE 1 Raman spectra of single crystal, and nanocrystalline CeO_2 together with the fitted curve according to the spatial correlation model (Eq. 1, solid line).

was observed by the broadening of the line and increases in its asymmetry is attributed to reduction of phonon life-time in the nanocrystalline regime [3, 6, 7].

Important information regarding the lattice disorder can be obtained from the analysis of the shape of Raman line, which has been performed using a spatial correlation model [7, 8]. According to this model, The Raman line intensity, $I(\omega)$ at the frequency, ω can be written as:

$$I(\omega) = \int_0^1 \exp\left(\frac{-q^2L^2}{4}\right) \cdot \frac{d^3q}{[\omega - \omega(q)]^2 + \left(\frac{\Gamma_o}{2}\right)^2} \tag{1}$$

where q is the wave vector expressed in units of $2\pi/a$ (a is the lattice constant). Γ_o is the half width of the Raman line. The expression of $\exp(-q^2L^2/4)$ represents a Gaussian spatial correlation function with parameter L as the coherence length, $\omega(q)$ is the function of Raman phonon dispersion. This function has been determined for CeO_2 based on a rigid-model calculation [6] and was used in this analysis.

Figure 1 shows the Raman spectra for different grain sized CeO_2 and the corresponding line-shape fit performed using the spatial correlation model, (Eq. 1). As can be seen this model correlates well with the experimental data when the microstructure of CeO_2 is changed from single crystal to the nanometer range. Note that this procedure used only one fitting parameter, which is the phonon coherence length. Therefore, the disorder induced by the microstructure could be well defined by the coherence length rather then the half width or line asymmetry. Figure 2a presents the relationship between the so determined coherence length and the grain size of CeO_2 specimens. As can be seen, the coherence length is not microstructure dependent for the grain size larger than 100 nm and equals 10.5 nm. This value corresponds to the 20 lattice constants. The observed independence between the correlation length and grain size illustrates the limit above which the line broadening and asymmetry are not detectable. Note that for the specimens with grain size larger than 150 nm the Raman line is practically the same as that of a single crystal (Fig. 1). When the grain size is smaller than 100 nm, the coherence length decreases rapidly and equals 1.1 nm for a 4 nm grain sized specimen, which corresponds to 2 lattice constants. Such large changes in the coherence

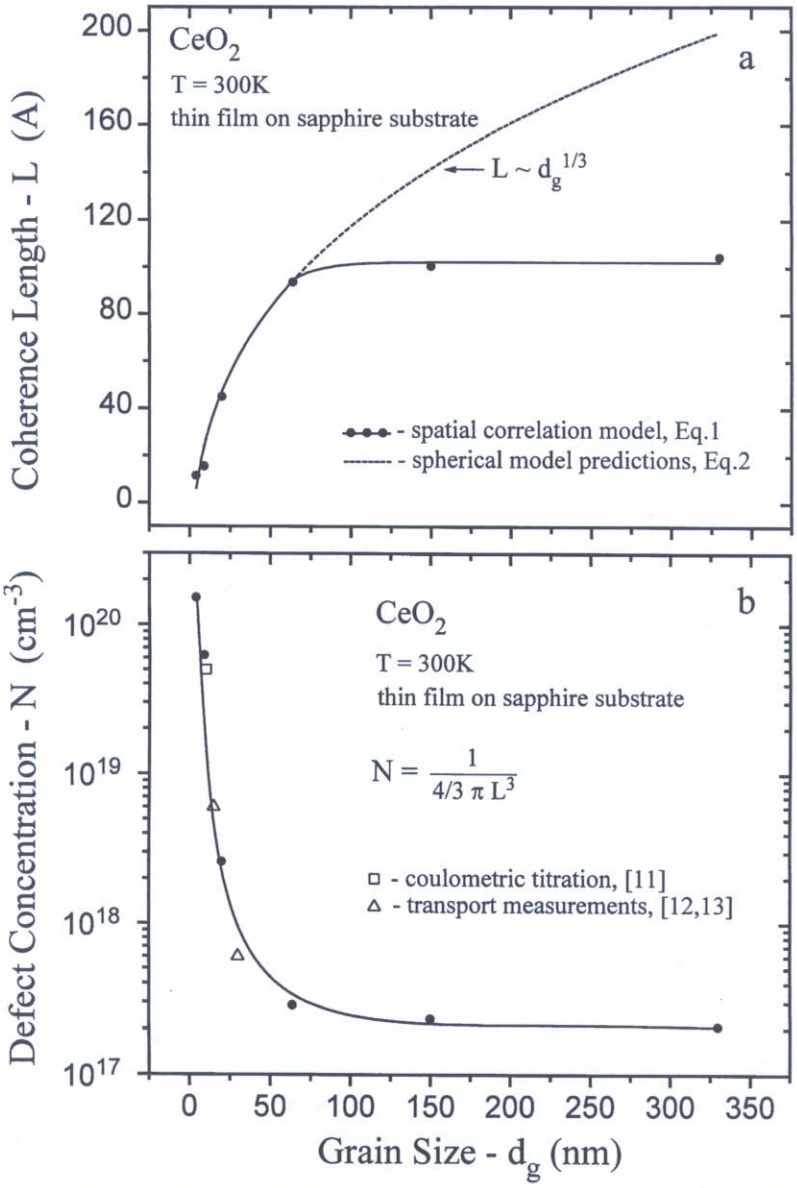

FIGURE 2 The coherence length (a), and related defect concentration (b) as a function of the grain size of nanocrystalline CeO_2 thin films.

length can be attributed to the grain boundary phase whose volume increases with decreasing grain size. The observed decrease in the coherence length was described in the model in which the fraction of atoms on the surface of each grain was considered. Assuming spherical symmetry of the grains and molecules, the relationship between the coherence length and the grain size can be determined [9]:

$$L = \sqrt[3]{\left(\frac{\alpha^2}{2d_g}\right) \cdot \left[(d_g - 2\alpha)^3 + 4{d_g}^2\alpha\right]} \tag{2}$$

where, α is the radius of CeO_2 molecule, which has been estimated from universal constants to be 0.34 nm. Note that for material with the grain size much larger then molecule radius ($d_g \gg \alpha$), the coherence length will depend upon the 1/3 power of the grain size $-L \sim d_g^{1/3}$. The coherence length determination in this way has been compared with the results obtained from the analysis of the Raman spectra and both are presented in Figure 2a as a function of grain size. As can be seen, the coherence length obtained from the spatial correlation model (Eq. 1) correlates well with predictions described by the spherical model (Eq. 2) in the range of the grain size smaller than 100 nm. This observation coincides with the changes of the fraction of grain boundary volume which sharply increase from 1 to 30% when grain size is reduced from 100 to 5 nm and illustrated the transition of the material into size-dependent region where physical properties are controlled by microstructure [9, 10].

Since the correlation length is dependent upon the grain size, it is possible that the changes of correlation length are attributed to the oxygen vacancies. Figure 2b presents the defect concentration calculated from the correlation length $-3/4\pi L^3$ as a function of grain size. As can be seen this concentration changes ca. 3 orders of magnitude from 10^{17} to 10^{20} cm^{-3} which corresponds to the same changes of oxygen vacancy concentration which were determined from the study of coulometric titration (10 nm) [11] and electrical conductivity measurements for 15 nm [12], and 30 nm [4, 13] grain sized specimens.

The good correlation between the defects determined from Raman spectra and conductivity measurements show that the changes in coherence length are related to the concentration of oxygen vacancies which increases

due to a reduction in their enthalpy of formation when the grain size decreases to the nanocrystalline regime.

4. CONCLUSIONS

The results of the study of nanocrystalline CeO_2 by Raman spectroscopy are presented and correlated with microstructure. The influence of the microstructure on the Raman spectra has been observed by an increase of asymmetry and half width of the Raman line, when the grain size decreased into the nanocrystalline range. The Raman spectra have been described using the spatial correlation model from which the correlation length has been determined and correlated with the concentration of defects in the grain boundary volume.

References

[1] Chiang, Y.M., Lavik, E.B., Kosacki, I., Tuller, H.L. and Ying, J.Y. (1996). *Appl. Phys. Lett.*, **69**, 185.
[2] Kosacki, I., Suzuki, T. and Anderson, H.U., *Electrochemical Society Proceedings*, **99–13**, (The Electrochemical Society Inc., Pennington NJ, 1999) pp.190–198.
[3] Kosacki, I. and Anderson, H.U. (2000). *Ionics* **6**, 1294.
[4] Kosacki, I., Suzuki, T. and Anderson, H.U. (2000). *Solid State Ionics* **136–137**, 1225.
[5] Chen, C.C., Anderson, H.U. and Nasrallah, M.M. (Feb. 1996). U.S. Patent No.5,494,700.
[6] Weber, W.H., Hass, K.C. and McBride, J.R. (1993). *Phys. Rev.*, **B48**,178.
[7] Parayanthal, P. and Pollak, F.H. (1984). *Phys. Rev. Lett.*, **52**, 1822.
[8] Fisher, A., Anthony, L. and Compaan, A.D. (1998) *Appl. Phys. Lett.* 72, 20, 2559.
[9] Kosacki, I., Suzuki, T., Anderson, H.U. and Colomban, Ph. (2001) *J. Am. Ceram. Soc.* **84**(9), in print.
[10] Sigel, R.W. In: *Materials Interfaces*, eds. D. Wolf and S. Yip, (Chapman and Hall, London 1992) pp. 341–460.
[11] Porat, O., Tuller, H.L., Lavik, E.B. and Chiang, Y.M., *M.R.S. Symposium Proceedings*, vol. **457**, (Materials Research Society, Pittsburgh PA, 1997) pp.99–103.
[12] Hwang, J.H. and Mason, T.O. (1998). *Z. Phys.Chem.*, **207**, 21.
[13] Kosacki, I. and Anderson, H.U. *M.R.S. Symposium Proceedings*, **453**, (Materials Research Society, Pittsburgh PA, 1997) pp. 537–542.

Appendix F

Grain Boundary Effects in Nanocrystalline Mixed Conducting Films

I. Kosacki, and H.U. Anderson

Encyclopedia of Materials – Elsevier, 2001

Grain Boundary Effects in Nanocrystalline Mixed Conducting Films

Nanostructured materials, including clusters, multilayers, ultrafine-grained films, and nanocrystalline bulk specimens, have become a very active research field in the area of solid-state ionics and materials engineering. A number of studies have shown that nanocrystalline materials are characterized by unique and improved optical, electronic, mechanical, and chemical properties that may lead to potentially useful technological applications (Alivisatos 1995, Gleiter 1989, Hadijpanayis and Siegel 1994, Siegel 1994). This is exciting both from the scientific and the technological point of view owing to the possibility of engineering the physical properties by controlling and varying the size of constituent domains and the manner in which they are assembled.

The unique properties of nanocrystalline materials are determined by the three fundamental features present in these materials: domain (grain) size spatially confined to less than 100 nm, significant number of grain boundaries which typically is about $10^{19}\,cm^{-3}$, and different composition of domain and grain boundaries. Since the volume of grain boundary phase depends upon microstructure, it is possible to obtain a material whose electrical transport is determined by interfaces and grain boundaries. In this case, owing to extended surface areas and higher diffusivity, the chemical kinetics of such materials should be enhanced compared with conventional microcrystalline specimens (Gleiter 1989, Siegel 1994). These possibilities have created a new challenge for solid-state ionic materials and may have an impact on a number of applications where high electrical conductivity (ionic or mixed) and the interaction between the solid and ambient atmosphere are the most important aspect, such as ionic and mixed conductors for batteries, fuel cells, gas sensors, and ionic membranes (Kosacki and Anderson 1998, Siegel and Hahn 1987, Tuller 1997).

However, for the development of such devices the stabilization of their microstructure is required. A number of studies have shown that this objective can be achieved by obtaining nanocrystalline thin films using the preparation techniques that allow the formation of dense specimens at reduced processing temperatures.

A wide variety of methods exist for the synthesis of nanocrystalline materials. They include molecular beam epitaxy, chemical vapor deposition, plasma spray, and evaporation and consolidation of ultrafine powders. The characteristics of nanocrystalline materials depend strongly on the method of preparation owing to different atomic arrangement in boundaries. In general, materials prepared from ultrafine powder, whether prepared by gas condensation or chemical methods, appear to differ significantly from those produced by atomic or molecular deposition techniques (Gleiter 1989, Hadijpanayis and Siegel 1994).

The key of nanocrystalline materials is the ability to significantly improve the electrical properties and phase stability by the understanding of the nanostructure/property relationship and how this might be controlled. These aspects are discussed using as examples results obtained from studies of $SrCeO_3$:Yb, ZrO_2:16%Y, and CeO_2 thin films prepared by the polymeric precursor spin coating technique which has proved to be particularly useful for the formation of dense nanocrystalline films with very uniform microstructures that are stable up to 1000°C.

1. *Processing and Microstructure*

The polymeric precursor spin coating method was developed by Anderson and co-workers (Anderson *et al.* 1996) and applied for the fabrication of oxide thin films. This technique allows the preparation of dense oxide films from organic precursors that can be converted to oxides by spin coating, drying, and annealing at temperatures in the range 300–1000°C. Such low temperatures compared to those typically required by powder processing (1400–1800°C) result in the formation of dense, nanocrystalline specimens with very uniform grain size distribution owing to the nucleation that occurs on the molecular level. Another advantage related to low processing temperatures is the ability to minimize interdiffusion effects between the film and substrate or between films with different composition. By controlling the precursor viscosity, spin rate, and annealing temperature, dense ZrO_2:16%Y, $SrCeO_3$:Yb, and CeO_2 films with thickness ranging from 20 nm to 1000 nm and grain size in the range 2–400 nm range can be prepared (Kosacki and Anderson 1996, 1997a, 1997b, Kosacki *et al.* 1999a, 1999d, 1999e).

Figure 1 shows a transmission electron microscopy (TEM) image of nanocrystalline ZrO_2:16%Y sintered at 400°C on a sapphire substrate, which is a typical example of a film prepared using the polymer precursor process. As can be seen the film is dense with an average grain size of 4 nm. Note that the microstructure of resulting films is related to the sintering temperature and can be varied: in the case of ZrO_2:16%Y from 1 nm to 400 nm for specimens $\sim 1\,\mu m$ thick. The crystallization and grain growth can be observed by x-ray diffraction. Figure 2 shows example x-ray spectra obtained for ZrO_2:16%Y films sintered at different temperatures. It is observed that crystallization occurs at temperatures below 400°C yielding single-phase material. The inset of Fig. 2 shows the relationship between grain size and sintering temperature. The uniform distribution of grains as well as the ability to control the thickness and microstructure of the films illustrate the advantage of the polymeric precursor method and allows a com-

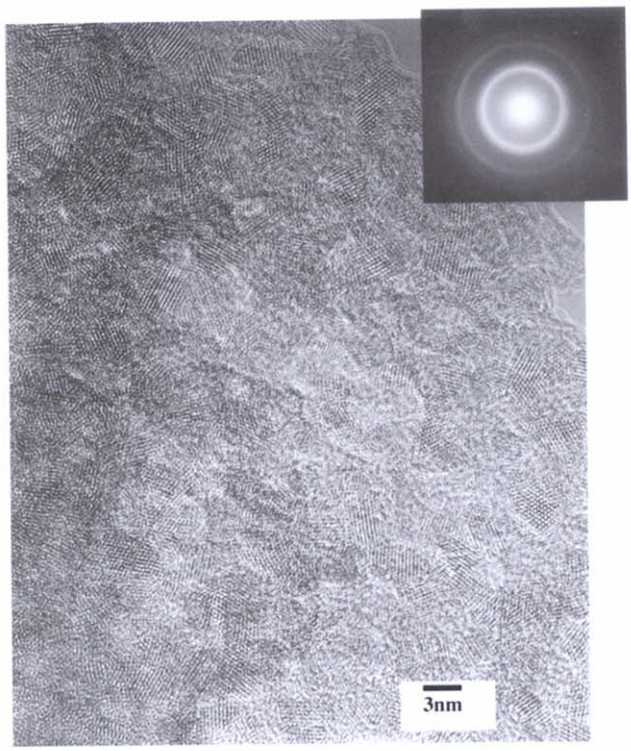

Figure 1
High-resolution TEM image of ZrO_2:16%Y thin film sintered at 400°C for 4h in air. The inset shows the diffraction pattern.

prehensivestudyofthestructure/propertyrelationships of nanocrystalline films.

2. *Electrical Conductivity*

Impedance spectroscopy is a very useful technique for the study of electrical transport in ceramic materials. This technique allows the separation of resistances related to grains, grain boundaries, and electrode effects because they each have different relaxation times that results in a separate semicircle in the impedance spectra. While the contribution of grain boundary area is controlled by the microstructure, it is possible to reach the grain size in which conductivity can be dominated by the interface and grain boundary phases. Such an effect has been considered by Siegel (1993, 1994) and experimentally observed by Kosacki and Anderson (1996, 1997a, 1997b). An example of the extent of the importance of the grain boundary phase is shown in Fig. 3 where the impedance spectra of a nanocrystalline $SrCeO_3$:Yb thin film and microcrystalline specimens are compared. As can be seen, distinctly different spectra are observed for the nano- and microcrystalline structures. The impedance spectra of the microcrystalline specimens exhibit three well-defined semicircles at high, intermediate, and low frequency that are attributed to bulk, grain boundary, and electrode resistances, respectively, while the nanocrystalline thin films show only two semicircles. The low-frequency semicircles are identified as related to the solid/electrode interface and can be also determined from two- and four-probe d.c. conductivity measurements (Kosacki and Anderson 1997a).

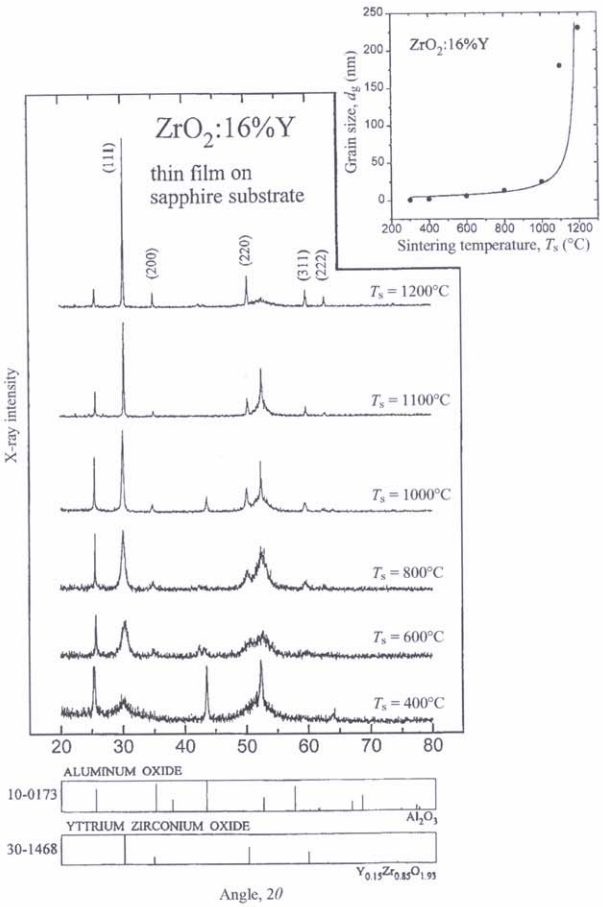

Figure 2
X-ray diffraction patterns of ZrO_2:16%Y thin films deposited on monocrystalline sapphire substrate sintered at different temperatures. The inset shows the dependence of grain size on sintering temperature.

The analysis of the temperature dependence of high-frequency conductivities for nano- and microcrystalline specimens shows that they have different origin, which is manifested by about three orders of magnitude higher conductivity, and higher activation energy for the nanocrystalline material (Kosacki and Anderson 1996, 1997a, 1997b). The comparison of the specific grain boundary conductivity, which is the conductivity normalized to a single grain boundary, determined from the intermediate-frequency semicircle for microcrystalline $SrCeO_3$:5%Yb and the conductivity related to the high-frequency semicircle for nanocrystalline specimens is shown in the inset of Fig. 3. As can be seen, there is a good correlation between the activation energies, which strongly suggests that the high-frequency semicircle for nanocrystalline specimens is dominated by the grain boundary contribution. Additional evidence for such an

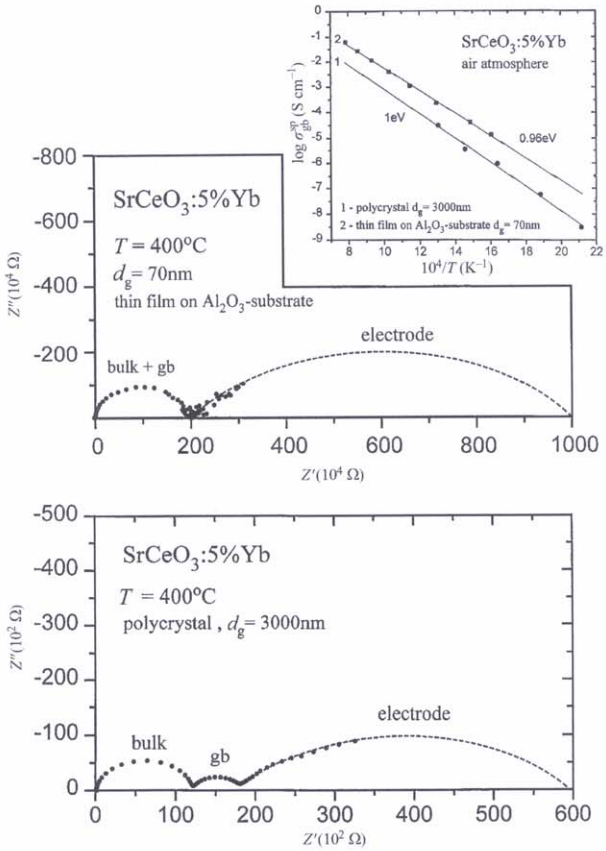

Figure 3
Comparison of the impedance spectra of $SeCe_{0.95}Yb_{0.05}O_3$ nanocrystalline thin film and microcrystalline bulk specimen. The inset shows the temperature dependence of specific grain boundary conductivity.

interpretation can be obtained from the analysis of the capacitance related to the bulk and grain boundaries for microcrystalline specimens and compared with the capacitance determined from the high-frequency semicircle of nanocrystalline materials, which yield the same values of the dielectric constant (Kosacki *et al.* 1998).

The differences in the values of the specific grain boundary conductivities determined for nano- and microcrystalline $SrCeO_3$:Yb (Fig. 3) are probably because of the size-dependent grain boundary impurity segregation effect that has been reported for ZrO_2:Ca (Aoki *et al.* 1996). A decrease in the concentration of silicon and calcium impurities has been observed in the grain boundaries owing to an increase in the grain boundary area as the grain size is decreased.

In recognition of the influence of the microstructure on electrical transport, a direct comparison between the electrical conductivity of single-crystal, micro- and nanocrystalline ZrO_2:16%Y was made by Kosacki *et al.* (1998). The results of this study are shown in Fig. 4.

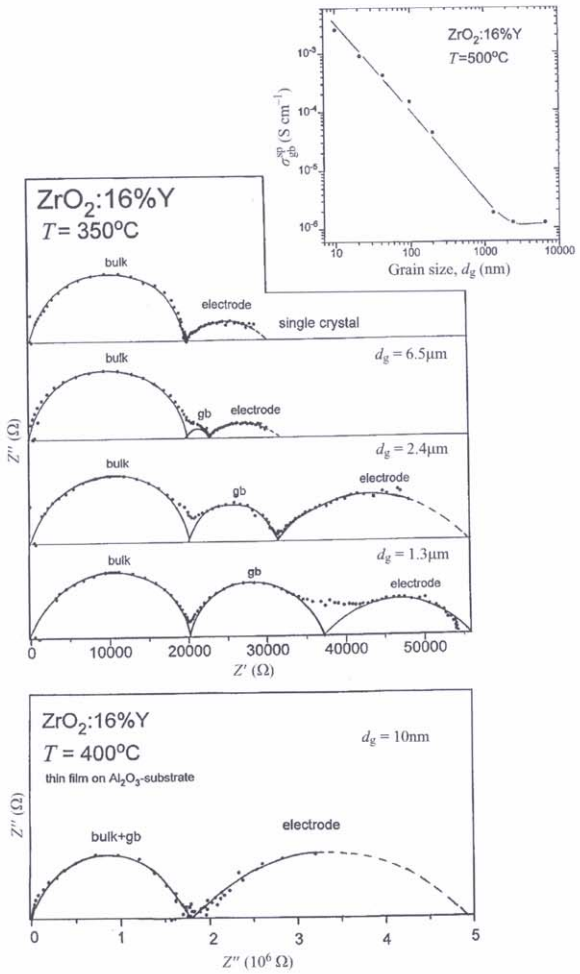

Figure 4
Comparison of the impedance spectra of single-crystal, bulk microcrystalline specimens and nanocrystalline thin films of ZrO_2:16%Y. The insert shows the specific grain boundary conductivity as a function of grain size.

As can be seen from the impedance data, the contribution of the grain boundary to the total resistance significantly increases when the grain size decreases below 2μm. The inset of Fig. 4 shows the specific grain boundary conductivity determined for ZrO_2:16%Y specimens as a function of grain size. The conductivity is microstructure independent for large grain size (> 2μm) and sharply increases by as much as three orders of magnitude when the grain size approaches 10nm. This effect illustrates the importance of the

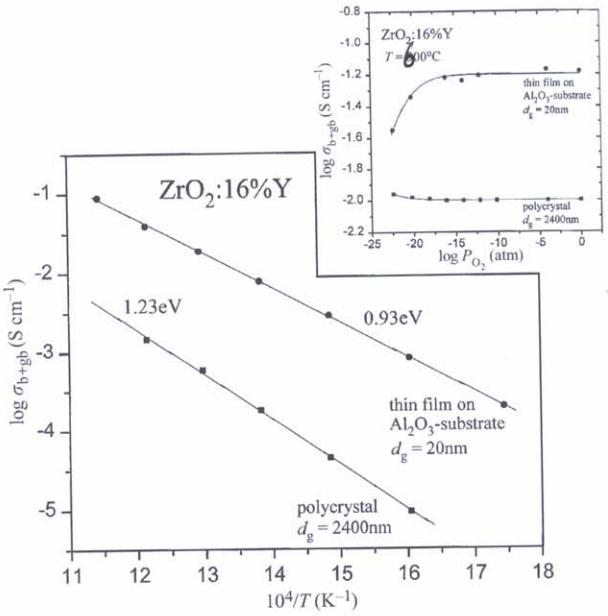

Figure 5
Temperature dependence of electrical conductivity of ZrO_2:16%Y nanocrystalline thin film and microcrystalline bulk specimens. The inset shows the electrical conductivity as a function of oxygen activity.

grain boundaries whose properties are size dependent in the nanocrystalline regime.

Since the electrical properties of nanocrystalline materials are dominated by the grain boundary phase, a very important question is what is the influence of the grain boundaries on the macroscopic electrical conductivity? It is expected that the grain boundary segregation effect should tend to enhance the electrical conductivity owing to a lowering of the impurity concentration and higher diffusion in the grain boundary compared to the bulk area. This behavior has been observed for the ionic conductivity in AgCl (Maier 1995), in CeO_2 (Kosacki and Anderson 1997b), and in ZrO_2:16%Y (Kosacki *et al.* 1999b) thin films. Figure 5 shows the temperature dependence of the conductivity calculated from impedance spectra for nanocrystalline ZrO_2:16%Y (superposition of the bulk and grain boundary) and that obtained from similar data for microcrystalline specimens. As can be seen, the nanocrystalline material exhibits about two orders of magnitude increase in the conductivity when the grain size is changed from 2.4μm to 20nm. This enhancement is a result of a decrease in the activation energy from 1.23eV to 0.93eV when the grain size is changed from 2.4μm to 20nm, respectively.

The inset of Fig. 5 illustrates another interesting behavior of nanocrystalline ZrO_2:16%Y. This shows the results obtained from the measurements of the electrical conductivity as a function of oxygen activity at 900°C. For a microcrystalline specimen the conductivity is P_{O2}-independent, which is typical for extrinsic ionic conductivity with the concentration of ionic species controlled by acceptors, while for a nanocrystalline specimen an anomalous decrease in the low P_{O2} region has been observed (Kosacki *et al.* 1999b). This behavior appears to be related to a decrease in carrier concentration, which in turn depends on defect pair formation and quantum confinement in the nanocrystalline specimens (Kosacki *et al.* 1999a, 1999c).

ZrO_2:16%Y is an example of a material in which the microstructure can alter the ionic conductivity owing to changes in the ion mobility. Cerium oxide is an example of a material in which the microstructure can also influence the electronic conductivity, but in this case it is electronic owing to reduction of the enthalpy

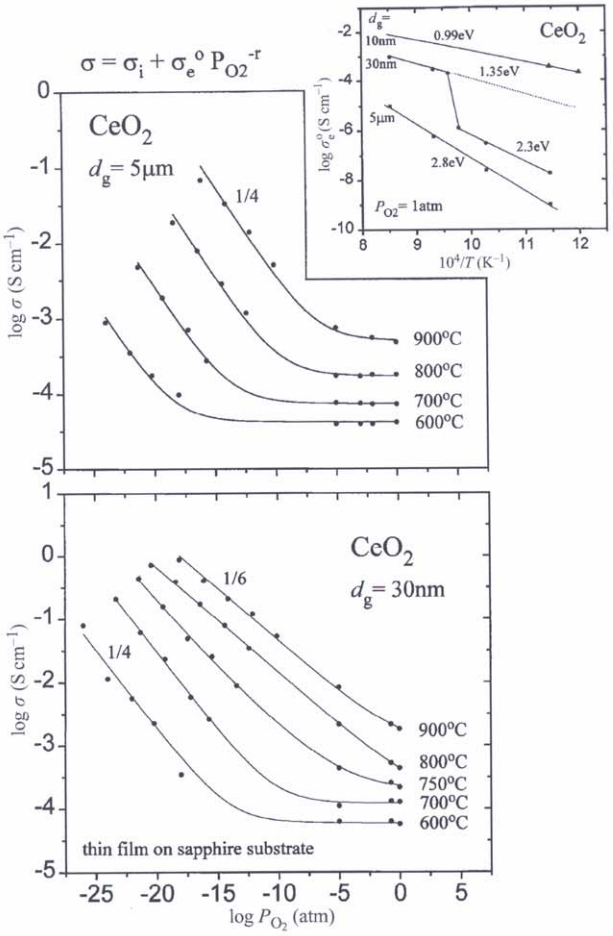

Figure 6
Electrical conductivity as a function of oxygen activity for CeO_2 specimens with different microstructure. The inset shows the temperature dependence of the electronic conductivity determined for CeO_2 with different grain size.

of oxygen vacancy formation. This effect has been reported by Chiang *et al.* (1996, 1997) for CeO_2 by showing the transition from ionic to electronic conductivity when microstructure changes from 5μm to 10nm.

Kosacki *et al.* (1999e, 1999f) studied the non-stoichiometry of CeO_2 as a function of microstructure. The electrical conductivity of microcrystalline CeO_2 shows at high oxygen activity a P_{O2}-independent region characteristic of extrinsic ionic conductivity, while at low P_{O2}, extrinsic electronic conductivity is observed (Fig. 6). A similar behavior has been

observed for a 30 nm grained specimen; however, at temperatures higher than 800 °C the electronic conductivity shows a transition from extrinsic to intrinsic, which is manifested in the change of the P_{O_2} dependence of the conductivity. The analysis of the temperature dependence of the conductivity provides an opportunity to separate the electronic and ionic parts of the conductivity and correlate them with material microstructure. The results show that only the electronic conductivity is microstructure dependent and an increase over six orders of magnitude (at 600 °C) is observed when the grain size changes from 5 μm to 10 nm (inset of Fig. 6), while the ionic conductivity changes by a factor of only 1.5 with the same activation energy. This behavior is striking and is related to the reduction in the oxygen vacancy formation energy, which is determined from the conductivity activation energy. Assuming that the polaron hopping energy does not change with grain size, the oxygen vacancy formation energy is calculated to decrease from 4.7 eV to 1.8 eV as the grain size decreases from 5 μm to 10 nm. Such a large reduction in the enthalpy implies greater nonstoichiometry in the nanocrystalline specimens, which is consistent with the measurement of higher electron conductivity.

3. *Summary*

The objective of this article is to illustrate the relationship between electrical transport and microstructure in nanocrystalline oxide thin films. The properties of these materials are extremely dependent upon the concentration of impurities, grain boundaries, and the number of atoms within the grain boundary area. Examples are given that illustrate enhancement of both the ionic and electronic conductivity in nanocrystalline materials. In particular the size-dependent effects related to impurity segregation, defect thermodynamics, and material nonstoichiometry are highlighted. The study of nanocrystalline oxide thin films is just at its beginning and the knowledge of the relationships between their properties and processing parameters seems to be a key to the understanding of the nature of these materials, and consequently to the realization of their full impact on solid-state ionics.

Bibliography

Alivisatos A P 1995 Semiconductor nanocrystals. *MRS Bull.* **20** (8), 23–32

Anderson H U, Chen C C, Nasrallah M M 1996 Method of coating a substrate with a metal oxide film from an aqueous solution comprising a metal cation and polymerizable organic solvent. *US Pat* 5 494 700

Aoki M, Chiang Y M, Kosacki I, Lee L J, Tuller H L, Liy Y 1996 Solute segregation and grain-boundary impedance in high-purity stabilized zirconia. *J. Am. Ceram. Soc.* **79** (5), 1169–80

Chiang Y M, Lavik E B, Kosacki I, Tuller H L, Ying J Y 1996 Defect and transport properties of nanocrystalline CeO_{2-x}. *Appl. Phys. Lett.* **69** (2), 185–7

Chiang Y M, Lavik E B, Kosacki I, Tuller H L, Ying J Y 1997 Nonstoichiometry and electrical conductivity of nanocrystalline CeO_{2-x}. *J. Electroceramics* **1** (1), 7–14

Gleiter H 1989 Nanocrystalline materials. *Prog. Mater. Sci.* **33**. 223–315

Hadjipanayis G C, Siegel R W 1994 *Nanophase Materials, Synthesis, Properties, Applications*. Kluwer, Dordrecht, The Netherlands

Kosacki I, Anderson H U 1996 The transport properties of nanocrystalline $SrCe_{0.95}Yb_{0.05}O_3$ thin films. *Appl. Phys. Lett.* **69** (27), 4171–3

Kosacki I, Anderson H U 1997a The structure and electrical properties of $SrCe0._{95}Yb_{0.05}O_3$ thin film protonic conductors. *Solid State Ionics* **97**, 429–36

Kosacki I, Anderson H U 1997b Electrical conductivity and structure of nanocrystalline CeO_2 thin films. In: Davies P K, Jacobson A J, Torardi Ch C, Venderah T A (eds.) *MRS Symp. Proc.* **453**, pp. 537–42

Kosacki I, Anderson H U 1998 Nanostructured oxide thin films for gas sensors. *Sensors Actuators* **B48**, 263–9

Kosacki I, Gorman B, Anderson H U 1998 Microstructure and electrical conductivity in nanocrystalline oxide thin films. In: Ramanarayanan T A (ed.) *Ionic and Mixed Conducting Ceramics*. Electrochemical Society, Pennington, NJ, Vol. 97-24, pp. 631–42

Kosacki I, Petrovsky V, Anderson H U 1999a Band gap energy in nanocrystalline ZrO_2:16%Y thin films. *Appl. Phys. Lett.* **74** (3), 341–3

Kosacki I, Petrovsky V, Anderson H U 1999b Electrical conductivity in nanocrystalline ZrO_2:Y. In: Nazri A, Julien Ch (eds.) *MRS Symp. Proc.* **548**

Kosacki I, Petrovsky V, Anderson H. U 1999c Modeling and characterization of electrical transport in oxygen conducting solid electrolytes. *J. Electroceramics*

Kosacki I, Suzuki T, Anderson H U 1999d The growth and optical properties of ZrO_2:16%Y and CeO_2 nanocrystalline thin films. *Proc. 101st Annual Meeting*. American Ceramic Society, Indianapolis, IN

Kosacki I, Suzuki T, Anderson H U 1999e Nanocrystalline oxide thin films for electrochemical devices. *Proc. 195th Meeting*. Electrochemical Society, Seattle, WA

Kosacki I, Suzuki T, Anderson H U 1999f Electrical conductivity of nanocrystalline ceria and zirconia thin films. *Solid State Ionics*

Maier J 1995 Composite electrolytes. *Mater. Chem. Phys.* **17** (5), 485–98

Siegel R W 1993 Exploring mesoscopia: the bold new world of nanostructures. *Phys. Today* (Oct.), 64–8

Siegel R W 1994 Nanophase materials. In: Trigg G L (ed.) *Encyclopedia of Applied Physics*. VSH, New York, Vol. 11, pp. 173–200

Siegel R W, Hahn H 1987 Nanophase materials. In: Yussouff M (ed.) *Current Trends in the Physics of Materials*. World Scientific, Singapore, pp. 403–19

Tuller H L 1997 Solid state electrochemical systems—opportunities for nanofabricated or nanostructured materials. *J. Electroceramics* **1** (3), 211–18

I. Kosacki and H. U. Anderson

Appendix G

Optical Properties of Undoped and Gd-doped CeO2 Nanocrystalline Thin Films
T. Suzuki, I. Kosacki, V. Petrovsky, and H.U. Anderson
Journal of Applied Physics, Vol. 91, No. 4, February 15, 2002

Optical properties of undoped and Gd-doped CeO_2 nanocrystalline thin films

Toshio Suzuki,[a] Igor Kosacki, Vladimir Petrovsky, and Harlan U. Anderson
Electronic Materials Applied Research Center, University of Missouri-Rolla, Rolla, Missouri 65401

(Received 6 April 2001; accepted for publication 6 November 2001)

The results of studies of the preparation, structure, and optical properties of undoped and Gd-doped CeO_2 thin films are presented. Dense films with 4–150 nm grain size have been obtained on monocrystalline sapphire substrates using a polymeric precursor spin coating method. The results of the optical measurements are presented and correlated with the microstructure of the films. The transmission spectra have been used to determine the energy dependence of the refractive index, n and the extinction coefficient, k. Both n and k of the thin films decreased as grain size decreased and these results showed that this change could be related to the transition from crystalline to amorphous CeO_2. The effect of dopant has little influence on n, $<5\%$, but doping resulted in about a 30%–40% reduction of k compared to undoped specimens, which could be related to the decrease of absorption centers due to the replacement of Ce by Gd. © *2002 American Institute of Physics.*
[DOI: 10.1063/1.1430890]

I. INTRODUCTION

Cerium based oxides have been of interest because of their relatively high electrical conductivity, chemical stability, efficiency for absorbing UV radiation, and transmission in the visible and infrared regions. Many studies have been made of the optical properties of CeO_2 thin films by using optical transmission or reflectance spectroscopy.[1–3] Guo *et al.* investigated the optical and structural properties of cerium oxide thin films obtained by rf magnetron sputtering.[1] They investigated optical properties of highly oriented crystalline and amorphous CeO_2 thin films using variable angle spectroscopic ellipsometry (VASE) and reported that highly oriented crystalline specimens exhibited a higher refractive index and a higher band gap energy for both direct and indirect transition compared to amorphous specimens. Therefore, investigation of optical properties for nanocrystalline ceria with different grain size becomes more important to understand the optical behavior of crystalline and amorphous specimens.

Nanocrystalline materials have studied not only optical but also electrical properties since they have shown their enhanced characters which are not seen in microstrusture materials. One of the interesting phenomena regarding nanostructure is the quantum confinement effect.[4,5] This effect, which is well investigated for semiconductors, occurs when the crystal size approaches the spatial extent of an electron and/or hole, and results in shifts of the absorption edge to higher energy, in other words, increase of band gap energy. This behavior also observed for nanocrystalline ZrO_2:16%Y and CeO_2 thin films.[6,7] Recent studies have shown that nanocrystalline ceria have the electrical properties that differ from those observed for microcrystalline oxides, because of the increased surface area and grain boundary volume.[8–11] The electronic conductivity of nanocrystalline ceria is enhanced compared with microcrystalline ones

Thin film processing methods such as deposition methods and sol-gel technique have been utilized to synthesize nanocrystalline materials. Comparing consolidation and sintering of clusters, these methods are the low temperature of the methods, which can be a significant advantage. Among these methods, recent studies have shown that a polymer precursor spin coating technique,[12] which is the low temperature nanocrystalline thin film synthesis method, has turned out to be effective for a very stable precursor, low processing temperature $\geqslant 400\,^{\circ}C$ and yielding very dense and optical quality films. These features are enabled to control the grain size and to obtain stable microstructure, which is very important and makes it possible for the systematic study of microstructure-physical properties relationships, including optical and electrical properties. Application of nanocrystalline oxides is very wide and includes the electrochemical devices such as solid oxide fuel cell, ceramic oxygen generator, and partial oxidation membranes.

The purpose of this study was to investigate the influence of grain size on the optical absorption spectra and to relate the optical absorption properties of nanocrystalline and amorphous structures. In the present work, the results of transmission measurements and analysis of spectra to determine the refractive index and the extinction coefficient are presented and the influence of dopant and microstructure to the optical absorption properties including the band gap energy.

II. EXPERIMENT

A. Sample preparation

Nanocrystalline undoped and 20%Gd-doped CeO_2 thin films with a thickness of 0.3–0.4 μm have been obtained on sapphire single crystal substrates using a polymeric precursor spin coating process.[12] For this preparation, cerium nitrate,

[a]Electronic mail: toshio@umr.edu.

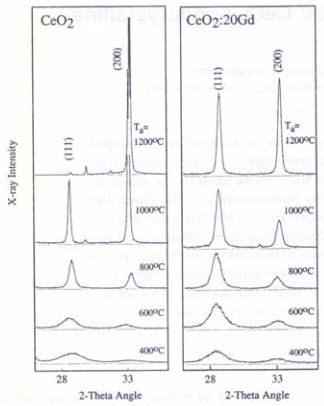

FIG. 1. X-ray diffraction patterns of undoped and Gd-doped CeO_2 thin films deposited on monocrystalline sapphire substrate annealed under different temperatures. Thickness of films ranged from 300 to 400 nm.

$Ce(NO_3)_3 \cdot 6H_2O$ and gadolinium nitrate, $Gd(NO_3)_3 \cdot 6H_2O$ for doped specimens were used as starting material. The appropriate concentrations of the cations were added to a solution containing water and ethylene glycol. A conventional spin coating technique was used to deposit the precursor on the substrate. By controlling the solution viscosity, the spin rate and annealing temperature, undoped and 20%Gd-doped CeO_2 films with variable thickness and microstructure were

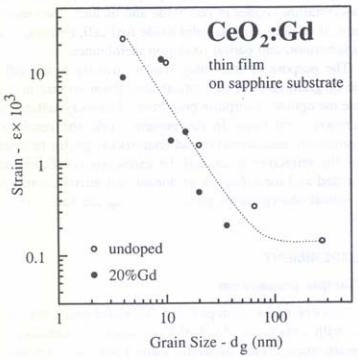

FIG. 2. Relationship between strain and grain size for undoped and Gd-doped CeO_2 thin films deposited on monocrystalline sapphire substrate. Film thickness = 300–400 nm.

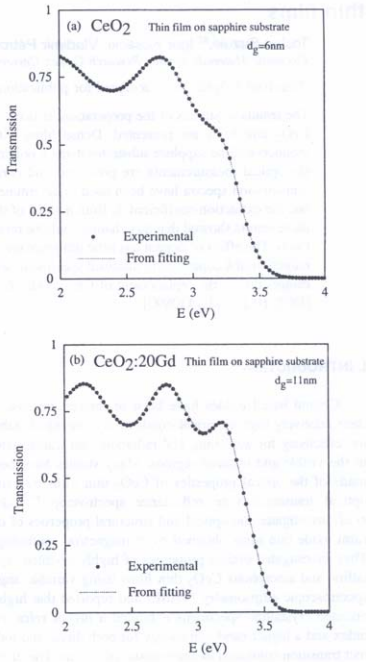

FIG. 3. Transmission spectra of (a) undoped and (b) Gd-doped CeO_2 thin films. The dash line was obtained by the curve fitting. Film thickness =300–400 nm.

prepared on the substrates. The undoped and 20%Gd-doped CeO_2 films were obtained by annealing the films for 4 hours over the temperature region of 350–1200 °C. These temperatures are low compared to those typically required by powder processing techniques (1400–1800 °C), but do allow the formation of dense, more than 90% of theoretical density, nanocrystalline specimens.

B. XRD characterization

The crystallization and grain growth of undoped and 20%Gd-doped CeO_2 films in the cubic phase were investigated using x-ray diffraction (XRD). X-ray diffraction data for thin film samples were collected using a SINTAG 2000 x-ray diffractometer operating with Cu $K\alpha 1$ radiation. A typical 2θ scan range of 20°–80° and a step size of 0.05°

were employed. The XRD spectra have been recorded in the offset configuration to reduce the signal from monocrystalline substrate [orientation (012)].

The analysis of the shape of each x-ray line has been used to determine the grain size for all specimens. Assuming that the line broadening ($\beta=\beta'+\beta''$) is the sum of the contributions attributed to the grain size(d_g) and the strain (ε), which can be written as $\beta'=1/(d_g\cos\theta)$ and $\beta''=4\varepsilon\tan\theta$, then the grain size and the strain can be determined from the linear relationship between $\beta\cos\theta$ and $4\sin\theta$, where θ is the Bragg diffraction angle. Note that the strain (ε) is defined as $\varepsilon=\Delta d/d$, where Δd is displacement of the lattice.[13]

C. Optical measurement

Undoped and 20%Gd-doped CeO_2 thin films were studied by optical transmission spectroscopy to determine the relationship between the optical related properties and the microstructure. The transmission spectra were obtained at room temperature with a Cary UV-visible spectrophotometer. Intensity of the transmission spectra can be described by the thickness of the film, the refractive index and extinction coefficient of thin film and substrate using Fresnel's equations.[14] The transmission spectra were fitted using these relations to determine the refractive index and extinction coefficient for different specimens.

III. RESULTS AND DISCUSSION

A. Microstructure of undoped and 20%Gd-doped CeO_2 thin films

Figure 1 shows the XRD spectra for the (111) and (200) diffraction lines for undoped and 20%Gd-doped CeO_2 specimens annealed at different temperatures.[15,16] Note that these are the parts of the spectra that are measured. The spectra show that the same crystal structures were obtained for both undoped and Gd-doped specimens, however the crystal growth in the (200) direction appears to be faster for the undoped specimens. It was observed that the grain size was as a function of the annealing temperature and the dopant level.[16] The doped films appeared to be about 20 nm after annealing at 1000 °C for 4 h, while that for the undoped was about 65 nm, which shows that the grain size of Gd-doped CeO_2 was substantially reduced compared to that of undoped specimens.[16]

Compared to the ionic radii of Ce^{4+} and Gd^{3+}, 1.11 and 1.19 Å (coordination number=8),[17] it can be predicted that Gd ions are most likely placed in Ce positions in the lattice. This can be confirmed by the x-ray diffraction lines, with the result that the peak positions for undoped and doped specimens do not change as shown in Fig. 1.

A strain versus grain size plot for undoped and Gd-doped CeO_2 thin films is shown in Fig. 2 which were determined from x-ray analysis. It is shown that smaller grain size specimens display higher strain for both undoped and doped specimens and no dopant effect on grain size–strain relation.

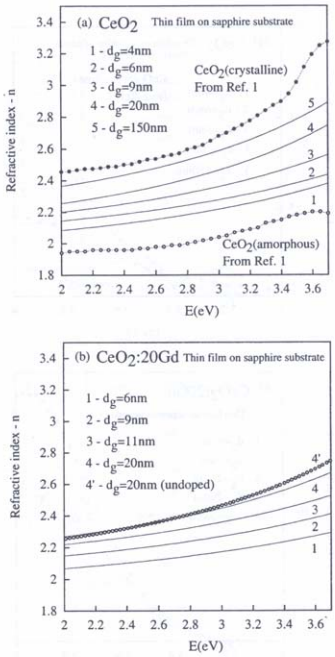

FIG. 4. The photon energy dependence refractive index of (a) undoped and (b) Gd-doped CeO_2 thin films with the reported values of crystalline and amorphous CeO_2. Film thickness = 300–400 nm.

B. Optical properties of undoped and 20%Gd-doped CeO_2 thin films

1. The refractive index and extinction coefficient of undoped and Gd-doped CeO_2 thin films

Figure 3 shows the transmission spectra of (a) undoped and (b) Gd-doped CeO_2 films with the line being calculated by a fitting procedure, where the refractive index and the extinction coefficient were determined. The results show that the experimental data were well reproduced by the calculated line. The thickness of films was obtained from this calculation and was found to range from 300 to 400 nm.

The energy dependence of the refractive index for undoped and 20%Gd-doped CeO_2 thin films is shown in Figs. 4(a) and 4(b) with the value of crystalline and amorphous CeO_2.[1] The refractive indices which were observed to decrease as the grain size decreased for both undoped and Gd-doped specimens appears to be due to density and/or the influence of the grain boundaries, since the refractive indices lie between those of crystalline and amorphous CeO_2. As

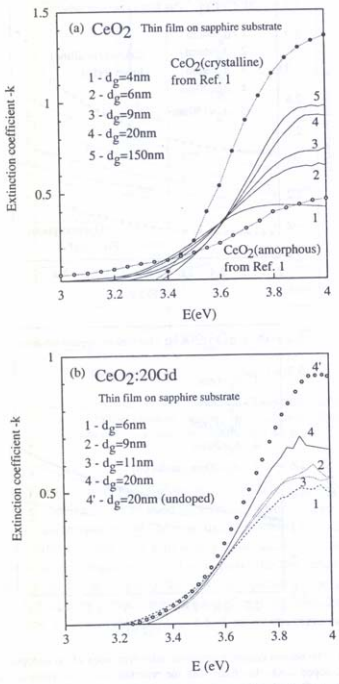

FIG. 5. Photon energy dependence extinction coefficient of (a) undoped and (b) 20%Gd-doped CeO_2 thin films with reported values. Film thickness = 300–400 nm.

shown in Fig. 4(b), the refractive index of both undoped and doped CeO_2 were same (within 5%), which shows almost no effect of the dopant on n. This is to be expected since the crystal structure and density at the undoped and doped specimens did not change with dopant additions. Similar results have also reported for Sn doped-CeO_2 (Ref. 11) and Y doped ZrO_2.[18]

The extinction coefficients as a function of photon energy for the undoped and Gd-doped CeO_2 films are shown in Figs. 5(a) and 5(b). For undoped specimens, it is shown that the shape of the k curve changes and decreases as grain size decreases to be close to the value seen for amorphous CeO_2.[1] For doped specimens, on the other hands, the value of k is decreased about 30%–40% compared to those of undoped specimens. These results could be explained by the assumption that the introduction of Gd results in a decrease in the

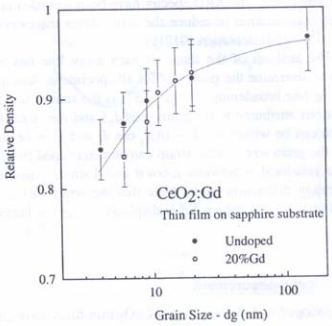

FIG. 6. Relative density for undoped and 20%Gd-doped CeO_2 thin films determined from the refractive index. Film thickness = 300–400 nm.

concentration of the absorption center (Ce–O–Ce) with dopant additions.

The relation between refractive index and the relative density of the specimens is given by,[19,20]

$$\frac{n_E^2-1}{n_E^2+2}=\frac{n^2-1}{n^2+2}\rho, \tag{1}$$

where n_E, n, and ρ are the effective refractive index, the refractive index of 100% dense material and the relative density of specimen, respectively. Taking n as the value of crystalline CeO_2 from literature[1] and n_E as the value of nanocrystalline specimens, the density of thin films can be obtained from Eq. (1) and shown in Fig. 6 as a function of grain size. The results showed the density of 87%±3.5%(undoped) and 84%±3.4%(Gd doped) for 6 nm grain size specimens. The relative density of the grain boundary region is reported to be about 60% of the crystalline[21] and assuming that the thickness of grain boundary is 1 nm, a 6 nm grain size specimen has about 27% of its volume as grain boundary. Therefore, the estimated density of 6 nm grain size specimen is about 89%, which is close to the value determined from optical measurements.

An attempt was made to treat the grain boundaries as being amorphous and to fit the k of the nanocrystalline specimens using the data for crystalline and amorphous specimens. This was, however, not successful which indicated that the grain boundary region could not be considered amorphous from the optical point of view.

2. Absorption coefficient and the band gap energy

The absorption coefficient, α can be calculated from the relation using k:[14]

$$\alpha=\frac{4\pi k}{\lambda}, \tag{2}$$

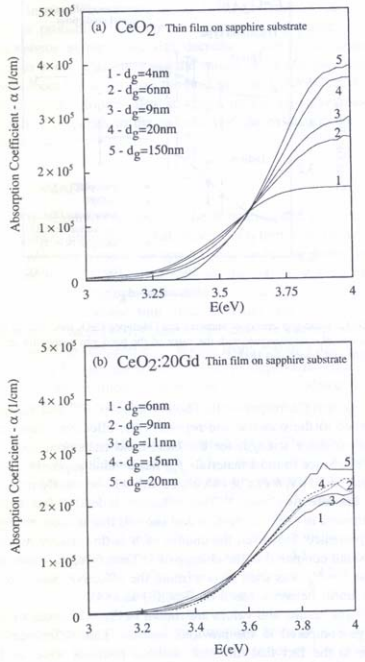

FIG. 7. Absorption coefficient, α as a function of photon energy for (a) undoped (b) 20%Gd-doped CeO_2 thin films with different grain size.

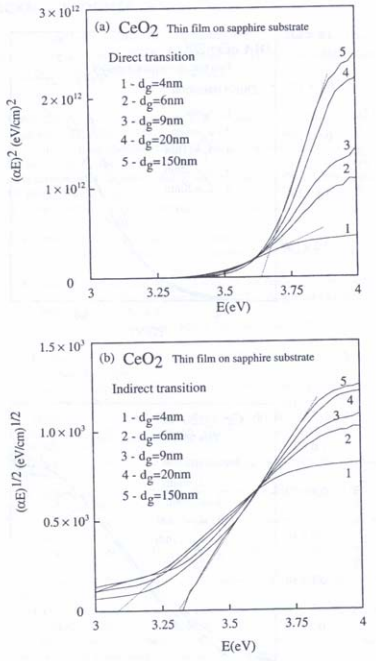

FIG. 8. Behavior of (a) $(\alpha E)^2$, (b) $(\alpha E)^{1/2}$ as a function of photon energy for CeO_2 thin films with different grain size.

where λ is the wavelength of incident light. The absorption coefficient of undoped and Gd-doped CeO_2 are shown in Fig. 7. The optical band gap energy, E_g was determined from the analysis of the absorption spectra, where a steep increase of the absorption is observed due to a band–band transition, from the general relation[1,3]

$$\alpha E = b(E - E_g)^{\eta}, \tag{3}$$

where E is the photon energy, and η is a constant with the value 1/2 for direct allowed transitions, and 2 for indirect allowed transitions. Figure 8 shows (a) direct and (b) indirect absorption of undoped specimens as a function of phonon energy. For both the direct and indirect transitions, E_g decreases as grain size decreases, where E_g is between the values reported for crystalline and amorphous specimens. The changes in band gap energy with a decreasing grain size are often correlated to quantum confinement which has been experimentally well established for semiconducting materials and theoretically understood.[4,5] For undoped CeO_2, we have reported that confinement effects occurred with grain size below 200 nm,[7] but E_g decreased for the grain size <50 nm. Similar results are also seen for direct and indirect absorption of Gd-doped specimens with grain size lower than 20 nm as shown in Figs. 9(a) and 9(b). Figure 10 shows the behavior of the band gap energy as a function of the grain size for undoped and 20%Gd-doped CeO_2 thin films determined from optical absorption spectra. As can be seen, the effect of dopant on the optical band gap energy is very small. The band gap energy determined for undoped 150 nm grain size was found to be 3.32 ± 0.10 eV for indirect transition, and 3.64 ± 0.11 eV for direct transition, which is consistent with previously reported results.[1,18] These values are close to values of the band gap energies found by Guo *et al.* 3.60 eV-(direct) and 3.30 eV(indirect) for crystalline and 3.55 eV(direct) and 2.96 eV(indirect) for amorphous.[1] The solid line in Fig. 10 shows the tendency of increasing band gap energy as a grain size decreasing to 50 nm grain size, which is possibly explained by quantum confinement effect (dashed line in Fig.

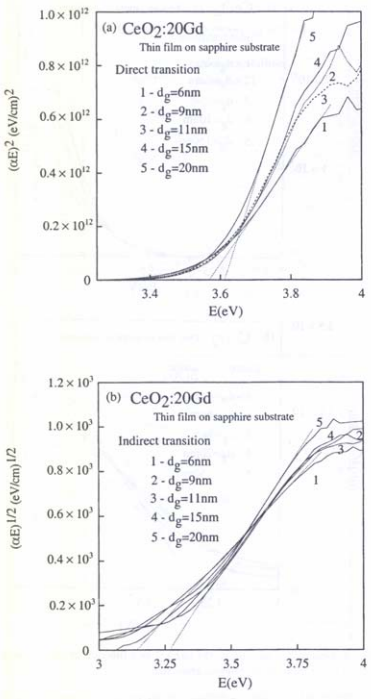

FIG. 9. Behavior of (a) $(\alpha E)^2$, (b) $(\alpha E)^{1/2}$ as a function of photon energy for Gd-doped CeO_2 thin films with different grain size.

10).[22] However, it is shown that the band gap energy decreased to be close to the value at amorphous specimens as the grain size decreased under 50 nm.

As can be seen in Figs. 8 and 9, not only was the band gap energy influenced by the grain size, but also the slopes of curves which are described by b in Eq. (3) also changed. Here, only the influence of microstructure on the slope of the absorption curve for direct transition will be considered, since the slope b of absorption curve for direct transition can explicitly be obtained. The parameter b for the direct transition is described as

$$b = \frac{e^2 m_0^{1/2}}{4\pi h^2 \epsilon c} \frac{1}{n} \left(\frac{2m_r^*}{m_0}\right)^{3/2} f_{cv}, \tag{4}$$

where e, m_0, h, ϵ, and c represent charge and mass of the electron, Planck constant, dielectric permittivity and the velocity of light, respectively. The constants of m_r^* and f_{cv} are related to the material and represent the effective mass and the oscillator strength for the band-band transition, respectively. Since in most materials f_{cv} has a value approximately equal to 20 eV, b can be calculated and will be mostly related to the effective mass.[23] The reflective index, n, has been estimated in previous section and showed that it had a energy dependence. However, the change of n at this energy region is small compared to the change of k. Therefore, the value of n at $E = E_g$ was used to determine the effective mass from the linear behavior based on Eqs. (3) and (4).

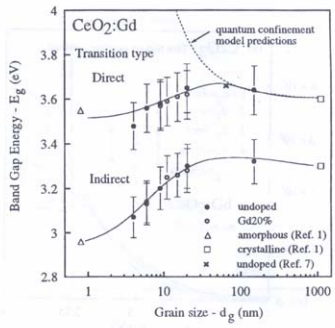

FIG. 10. Band-gap energy of undoped and Gd-doped CeO_2 thin films as the function of microstructure with the value of the band gap energy for crystalline and amorphous (Ref. 1).

The results and values are shown in Fig. 11 appear to be large compared to the previous results.[7] This difference is due to the fact that different analysis methods were used, however, the tendency of the effective mass appeared to be same. The effective mass decreases as grain size decreases,

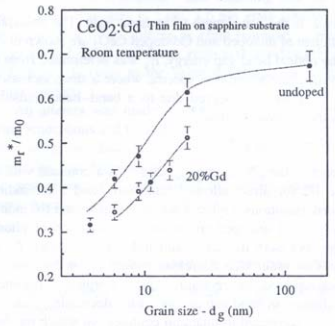

FIG. 11. Relationship between the effective mass and grain size of undoped and doped CeO_2 thin films determined from the slope of $(\alpha E)^2$ function.

which means the density of states is changed by the decrease in grain size. The change in the density of states with grain size is probably related to the specimens becoming more amorphous as the grain size decreased. The effect is also seen in doped specimens and the values of the effective mass were about 0.1 lower than those of undoped specimens. The effect of the dopant also appeared in the effective mass, which corresponds to the reduction of the extinction coefficient.

IV. SUMMARY

The results of a study of the formation and the microstructure of undoped and Gd-doped CeO_2 thin films obtained by a polymeric precursor spin coating technique have been presented. The preparation method allowed crystalline film formation temperatures to be decreased such that it was possible to obtain dense thin films with the grain size in the nanometer range (4–150 nm) on the sapphire substrates with the annealing temperatures ranging from 350 to 1200 °C.

Using Fresnel equations, the energy dependent refractive index, n and extinction coefficient, k were calculated from transmission spectra. Both the n and k of thin films decreased as grain size decreased which could be related to the transition from the crystalline to amorphous state. The addition of Gd had little influence on n ($<5\%$), but resulted in about a 30%–40% reduction of k, which can be related to a decrease in concentration of absorption centers (Ce–O–Ce) due to replacement of Ce by Gd. The behavior of the band gap energies determined from direct and indirect transition as a function of grain size was also determined and found to decrease for grain size <50 nm for both undoped and 20%Gd-doped CeO_2. From the optical property point of view, the grain boundary region could not be considered to be amorphous, however, it showed the transition from crystalline to amorphous with the decrease of grain size for optical related properties in CeO_2 thin films. Optical properties of nanocrystalline specimens showed systematic changes which suggest that their optical character can be controlled by microstructure.

ACKNOWLEDGMENTS

The authors would like to thank the Department of Energy, Contract No. DE-AC26-99FT40710 and Unitika Ltd. for financial support of this research.

[1] S. Guo, H. Arwin, S. N. Jacobsen, K. Järrendahl, and U. Helmersson, J. Appl. Phys. **77**, 5369 (1995).
[2] R. M. Bueno, J. M. Martinez-Duart, M. Hernandez-Velez, and L. Vazquez, J. Mater. Sci. **32**, 1861 (1997).
[3] A. Hartridge, M. G. Krishna, and K. Bhattacharya, J. Phys. Chem. Solids **59**, 859 (1998).
[4] M. I. Freedhoff and A. P. Marchetti, *Optical Properties* (CRC, New York, 1997), Vol. 2, pp. 1–30.
[5] L. E. Brus, J. Chem. Phys. **80**, 4403 (1984).
[6] I. Kosacki, V. Petrovsky, and H. U. Anderson, Appl. Phys. Lett. **74**, 341 (1999).
[7] I. Kosacki, T. Suzuki, and H. U. Anderson, in *Innovative Processing/Synthesis: Ceramics, Glasses, Composites III* (The American Ceramic Society, 2000), pp. 275–284.
[8] I. Kosacki and H. U. Anderson, Mater. Res. Soc. Symp. Proc. **453**, 537 (1997).
[9] Y. M. Chiang, E. B. Lavik, I. Kosacki, H. L. Tuller, and J. Y. Ying, J. Electroceram. **1**, 7 (1997).
[10] I. Kosacki, T. Suzuki, and H. U. Anderson, Proc. Meeting Electrochem. Soc., **99**, 190 (1999).
[11] Z. Crnjak Orel and B. Orel, Phys. Status Solidi B **186**, K33 (1994).
[12] H. U. Anderson, M. M. Nasrallah, and C. C. Chen, U.S. Patent No. 5,494,700 (1996).
[13] B. D. Cullity, *Elements of X-ray Diffraction* (Addison-Wesley Reading, MA, 1959).
[14] C. F. Bohren and D. R. Huffman, *Absorption and Scattering of Light by Small Particles* (Wiley, New York, 1983).
[15] T. Suzuki, I. Kosacki, H. U. Anderson, and P. Colomban, J. Am. Ceram. Soc. **84**, (2001).
[16] T. Suzuki, I. Kosacki, and H. U. Anderson, Electrochem. Soc. Proc. **32**, 190 (2000).
[17] M. W. Barsoum, *Fundamentals of Ceramics* (McGraw-Hill, New York, 1997).
[18] L. Mechin, A. Chabli, F. Bertin, M. Burdin, G. Rolland, C. Vannuffel, and J. C. Villegier, J. Appl. Phys. **84**, 4935 (1998).
[19] C. J. Brinker and G. W. Scherer, *Sol-Gel Science: The Physics and Chemistry of Sol-Gel Processing* (Academic, San Diego, CA, 1990).
[20] V. Petrovsky, H. U. Anderson, and T. Petrovsky, Mater. Res. Soc. Symp. Proc. **581**, 553 (2000).
[21] H. Gleiter, Mater. Sci. **33**, 223 (1989).
[22] I. Kosacki, T. Suzuki, and H. U. Anderson, Ceram. Trans. **108**, 275 (2000).
[23] P. Bhattacharya, *Semiconductor Optoelectronic Devices* (Prentice-Hall, Upper Saddle River, NJ, 1993).

Appendix H

Characterization of Low Temperature Cathodes for Solid Oxide Fuel Cells

Z. Byars, W. Huebner, and H.U. Anderson

Presentation at
The American Ceramic Society Meeting
St. Louis, MO, April 2002

Characterization of Low Temperature Cathodes for Solid Oxide Fuel Cells

Zach Byars*, Wayne Huebner
and Harlan U. Anderson

With thanks to:
Roger Smith, Amy Trujillo, Shi C. Zhang
and DOE

Department of Ceramic Engineering
University of Missouri – Rolla
Rolla, MO 65409

Outline

- Introduction
- Impedance Spectroscopy of Symmetric Cells
  - Processing / Testing geometry
  - Temperature dependence
  - pO_2 dependence
- Fuel Cell Testing
  - Processing / Test geometry
  - IV results
  - Comparison to symmetric cell results
- Conclusions

Introduction

- Currently there is a significant amount of research attempting to reduce the operating temperature of solid oxide fuel cells.
  - If the operating temperature can be lowered to below 800°C metals could be used as the interconnect reducing cost.
- In order to lower the operating temperature the catalytic activity of the electrodes needs to be increased.
- $La_{1-x}Sr_xCo_{1-y}Fe_yO_3$ (LSCF) is known to be more catalytic than LSM. However it reacts with the most common electrolyte yttrium stabilized zirconia (YSZ).
  - The A site cation (La and Sr) reacts to form a low conductivity pyrochlore phase.
- This study looks at different A site cations with two possible ionization states.
  - Hopefully, if the pyrochlore phase forms it will be conductive and not reduce the catalytic activity of the electrode.

Symmetric Cell Testing Geometry

- The Pechini process was used to make all cathode powders.
  - Each powder was milled, calcined and x-rayed to insure single phase.
- Tape cast yttrium stabilized zirconia (YSZ) was used as an electrolyte.
- The cathode powders were mixed with a binder and solvent system and painted onto both sides of the YSZ.
- The cathode powders were sintered at the temperatures shown below.
- Pt mesh was used as current collectors.

Cathode Composition	Acronym	Sintering Temp.
$La_{0.7}Sr_{0.2}MnO_3$	LSM	1200°C
$La_{0.8}Sr_{0.2}Co_{0.2}Fe_{0.8}O_3$	LSCF	1000°C
$Sm_{0.8}Sr_{0.2}Co_{0.2}Fe_{0.8}O_3$	SSCF	1000°C
$Pr_{0.8}Sr_{0.2}Co_{0.2}Fe_{0.8}O_3$	PSCF	1000°C

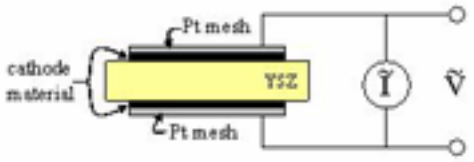

Symmetric Cell ASR Definition and Temperature Dependence

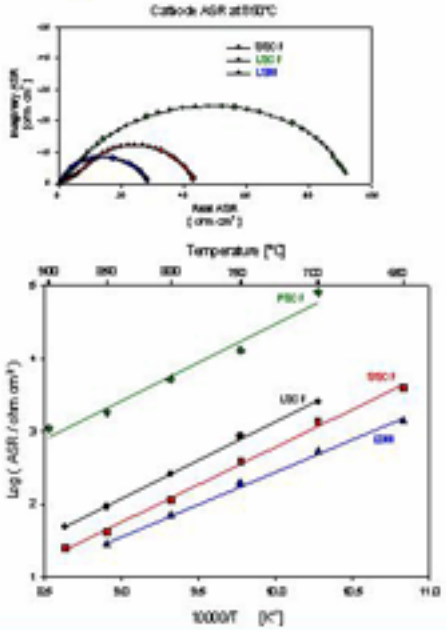

- Impedance spectroscopy was used to separate the electrode resistance from the bulk.
- In this study the electrode area specific resistance (ASR) is assumed to be given by:

$$ASR = \left(\begin{array}{l} \text{low freq. intercept} - \\ \text{high freq. intercept} \end{array} \right) \text{area}$$

Material	Activation Energy [eV]	Pre-exponential [ohm cm²]
LSM	1.8	3.6E-07
SSCF	2.0	3.0E-08
LSCF	2.1	3.3E-08
PSCF	2.1	8.7E-07

LSM and SSCF Electrode ASR vs. pO_2

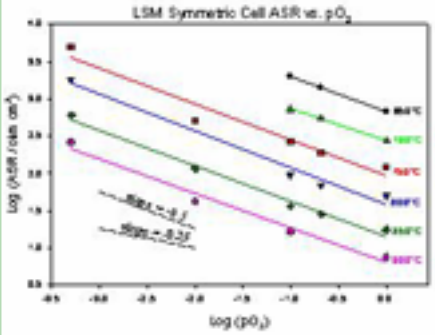

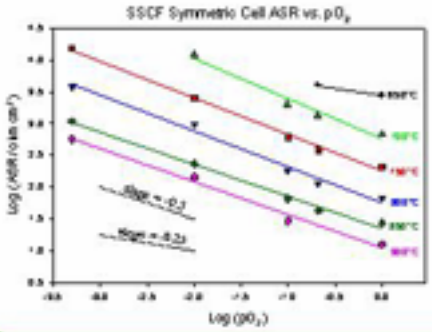

- The effects of changing the partial pressure of oxygen on the electrode ASR are shown to the left.
  - pO_2 was controlled by mixtures of oxygen and nitrogen.
- The symmetric cells were equilibrated in each gas for at least 10 hours before measurement.
- The cells were equilibrated at each temperature for at least 1.5 hours before measurement.
- Both LSM and SSCF show a pO_2 dependence of -½.

LSCF Electrode ASR vs. pO_2

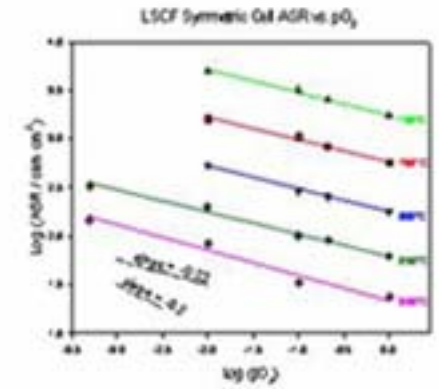

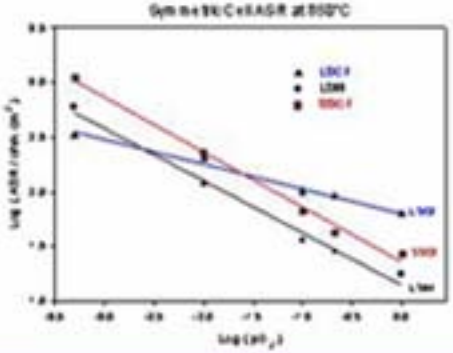

- LSCF shows a pO_2 dependence of -¼.
  - LSCF is not as strongly dependent on pO_2 as LSM and SSCF.
- Below a pO_2 of approximately 0.01 LSCF has a lower ASR than LSM and SSCF.
- Oxygen adsorption is predicted to have a pO_2 dependence of -½.
- A possible explanation is:
  - Oxygen adsorption is the dominate step in LSM and SSCF.
  - LSCF has a higher oxygen surface exchange coefficient and adsorption is no longer dominate.

Processing Technique for Producing Tape Cast Co-Fired Fuel Cells

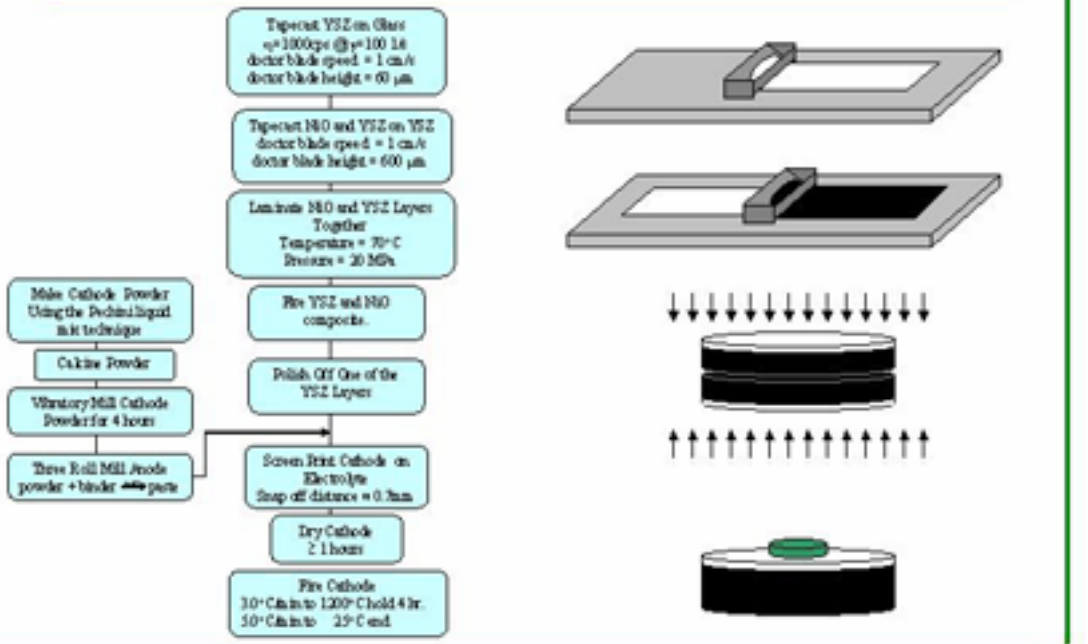

Anode Supported Electrodes

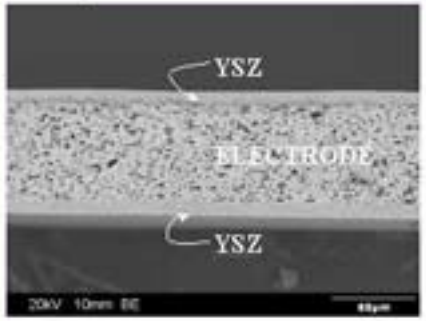

- Back Scattered image showing both sides of the composite, before polishing off one of the sides.
- By matching the shrinkage, and creating a symmetric composite the sample stays relatively flat after firing.

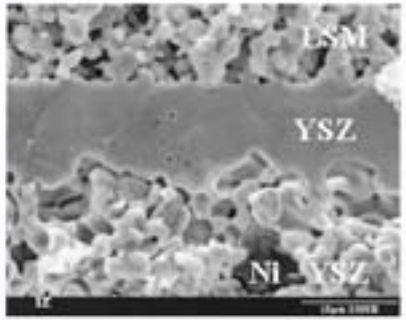

- Cross Section of a fuel cell
  - Porous LSM on top
  - Dense, 10μm thick, YSZ in the middle
  - Porous Ni - YSZ on bottom

Testing Geometry

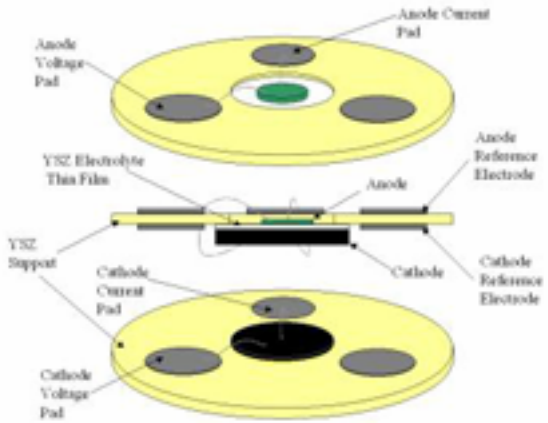

- 6 point conductivity measurements
- The reference electrodes are on the support which is also made of YSZ.
- The reference electrodes can be used to separate the anode and cathode losses.

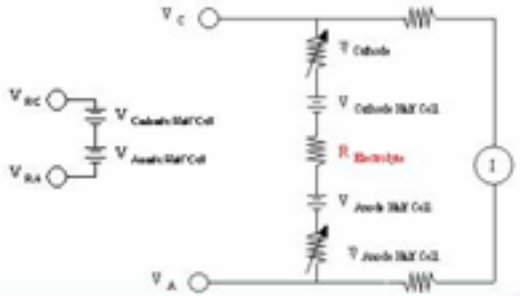

Electrical Results for Anode Supported Fuel Cells

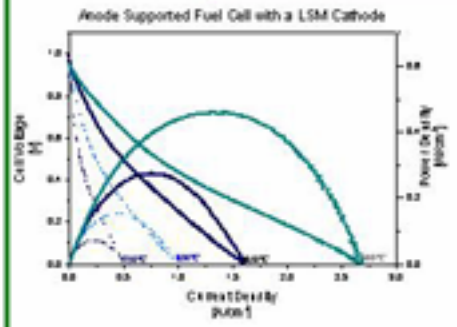

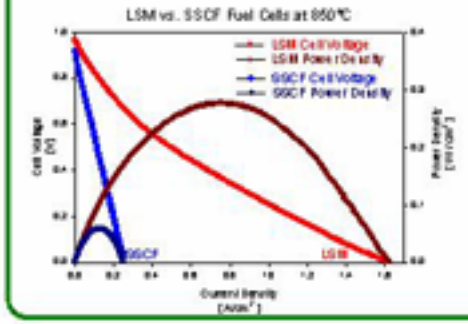

- Cell Design
  - Electrolyte - 10μm thick YSZ
  - Anode - 40 v% Ni, YSZ
    - Fired at 1450°C for 2 hours
  - Cathode –
    - LSM or SSCF
- Measurement Conditions
  - Fuel: 97% FG , 3% H_2O
  - Oxidant: Air
- LSM Cathode max. power density at 850°C = 300mW/cm^2
- SSCF Cathode max. power density at 850°C = 50mW/cm^2

Overpotentials for SSCF Cathodes vs. Temperature

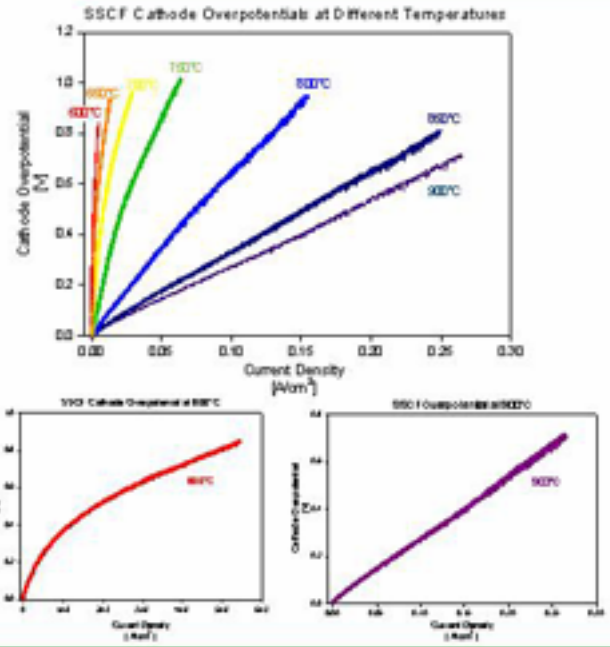

- By measuring the voltage difference from the reference electrodes and the cathode, overpotentials can be found.
- The cathodes "resistance" varies over two orders of magnitude from 600 to 900°C.
- At low temperatures the overpotential is nonlinear. As temperature is increased it becomes more linear.
- All curves can be described by a power law:

$$\eta = \eta_{\circ(T)} I^{a(T)}$$

Cathode Overpotentials at 850°C

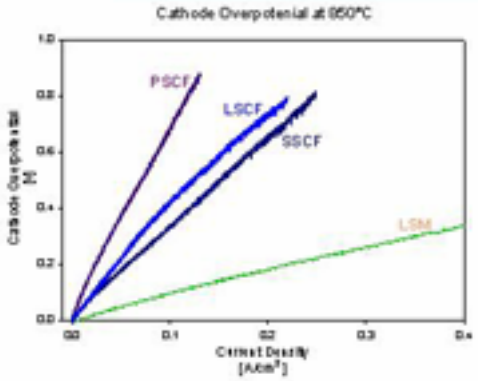

- As predicted by the symmetric cell results the cathodes grouped in order of low to high overpotential are:

  LSM < SSCF < LSCF < PSCF

- Impedance spectroscopy of symmetric cells does not predict the ratio of the overpotentials correctly.

Cathode Material	Symmetric Cell ASR at 850° C / Symmetric Cell LSM ASR at 850° C	Fuel Cell ASR at 850° C / Fuel Cell LSM ASR at 850° C
LSM	1	1
SSCF	1.5	4.0
LSCF	3.3	4.8
PSCF	64	8.6

Conclusions

- Symmetric Cells
  - The activation energy for all electrodes studied is approximately 2 eV.
  - LSM and SSCF have a pO2 dependence of -½.
  - LSCF has a pO2 dependence of -¼.
- Fuel Cell
  - LSM performs the best of all cathodes tested.
    - Approximately four time better than SSCF.
  - Electrode overpotential on thin film cells can be measured by a reference electrode not located on the cell.
  - At low temperature the cathode overpotentials were found to be nonlinear.
  - As the temperature was increased the overpotentials became linear.

Overpotentials for LSCF Cathodes vs. Temperature

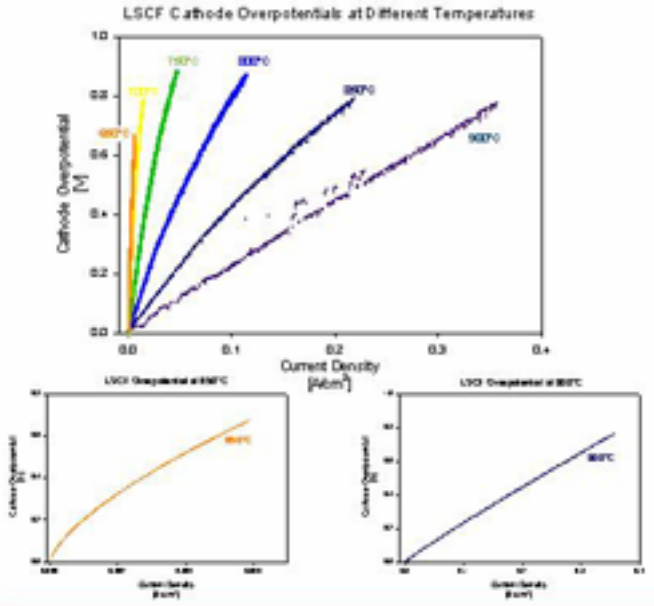

LSCF and SSCF Tafel Plots

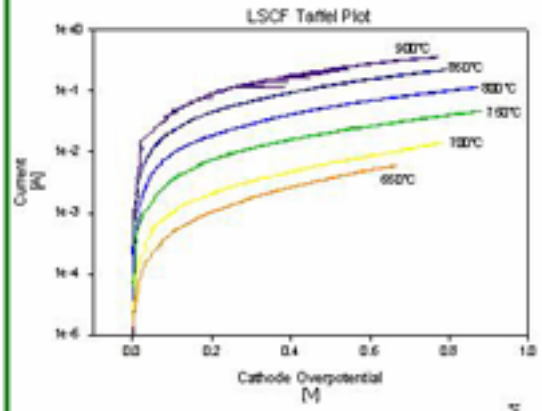

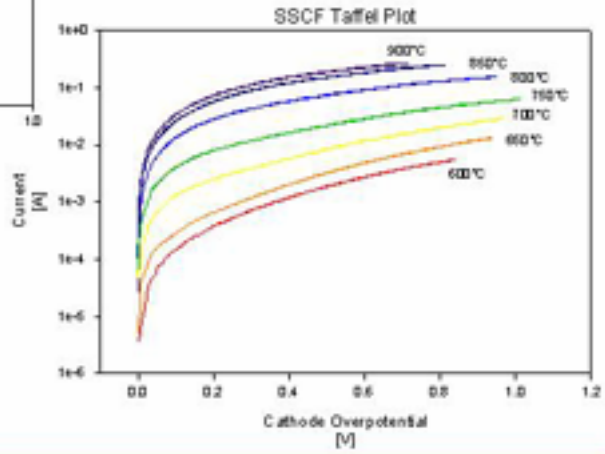

X-Ray Diffraction Analysis

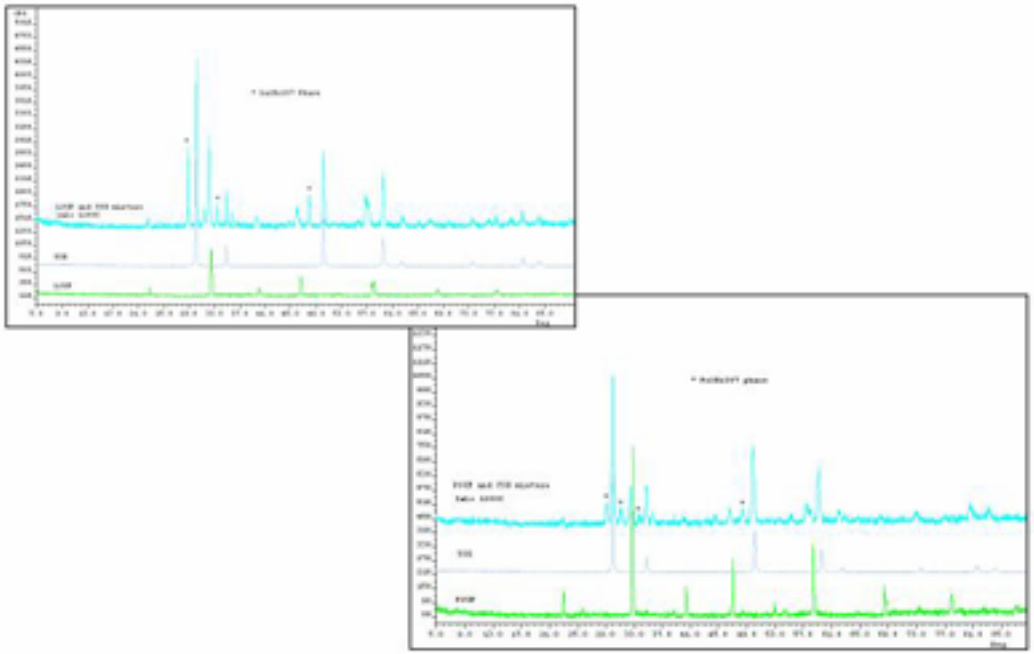

X-Ray Diffraction Analysis